POLITECNICO DI MILANO

Scuola di Ingegneria Industriale e dell'Informazione

Corso di Laurea Magistrale in Ingegneria Nucleare

Numerical characterization of a monolithic ΔE-E telescope detector for Heavy Ion Therapy Quality Assurance

Relatore: Prof. Andrea Pola

Correlatore: D.ssa Susanna Guatelli

Giordano Biasi 799377

A.A. 2014-2015

List of Contents

I. List of Figures V

II. List of Tables XIII

III. Abstract XV

IV. Abstract (italiano) XVII

1. Introduction 1
1.1. Scope of the project 1

2. Literature Review 3
2.1. Heavy Ion Therapy: an overview 3
2.2. Basic principles of microdosimetry 10
2.2.1. Introductory remarks 10
2.2.2. Microdosimetry 15
2.2.3. TEPC 17
2.3. ΔE-E telescope detectors 21
2.4. The MKM Model 26

3. Methodology 29
3.1. The simulation study 29
3.2. Overview of the Geant4 Toolkit 32

4. Validation of GEANT4 for Heavy Ion Therapy 35
4.1. The Geant4 application 37
4.2. Simulation results 41

5. ΔE-E telescope characterization with a clinical carbon ion beam at CNAO 49
5.1. Experiment set-up 49
5.2. The GEANT4 application 50
5.3. Characterization of carbon ions radiation field 52
5.4. Characterization of the ΔE-E telescope response 64
5.4.1. In-field configuration 67
5.4.2. Out of field configuration 80

6. ΔE-E telescope characterization with a low energy carbon ion beam at ANU 87
6.1. Experimental set-up 87

6.2. The GEANT4 application 89
6.3. Characterization of the carbon ion radiation field 90
6.4. Characterization of the ΔE-E telescope response 95

7. Conclusions 105

8. Bibliography 107

I. List of Figures

Figure 2.1 Considerations for the implementation of new carbon ion facilities. Image courtesy of [7] 6

Figure 2.2 Depth dependence of the deposited dose for different radiations. An inverted dose-depth distribution is clinically much more favorable than an exponentially decaying distribution. Image courtesy of [8]. 6

Figure 2.3 Comparison of treatment plans with 2 fields of carbon ion (IMPT—left panel) and with 9 fields of x-rays (IMRT—right panel). In both cases the conformity to the target volume is good but for carbon ions the dose to the normal tissues is much smaller. Image courtesy of [10]. 7

Figure 2.4 RBE_{10} profile (a) and biological dose (b) distribution obtained by measurement and Monte Carlo calculation with GEANT4 for HIT with carbon ions. From the RBE profile it is apparent that the biological effectiveness of carbon ions varies in the SOBP and that RBE values are greater than unity. Image courtesy of [11]. 7

Figure 2.5 Bragg curve for 330 MeV/nucleon ^{12}C in water measured at GSI with large parallel-plate ionization chambers. The data points are compared to a model calculation (solid line). The calculated contributions from the primary particles (red line) and from nuclear fragments (blue line) are also shown. Image courtesy of [14]. 9

Figure 2.6 Basic steps of nuclear fragmentation. Image courtesy of [17]. 10

Figure 2.7 Illustration of DNA helix being damaged by incident radiation. Low LET particles such as x-rays are expected to produce single strand breaks while high LET particles such as carbon ions are expected to produce more biologically significant double strand breaks. Image courtesy of [20]. 12

Figure 2.8. Structure of a proton and of a carbon track in nanometre resolution are compared with a schematic representation of a DNA molecule. In the picture it can be appreciated that the higher density of the secondary electrons produced by high LET primary carbon ions creates a larger amount of clustered DNA damage. Image courtesy of [8]. 12

Figure 2.9. Dependency of RBE on LET. Image courtesy of [21]. 13

Figure 2.10 SOBP obtained by superimposing several mono-energetic pristine Bragg curves each of which is associated to particles of a different kinetic energy. In the SOBP it is possible to distinguish a plateau, a proximal peak, a distal peak, a distal edge and a tail. 14

Figure 2.11 Physical and biological doses in a SOBP in water. An inhomogeneous physical dose is required to deliver a constant

biological dose in the target tumor because the RBE varies with position in the SOBP. 15

Figure 2.12 Picture and schematic of a Tissue Equivalent Proportional Counter. 18

Figure 2.13. Microdosimetric spectrum *yd(y)* vs *log(y)* obtained by irradiating a spherical TEPC simulating sites of 1, 2, 3 um of diameter with 14.18 MeV mono-energetic neutrons. Three zones are highlighted: (A) low LET, (B) intermediate LET, (C) high LET. Image courtesy of [18]. 20

Figure 2.14. A schematic of a solid state monolithic ΔE-E telescope detector. The E stage and the ΔE stage are separated by a P+ electrode. Thin N+ layers are used as contacts for both the ΔE stage and the E stage. The detector is operated biased. Image courtesy of [38]. 22

Figure 2.15. Example of the ΔE-E telescope response when irradiated with 400 MeV/nucleon 22Ne and plotted in a ΔE-E 2D plot, the NE102A being the ΔE layer and the BGO being the E layer of the telescope. Image courtesy of [15]. 23

Figure 2.16. ΔE-E plot acquired with a pixelated silicon telescope when irradiated with 2.7 MeV mono-energetic neutrons. Three different regions can be distinguished based on LET: (a) high-LET recoil protons, (b) low-LET secondary electrons, (c) intermediate region. Image courtesy of [34]. 24

Figure 2.17. Schematic of a pixelated silicon telescope detector with the E stage and the pixels constituting the ΔE layer. A single pixel is pictured on the right detailing the surrounding guard. Image courtesy of [34]. 25

Figure 3.1 In-field configuration: the detector is placed inside the field due to primary particles, at different depths along the beam path (red boxes). In the figure red and grey boxes represent detector positions whereas the blue solid represents the 3D SOBP and plateau in the water medium target due to primary carbon ions coming from the figure's upper-left angle. It should be noted that the detector is to be placed at each position one at a time and not at all of them simultaneously, in order to prevent perturbation of the radiation field. In this figure, grey boxes are detector positions out of field, as explained in Figure 3.2. 30

Figure 3.2 Out-of-field configuration: the detector is placed outside the field due to primary particles, at different distances from the axis (red boxes). In the figure red and grey boxes represent detector positions whereas the blue solid represents the 3D SOBP and plateau in the water medium target due to primary carbon ions coming from the figure's upper-left angle. It should be noted that the detector was placed at each position one at a time and not at all of them simultaneously, in order to prevent a distortion in the radiation field analysis. 31

Figure 3.3 Out-of-field configuration: the detector is placed outside the field due to primary particles, at different depths along the axis but at a fixed

distance from the axis (red boxes). In the figure red and grey boxes represent detector positions whereas the blue solid represents the 3D SOBP and plateau in the water medium target due to primary carbon ions coming from the figure's upper-left angle. It should be noted that the detector was placed at each position one at a time and not at all of them simultaneously, in order to prevent a distortion in the radiation field analysis. 31

Figure 4.1. Experimental setup used for measuring the absorption of primary ^{12}C ions in water. Image courtesy of [61]. 36

Figure 4.2. Experimental set-up of the GEANT4 simulation. The water box, is placed in the center of the world, is traversed by simulated particles' tracks. 37

Figure 4.3: Bragg peak calculated activating different electromagnetic physics lists and no hadronic model for 200 MeV/nucleon carbon ions beam. 41

Figure 4.4: Bragg peak calculated activating different hadronic physics lists with *electromagnetic physics list option 3* for 200 MeV/nucleon carbon ions beam. 42

Figure 4.5: Bragg peak calculated activating different electromagnetic physics lists and no hadronic model for 400 MeV/nucleon carbon ions beam. 42

Figure 4.6. Bragg peak calculated activating different hadronic physics lists with *electromagnetic physics list option 3* for 400 MeV/nucleon carbon ions beam. 43

Figure 4.7. Percentage difference on energy deposition between *INCL++* and *QMD* physics lists, with *QMD* as a reference. The *electromagnetic standard package option 3* was selected for both the simulations as the electromagnetic model. 44

Figure 4.8. Percentage difference on energy deposition between *QGSP_BIC_HP* and *QMD* physics lists, with *QMD* as a reference. The *electromagnetic standard package option 3* was selected for both the simulations as the electromagnetic model. 44

Figure 4.9. Bragg Peak position for 200 MeV/nucleon carbon ions beam in water. Experimental result is plotted in black, simulated one in blue. 46

Figure 4.10. Bragg Peak position for 400 MeV/nucleon carbon ions beam in water. Experimental result is plotted in red, simulated one in blue. 46

Figure 5.1: CNAO experimental set-up. 49

Figure 5.2: Experimental set-up of the Geant4 simulation. The ripple filter is visible on the left (light blue) and the PMMA box with the water target on the right (blue and white frames delimit the boxes). 50

Figure 5.3. Simulated energy spectrum: number of primary particles generated per slice normalized to the total number of generated primaries. 52

Figure 5.4. SOBP produced by a clinical ^{12}C ion beam and its secondary fragments in a phantom, modelling the patient. The blue line shows the energy deposited by primary ^{12}C whereas the red line shows the total contribution of the secondary particles. Note that the origin is placed at the front of the 10 mm thick PMMA phantom surrounding the water target, which explains the higher energy deposition. The energy deposition in MeV is normalized to the total number of primary particles. The bin of the x axis is 0.1 mm. 54

Figure 5.5. 2D distribution of the point of origin of secondary ^{1}H normalized to the number of incident primary carbon ions. 55

Figure 5.6. 2D distribution of the point of origin of secondary ^{4}He normalized to the number of incident primary carbon ions. 55

Figure 5.7. 2D distribution of the point of origin of secondary ^{6}Li normalized to the number of incident primary carbon ions. 56

Figure 5.8. 2D distribution of the point of origin of secondary ^{9}Be normalized to the number of incident primary carbon ions. 56

Figure 5.9. 2D distribution of the point of origin of secondary ^{11}B normalized to the number of incident primary carbon ions. 57

Figure 5.10. 2D distribution of the point of origin of secondary ^{12}C normalized to the number of incident primary carbon ions. 57

Figure 5.11. 2D distribution of the point of origin of secondary ^{16}O normalized to the number of incident primary carbon ions. 58

Figure 5.12. 2D distribution of the point of origin of secondary neutrons normalized to the number of incident primary carbon ions. 58

Figure 5.13. 2D energy deposition in the target due to H. 60

Figure 5.14. 2D energy deposition in the target due to He. 60

Figure 5.15. 2D energy deposition in the target due to Li. 61

Figure 5.16. 2D energy deposition in the target due to Be. 61

Figure 5.17. 2D energy deposition in the target due to B. 62

Figure 5.18. 2D energy deposition in the target due to C (primaries). 62

Figure 5.19. 2D energy deposition in the target due to C (secondaries). 63

Figure 5.20. 2D energy deposition in the target due to O. 63

Figure 5.21. Total 2D energy deposition in the target due to primary particles and secondary particles. 64

Figure 5.22. ΔE-E plot for telescope placed in-field at 50 mm in the phantom. There is a clustered energy deposition in the detector between 10 and 15 MeV due to primary carbon ions. The amount of H and He nuclei is negligible. 69

Figure 5.23. ΔE-E plot for telescope placed in-field at 150 mm in the phantom. 70

Figure 5.24. ΔE-E plot for telescope placed in-field at 170 mm in the phantom. 70

Figure 5.25. ΔE-E plot for telescope placed in-field at 190 mm in the phantom. The maximum energy deposition in the detector as a whole due to primary carbon ions is somewhere around 180 MeV, corresponding to the kink in the plot. 71

Figure 5.26. ΔE-E plot for telescope placed in-field at 195 mm in the phantom. 71

Figure 5.27. ΔE-E plot for telescope placed in-field at 210 mm in the phantom. The maximum energy deposition in the detector as a whole due to primary carbon ions is somewhere around 180 MeV, corresponding to the kink in the plot. Loci of secondary fragments are visible. 72

Figure 5.28. ΔE-E plot for telescope placed in-field at 220 mm in the phantom. 72

Figure 5.29. ΔE-E plot for telescope placed in-field at 225 mm in the phantom. Primary carbon ions still deposit energy in the detector but in far smaller quantity. Heavier fragments such as Ne, F and O are present. 73

Figure 5.30. ΔE-E plot for telescope placed in-field at 230 mm in the phantom. Primary carbon ions deposit a limited amount of energy in the detector. Main contributors to the energy deposition are secondary fragments such as Ne, F and lighter fragments. 73

Figure 5.31. ΔE-E plot for telescope placed in-field at 250 mm in the phantom. 74

Figure 5.32. Microdosimetric spectrum obtained for the telescope placed in-field at 50 mm in the phantom. Spectra is dominated by primary carbon ions contribution. 75

Figure 5.33. Microdosimetric spectrum obtained for the telescope placed in-field at 150 mm in the phantom. The spectrum is dominated by primary carbon ions contribution at higher lineal energy with respect to previous position. 76

Figure 5.34. Microdosimetric spectrum obtained for the telescope placed in-field at 190 mm in the phantom. The spectrum is dominated by primary carbon ions contribution at higher lineal energy with respect to previous position. 76

Figure 5.35. Microdosimetric spectrum obtained for the telescope placed in-field at 195 mm in the phantom. 77

Figure 5.36. Microdosimetric spectrum obtained for the telescope placed in-field at 210 mm in the phantom. 77

Figure 5.37. Microdosimetric spectrum obtained for the telescope placed in-field at 220 mm in the phantom. Spectra is dominated by primary carbon ions contribution. Carbon edge becomes visible. 78

Figure 5.38. Microdosimetric spectrum obtained for the telescope placed in-field at 225 mm in the phantom. Spectra is dominated by secondary fragments. 78

Figure 5.39. Microdosimetric spectrum obtained for the telescope placed in-field at 230 mm in the phantom. Spectra is dominated by secondary fragments. 79

Figure 5.40. Microdosimetric spectrum obtained for the telescope placed in-field at 250 mm in the phantom. Spectra is dominated by secondary fragments. 79

Figure 5.41. RBE_{10} profile obtained from microdosimetric spectra using the MKM model. Depth values refer to the depth in the phantom, an in-field configuration. As expected, the profile is almost flat in the plateau and in the tail of the SOBP, with the higher values recorded in the distal part of the SOBP. Lines are shown to help the eye and only the points where error bars are shown where simulated. 80

Figure 5.42. ΔE-E plot for telescope placed out of field at 200 mm depth in the phantom and 35 mm from the axis. Only a small amount of low energy secondary fragments are visible. 81

Figure 5.43. Microdosimetric spectrum obtained for the telescope placed out-of-field at 200 mm in the phantom and at 35 mm distance from the axis. The spectrum is dominated by secondary fragments. 82

Figure 5.44. RBE_{10} profile obtained from microdosimetric spectra using the MKM model. Depth values refer to the depth in the phantom at a distance of 35 mm from the main axis, an out of field configuration. As expected, the profile is almost flat with values significantly lower than the corresponding values for the same depths in field. Lines are shown to help the eye and only the points where error bars are shown where simulated. 82

Figure 5.45. ΔE-E plot for telescope placed out of field at 210 mm depth in the phantom and 25 mm from the axis. Only a small amount of low energy secondary fragments are visible. 84

Figure 5.46. Microdosimetric spectrum obtained for the telescope placed out-of-field at 210 mm in the phantom and at 15 mm distance from the axis. The spectrum is dominated by primary carbon ions. 84

Figure 5.47. Microdosimetric spectrum obtained for the telescope placed out-of-field at 210 mm in the phantom and at 20 mm distance from the axis. The spectrum is dominated by secondary fragments. 85

Figure 5.48. Microdosimetric spectrum obtained for the telescope placed out-of-field at 210 mm in the phantom and at 35 mm distance from the axis. The spectrum is dominated by secondary fragments. 85

Figure 5.49. RBE_{10} profile obtained from microdosimetric spectra using the MKM model. Depth values refer to the distance from the main axis. Positions from 0 to 15 mm are in-field whereas positions from 15 to 35 mm are out of field. The RBE_{10} is flat in-field and fall sharply

towards significantly lower values out of field, where the biological efficacy of the carbon ion beam is thus smaller. Lines are shown to help the eye and only the points where error bars are shown where simulated. 86

Figure 6.1: the 14UD pelletron accelerator at the Heavy Ion facility at the Australian National University (ANU). 87

Figure 6.2: a virtual model of the vacuum chamber with the gold scatterer holder on the left [A] and the polyethylene foils holder [B] and detector holder [C] at the centre. The primary beam enters the chamber from the left, passes through the scatterer [A] and hits the foil with the select thickness before hitting the detector. 88

Figure 6.3. Simulated set-up with incoming primary beam (yellow arrow). The polyethylene phantom in figure (grey box) was placed in a simulated vacuum world (light blue box). To simulate the detector response at different depths along the primary carbon ions Bragg curve, the ΔE-E telescope (white box) was placed at different positions starting from the phantom surface. Positions were simulated one at a time in order to not alter the radiation field. 89

Figure 6.4. Bragg Peak of a 5.95 MeV/nucleon carbon ion beam incident on a polyethylene phantom. The black dots represent the different depths at which the detector was placed for the subsequent study detailed in section 6.4 91

Figure 6.5. 2D distribution of the point of origin of secondary ^{1}H normalized to the number of incident primary carbon ions. 91

Figure 6.6. 2D distribution of the point of origin of secondary ^{4}He normalized to the number of incident primary carbon ions. 92

Figure 6.7. 2D distribution of the point of origin of secondary ^{12}C normalized to the number of incident primary carbon ions. 92

Figure 6.8. 2D distribution of the point of origin of secondary neutrons normalized to the number of incident primary carbon ions. 93

Figure 6.9. 2D energy deposition in the target due to He. 93

Figure 6.10. 2D energy deposition in the target due to secondary carbon ions. 94

Figure 6.11. 2D energy deposition in the target due to primary carbon ions. 94

Figure 6.12. 2D total energy deposition in the target. 95

Figure 6.13. ΔE-E plot for telescope placed in-field at 0 μm depth from the phantom surface closest to the incoming primary beam. 97

Figure 6.14. ΔE-E plot for telescope placed in-field at 157 μm depth from the phantom surface closest to the incoming primary beam. 98

Figure 6.15. ΔE-E plot for telescope placed in-field at 171 μm depth from the phantom surface closest to the incoming primary beam. 98

Figure 6.16. ΔE-E plot for telescope placed in-field at 183 μm depth from the phantom surface closest to the incoming primary beam. 99

Figure 6.17. Microdosimetric spectrum obtained for the telescope placed in-field at 0 μm depth from phantom surface closest to the incoming primary beam. 100

Figure 6.18. Microdosimetric spectrum obtained for the telescope placed in-field at 157 μm depth from phantom surface closest to the incoming primary beam. 101

Figure 6.19. Microdosimetric spectrum obtained for the telescope placed in-field at 171 μm depth from phantom surface closest to the incoming primary beam. 101

Figure 6.20. Microdosimetric spectrum obtained for the telescope placed in-field at 183 μm depth from phantom surface closest to the incoming primary beam. 102

Figure 6.21. Microdosimetric spectrum obtained for the telescope placed in-field at 200 μm depth from phantom surface closest to the incoming primary beam. 102

Figure 6.22. RBE_{10} profile obtained from microdosimetric spectra using the MKM model. Depth values refer to depths from phantom surface closest to the incoming primary beam, an in-field configuration. Counter-intuitively, the profile does not show a rising trend towards the Bragg Peak followed by a sharp fall-off. On the contrary, the RBE_{10} values decrease towards the Bragg Peak due to the overkilling effect. The sharp increase at the Bragg Peak is instead due to an intrinsic limitation of the microdosimetric model: carbon ions at these depths are coming to a complete stop in the ΔE layer of the detector whereas they should be crossing it for the microdosimetry theory to be coherently applied. Lines are shown to help the eye and only the points where error bars are shown where simulated. 103

II. List of Tables

Table 2.1 Elemental components (percent by weight) of a methane based and a propane based tissue equivalent gases. Table courtesy of [22]. 18

Table 4.1. Standard PMMA composition used in the simulations. Mass percentage of each component is given. 36

Table 4.2: Proportion of primary carbon ions, with initial energy 100, 200, 300 and 400 MeV/nucleon reaching the Bragg Peak without occurring in a nuclear interaction in a thick water target. GEANT4 simulated results. Table courtesy of [62]. 37

Table 4.3: Physics Lists EM constructors in GEANT4 10.0 [64]. 39

Table 5.1. Primary carbons are generated with different initial kinetic energies; each kinetic energy has a defined weight and corresponds to a different range (corresponding to a “slice” of the tumor to irradiate). The weight for each slice is provided in the Table. The data are experimental. 51

Table 5.2: Secondary particle yields produced by one incident ^{12}C. In the table the value of ^{12}C includes only secondary ^{12}C ions generated by heavier nuclei fragmentation processes or elastic scattering in the PMMA phantom. ^{16}O comes mainly by elastic scattering in PMMA or, mainly, water. 53

Table 5.3: Minimum kinetic energy of different fragments to produce coincidence events in the ΔE-E telescope. 65

Table 5.4: Kinetic energy of different types of particle to completely stop in the detector. Values have been extrapolated from the proton range in silicon accessed from NIST database, in the non-relativistic hypothesis [32]. 66

Table 5.5: Positions where the ΔE-E telescope was placed along the SOBP, in the in-field configuration. The column on the right indicates the number of events generated in each simulation to obtain statistically meaningful results. 67

Table 6.1. The detector was placed at various depths in the polyethylene phantom, starting from the phantom surface closest to the incoming primary beam. Positions are distributed along the Bragg curve in order to cover plateau, Bragg Peak proper and tail regions. 96

III. Abstract

^{12}C ions in Heavy Ion Therapy (HIT) are currently used in a growing number of clinical facilities all around the world due to their favorable Radiobiological Effectiveness (RBE) and better conformality to the tumor target when compared to alternative radiotherapy treatments. The RBE, defined as the ratio of the dose delivered by photons to the dose delivered by the radiation under study producing the same biological effect, is used to determine the physical dose and it is an essential input parameter to the clinical HIT Treatment Planning System.

HIT is characterized by a complex radiation field with a significant amount of fragments originating from the primary carbon ions. These affect significantly both the RBE and the dose delivery in the patient and are a major concern especially at the distal edge of the Bragg Peak, where organs at risk may be located.

The development of Quality Assurance (QA) detectors able to effectively characterize the HIT radiation field with sub-millimeter spatial resolution and measure microdosimetric spectra allowing the determination of the RBE profile along the Bragg Peak is of pivotal importance. Even though such a detector does not currently exist in routine QA procedures, the silicon ΔE-E telescope detector developed at the Politecnico di Milano is being considered as a very promising candidate.

In this thesis, the detector response is thus characterized both in a clinical and in a low-energy HIT radiation field by means of Monte Carlo simulations with the GEANT4 toolkit, the accuracy of which has been quantified by comparing Bragg curves of ^{12}C ions with clinical energies against published experimental data.

This work shows that the ΔE-E telescope detector can be effectively used both to characterize the HIT radiation field and to acquire microdosimetric spectra allowing the determination of the RBE profile along the Bragg

Peak. The simulation results complement and support the experimental characterization of the same device.

IV. Abstract (italiano)

Il cancro, secondo l'Organizzazione Mondiale della Sanità (OMS), è una delle principali cause di morte al mondo e circa la metà dei pazienti diagnosticati ricevono trattamenti radioterapici, spesso in combinazione con altre terapie come chirurgia e chemioterapia.

Un numero crescente di centri medici sono oggi attrezzati per offrire trattamenti radioterapici con ioni carbonio. La terapia, nota in inglese come *Heavy Ion Therapy* (HIT), è affermata e riconosciuta a livello globale ed è stato dimostrato essere adatta al trattamento di tumori profondi e radio-resistenti. I principali vantaggi che offre quando confrontata con trattamenti radioterapici alternativi sono:

- il deposito di energia nel mezzo segue il caratteristico andamento a curva di Bragg con il massimo dell'energia ceduta in corrispondenza del Picco di Bragg al termine del range delle particelle; inoltre, essendo gli ioni ^{12}C particelle cariche possono essere più facilmente collimati in un fascio di sezione ridotta contraddistinto dall'aver sia un minor *scattering* laterale sia un minor *straggling* longitudinale. Queste caratteristiche si traducono da un lato in una miglior copertura del volume trattato e dall'altro in una più facile salvaguardia dei tessuti sani circostanti il target;
- una maggiore efficacia radiobiologica, caratteristica della radiazione che viene descritta attraverso il parametro RBE (*Radiobiological Effectiveness*). Questo, definito come il rapporto tra la dose depositata da fotoni e la dose depositata dalla radiazione in studio tale che produca lo stesso effetto biologico, è usato per determinare la dose fisica ed è un dato essenziale per la pratica clinica in HIT che può essere ricavato facendo uso della teoria microdosimetrica. In particolare nel caso degli ioni ^{12}C il parametro RBE è caratterizzato dall'avere valori bassi nelle parti iniziali del range delle particelle nel mezzo e via via crescenti fino ad un massimo raggiunto attorno agli

ultimi 2 cm del range. Gli ioni ^{12}C sono perciò detti essere radiobiologicamente più efficaci in corrispondenza del Picco di Bragg, ove è localizzato il target, rispetto al plateau della curva di Bragg. Inoltre il valore del parametro RBE in corrispondenza del Picco di Bragg risulta essere maggiore di 1, ulteriore fatto che rende la HIT con ioni ^{12}C vantaggiosa rispetto alle alternative radioterapiche.

Nel capitolo 2, dopo aver analizzato i fondamenti fisici e lo stato attuale della pratica HIT ed averne discusso i vantaggi e gli svantaggi rispetto alle alternative radioterapiche, viene introdotta la teoria su cui si basa la microdosimetria e le sue applicazioni. Il *Microdosimetric Kinetic Model* (MKM), applicato per determinare i valori del parametro RBE partendo dagli spettri microdosimetrici acquisiti con il rivelatore, è descritto al termine del capitolo.

È importante notare come in HIT il paziente è sottoposto ad un campo di radiazione complesso costituito per una frazione significativa da frammenti originati dal fascio primario di ioni carbonio. In effetti la loro presenza influenza significativamente sia i valori complessivi che il parametro RBE assume sia la dose depositata nei tessuti e costituiscono perciò un fattore di preoccupazione in particolare per quanto riguarda la parte distale del Picco di Bragg, zona che nella pratica clinica corrisponde alla localizzazione di possibili organi a rischio.

Lo sviluppo di rivelatori per *Quality Assurance* (QA) in grado di caratterizzare efficacemente il campo di radiazione per un trattamento HIT è evidentemente di fondamentale importanza. Caratteristiche essenziali per questi strumenti sono una risoluzione spaziale sub-millimetrica e la capacità di acquisire spettri microdosimetrici permettendo quindi la determinazione dei valori del parametro RBE lungo la curva di Bragg. Sebbene tali rivelatori per QA attualmente non esistano nella pratica clinica, il rivelatore telescopico ΔE-E al silicio sviluppato al Politecnico di Milano può essere considerato un candidato promettente.

Il rivelatore telescopico ΔE-E, proposto dal gruppo di ricerca guidato dal prof. S. Agosteo e dal prof. A. Fazzi, è un rivelatore allo stato solido composto da due layer di silicio. Il primo, detto stage ΔE, è caratterizzato dall'avere uno spessore molto inferiore rispetto al range in silicio delle particelle primarie incidenti, così da renderlo utilizzabile come microdosimetro. Al contrario, il secondo layer è detto stage E ed ha uno spessore maggiore del range in silicio delle particelle primarie incidenti. L'identificazione delle particelle componenti il campo di radiazione si ottiene associando l'informazione sul deposito di energia nei due layer, che sono operati in coincidenza.

Nel capitolo 2 è descritto il rivelatore telescopico ΔE-E al silicio con particolare attenzione ai vantaggi offerti da questo rispetto ad una TEPC, strumento che costituisce l'attuale standard per la microdosimetria.

Nell'ambito di questo lavoro di tesi, la caratterizzazione numerica della risposta del rivelatore telescopico ΔE-E al silicio è stata condotta attraverso un'applicazione originariamente sviluppata a partire dal Toolkit GEANT4 da S. Guatelli e D. Bolst al CMRP, University of Wollongong, e adattata per i casi studio presi in esame. Il Toolkit GEANT4 è basato su codice Monte Carlo, strumento che fornisce tecniche di simulazione oggi utilizzate in molte aree della ricerca scientifica e della sviluppo industriale. Esse costituiscono probabilmente il metodo più accurato oggi a disposizione per descrivere il trasporto di particelle in un mezzo e rappresentano perciò un valido strumento per ottenere una descrizione della distribuzione del deposito di energia nel mezzo oltre ad una caratterizzazione del campo di radiazione e dei relativi parametri.

Il Toolkit GEANT4 e l'applicazione sviluppata per le simulazioni realizzate nell'ambito di questo lavoro di tesi sono descritti nel capitolo 3.

Tuttavia il comportamento simulato delle particelle è consistente con la realtà solo se i modelli scelti per descrivere la fisica coinvolta nel problema in studio sono sufficientemente efficaci. La scelta di questi è senz'altro un

aspetto di estrema importanza. Nel capitolo 4 sono confrontati i vari modelli fisici resi disponibili con il Toolkit GEANT4 in particolare nel caso della riproduzione di Picchi di Bragg sperimentali per fasci di ioni ^{12}C descritti in letteratura. Questa valutazione è importante per poter quantificare l'accuratezza dei risultati simulati nel corso della caratterizzazione numerica del rivelatore telescopico ΔE-E al silicio e presentati nei capitoli successivi.

La caratterizzazione numerica della risposta del rivelatore è stata valutata in due scenari di interesse:

- nel campo di radiazione dovuto ad un fascio clinico di ioni ^{12}C presso il Centro Nazionale di Adroterapia Oncologica (CNAO). Lo studio, i cui risultati sono presentati nel capitolo 5, è particolarmente importante per le energie cliniche utilizzate;
- nel campo di radiazione dovuto ad un fascio di ioni ^{12}C a bassa energia presso lo Heavy Ion accelerator (14UD), Australian National University (ANU). Lo studio, i cui risultati sono discussi nel capitolo 6, è importante per approfondire la comprensione dei valori che assume il parametro RBE nella parte distale del Picco di Bragg. Esso può essere considerato come uno step verso una più accurata descrizione degli effetti indesiderati di un trattamento HIT.

Per entrambi gli scenari, è stato innanzitutto condotto uno studio di tipo preliminare atto a caratterizzare il campo stesso e fornire indicazioni in termini di deposizione di energia delle particelle e identificazione dei frammenti secondari. Successivamente la caratterizzazione numerica della risposta del rivelatore quando posizionato nel target all'interno del campo di radiazione viene presentata attraverso dei plot della deposizione energetica nello stadio ΔE versus la deposizione energetica negli stadi ΔE+E (ΔE-E plots). La risposta del rivelatore è stata valutata sia nella configurazione detta *In-field*, ovvero con il rivelatore all'interno del fascio primario, sia nella configurazione detta *Out-of-field*, ovvero con il rivelatore posto a distanza rispetto l'asse al centro del fascio primario. Uno studio in configurazione *Out-of-field* è rilevante per la valutazione della dose al tessuto sano attorno

al tumore, il target del trattamento radioterapico nella pratica clinica. Lo stadio ΔE del rivelatore è stato anche caratterizzato per misure microdosimetriche. Dagli spettri microdosimetrici acquisiti, applicando il modello MKM, sono stati ottenuti i valori per RBE_{10} per varie profondità e posizioni nel target.

Si è mostrato come il rivelatore telescopico ΔE-E al silicio possa essere efficacemente utilizzato sia per caratterizzare un campo di radiazione complesso come quello dovuto ad ioni ^{12}C con energie cliniche dell'HIT, permettendo teoricamente l'identificazione dei frammenti, sia per acquisire spettri microdosimetrici con una risoluzione spaziale sub-millimetrica che possono essere utilizzati per la determinazione dei valori del parametro RBE lungo la curva di Bragg e nella parte distale del Picco di Bragg. I risultati della caratterizzazione numerica potranno in futuro complementare e supportare una caratterizzazione sperimentale dello stesso strumento. Queste conclusioni sono raccolte nel capitolo 7.

1. Introduction

1.1. Scope of the project

Heavy Ion Therapy (HIT), consisting of carbon ion beams incident on the patient, has been shown to be very suitable for the treatment of deeply seated and radio-resistant tumors, thanks both to the energy deposition profile and the favorable Radiobiological Effectiveness (RBE) of carbon ions, when compared to alternative types of radiation [1]. HIT is nowadays an important and prominent field for scientific and technological research.

In Chapter 2, after a brief overview of the current status of HIT, microdosimetry is introduced along with its applications. After that, a description of the ΔE-E telescope detector developed at the Politecnico di Milano is given with a focus on its advantages over Tissue Equivalent Counters (TEPCs), the current standard for microdosimetry measurements. The Microdosimetric Kinetic Model (MKM), applied to the microdosimetric response of the ΔE-E telescope to determine the RBE of HIT, is described as well.

The GEANT4 Monte Carlo toolkit used in this thesis work to characterize the ΔE-E telescope detector response is presented in Chapter 3 while its validation for HIT applications is discussed in Chapter 4.

The ΔE-E telescope detector response has been charaterized in the following scenarios:

- placed in a clinical ^{12}C ions radiation field at the Centro Nazionale di Adroterapia Oncologica (CNAO) HIT facility, a study whose importance stems from the clinical energies and experimental set-up used and whose results are presented in Chapter 5;

- placed in a low-energy ^{12}C ions radiation field at the Heavy Ion accelerator (14UD) facility at the Australian National University (ANU), a study devised to better understand the RBE profile in the distal edge of the Bragg Peak i.e. at the borders of the malignant tissues in the clinical practice. This is an important step towards the aim of obtaining a comprehensive understanding of the side effects of radiotherapy. This part is covered in Chapter 6.

Finally, chapter 7 summarizes the conclusions of this thesis work.

2. Literature Review

2.1. Heavy Ion Therapy[1]: an overview

Radiotherapy techniques are currently used either as the sole treatment or in combinations with other therapies to treat various types of cancer, which according to the World Health Organisation (WHO) is one of the leading causes of death in the world [2] and the single biggest cause in Australia [3]. Nowadays approximately half of the patients diagnosed with cancer receive radiotherapy as part of their treatment along with surgery and chemiotherapy and it is often the preferred approach whenever other options may not be viable, as in inaccessible or intimately entwined with vital organs tumours, or when regional spreads of the malignant tissues may occur.

Charged particles beams have been used to treat various types of tumours since their use was first proposed by Robert R. Wilson in 1946. Pioneering work in Heavy Ion Therapy (HIT) was performed at the Lawrence Berkley Laboratory, where patient treatments with helium ions started in 1957, but it was not until the 1994 that the first routine carbon ions beam for a full-scale clinical study was initiated at the Heavy Ion Medical Accelerator in Chiba (HIMAC) at the National Institute of Radiological Sciences (NIRS) in Japan, which has treated 4000 patients since December 2008 [4]. Carbon ion therapy has now been available at various facilities in Japan, among others at the Hyogo Ion Beam Medical Center, at the Gunma Medical Center, at the SAGA Heavy Ion Medical Accelerator in Tosu and at the Kanagawa Cancer Center in Yokohama for several years.

1 The term heavy ions is being commonly used in the particle therapy community to characterize ions heavier than protons, although relatively light considering the full range of nuclei, but usage may vary between countries. For instance, in Japan heavy ion therapy refers just to carbon ion beams unless otherwise specified whereas in the EU the practice of charged particle therapy is generally collectively referred to as hadron therapy [6].

In the meanwhile the European Light Ion Medical Accelerator (EULIMA) project has laid the foundations for HIT in Europe with the Gesellschaft für Schwerionenforschung GmbH (GSI) in Germany which started patient treatments with carbon ion beams in 1997. The facility has subsequently ceased patient treatment in favour of the newly built Heidelberg Ion Therapy Center in 2009. In Italy the National Centre for Oncological Hadrontherapy (CNAO) in Pavia has been treating patients with carbon ion beams since 2010 and other in-development facilities in Europe include the MedAUSTRON in Austria where the first treatment is expected to happen in 2015 and the ETOILE in Lyon, France. Twenty more facilities are currently planned over the next decade [5].

Notwithstanding the technical complexity and enormous capital investment required to build a clinical HIT facility, mainly due to the fact that currently the only viable source for high energy ion beams are synchrotrons, this trend of building new HIT facilities prove that carbon ion therapy is established as a worldwide recognized cancer therapy [6].

During the last decades various forms of radiation have been used in radiotherapy techniques, including electron, neutrons, pi-mesons, protons and heavy charges ions as ^{12}C and ^{20}Ne beams as well as implanted radioactive sources (a technique known as brachytherapy) and the fruitful collaborations of scientists, engineers and physicians have let to outstanding achievements in this practice. HIT is a valid option for most malignancies because of the higher RBE and tumor comformality, but the significant cost associated with the construction and operation of dedicated facilities as well as the lack of long term data regarding toxicity and secondary malignaincy [7] suggest a selective use of the technology as the best option.

On the other hand, the advantages of the use of carbon ions in radiotherapy are important and can be summurized as the four physical and biological properties as listed below [8]:

1- The maximum energy deposit occurs at the Bragg Peak at the end of the range with a sharp longitudinal dose fall-off. Being charged particles carbon ions can easily be focused in a narrow scanning pencil beam of variable penetration depth with minor lateral scattering and longitudinal straggling when compared to other particles. This means that is HIT is more conformal to the tumor target with respect to other radiotherapy modalities as shown in Figure 2.2 and Figure 2.3. This means that healthy tissues surrounding the tumor target can be more easily spared. This property is more emphasized when techniques of active dose shaping by magnetic deflection are used.
2- The RBE depth profile is highly favourable in that high energy carbon ions have low RBE in the entrance channel and high RBE in the last 2 to 3 cm of their range. The RBE of therapeutic carbon ions at the Bragg Peak becomes larger than 1 when the LET becomes greater than 20 keV/μm, i.e. in the last 40 mm of a carbon track in water or biological tissue [8], whereas the RBE of therapeutic protons is in average approximately 1 at the Bragg Peak [9]. Heavy ions are biologically more effective in the peak than in the plateau and their RBE increases as they advance deeper in the human tissues, for which see Figure 2.4.
3- The location where the dose is deposited can be determined by means of on-line positron emission tomography (PET) with millimetre precision.

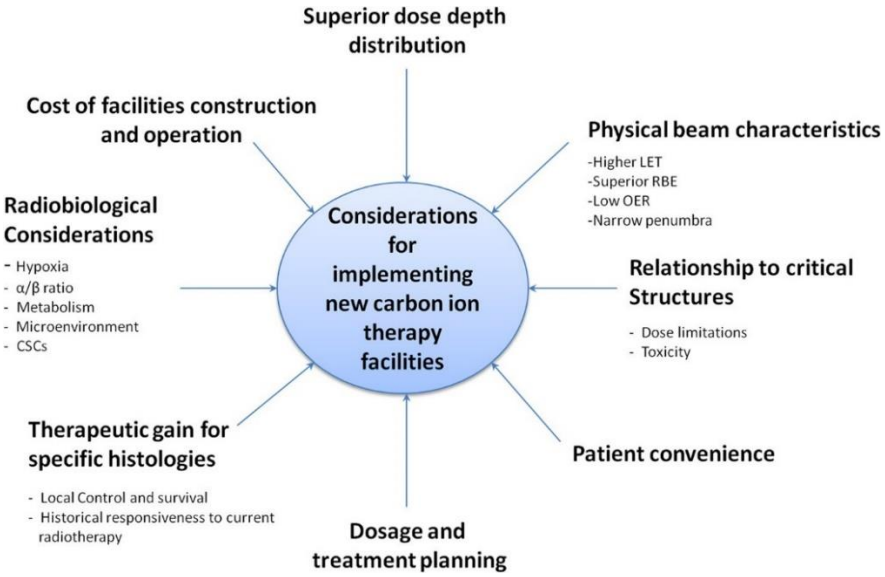

Figure 2.1 Considerations for the implementation of new carbon ion facilities. Image courtesy of [7]

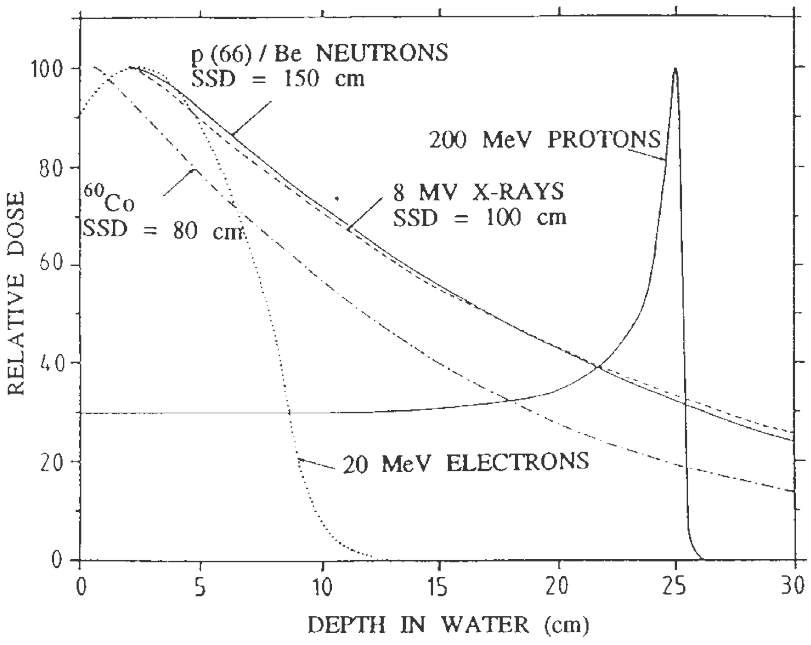

Figure 2.2 Depth dependence of the deposited dose for different radiations. An inverted dose-depth distribution is clinically much more favorable than an exponentially decaying distribution. Image courtesy of [8].

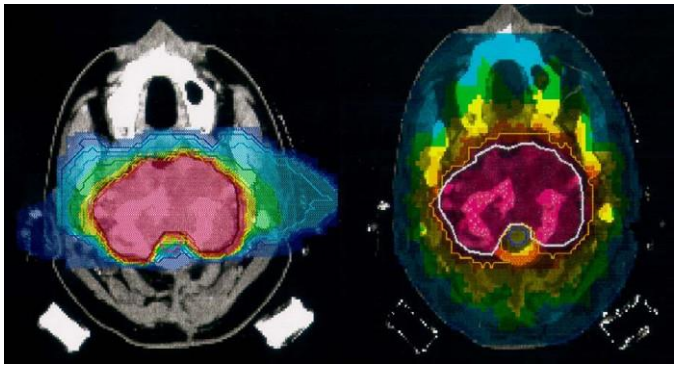

Figure 2.3 Comparison of treatment plans with 2 fields of carbon ion (IMPT—left panel) and with 9 fields of x-rays (IMRT—right panel). In both cases the conformity to the target volume is good but for carbon ions the dose to the normal tissues is much smaller. Image courtesy of [10].

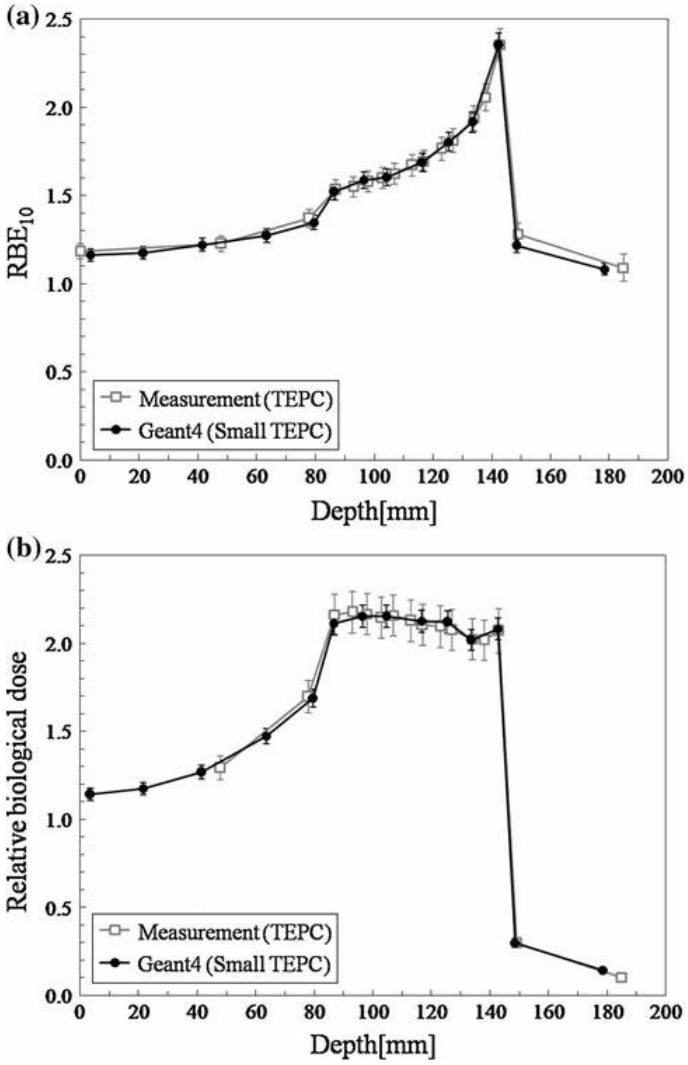

Figure 2.4 RBE_{10} profile (a) and biological dose (b) distribution obtained by measurement and Monte Carlo calculation with

GEANT4 for HIT with carbon ions. From the RBE profile it is apparent that the biological effectiveness of carbon ions varies in the SOBP and that RBE values are greater than unity. Image courtesy of [11].

For accurate treatment planning it is paramount to correctly assess the biological dose being delivered. To this end, it is essential to know which particle is to be found and at which depth along the beam path. This may prove tricky particularly when primary ^{12}C ions are concerned, since fragmentation plays an important role in the energy deposition process.

The primary way through which ^{12}C ions lose energy while traversing the biological tissue is continuous Coulomb interactions with atomic electrons, which are consequently excited. Nuclei may be left in an ionised state depending on the energy at stake. Inelastic nuclear collisions with nuclei are on the other hand rare, but they nonetheless turn out to be important when primary ions have clinical energies and substantial fragmentation is present. The secondary fragments produced in these inelastic reactions along the primary particles' path have generally the same velocity as primary ions but smaller Z, therefore a greater range. This results in the creation of a dose tail occurring after the Bragg Peak as clearly shown in Figure 2.5 and also an additional lateral dose due to scattering and a somewhat more complex radiation field [12]. Typically, light fragments such as protons and alpha particles are responsible the most for the dose deposited in the fragment tail whereas that due to heavier ones is mainly localized around the stopping point of the ^{12}C ions [13]. The fragments are also characterized by a different LTE resulting in a difference of RBE for the same delivered dose as well as an altered angular distributions with respect to primary ^{12}C ions. In fact, nuclear fragmentation, along with an increasing stopping power, is the reason why in the Bragg Peak region the RBE of primary carbon ions cannot be held as a constant, as shown in Figure 2.4. The presence of a fragment tail localized beyong the Bragg Peak and of an additional lateral dose, meaning that physical dose is being delivered to the healthy tissue

surrounding the target, can easily be considered as one of the main clinical drawbacks of the use of heavy ions in radiotherapy.

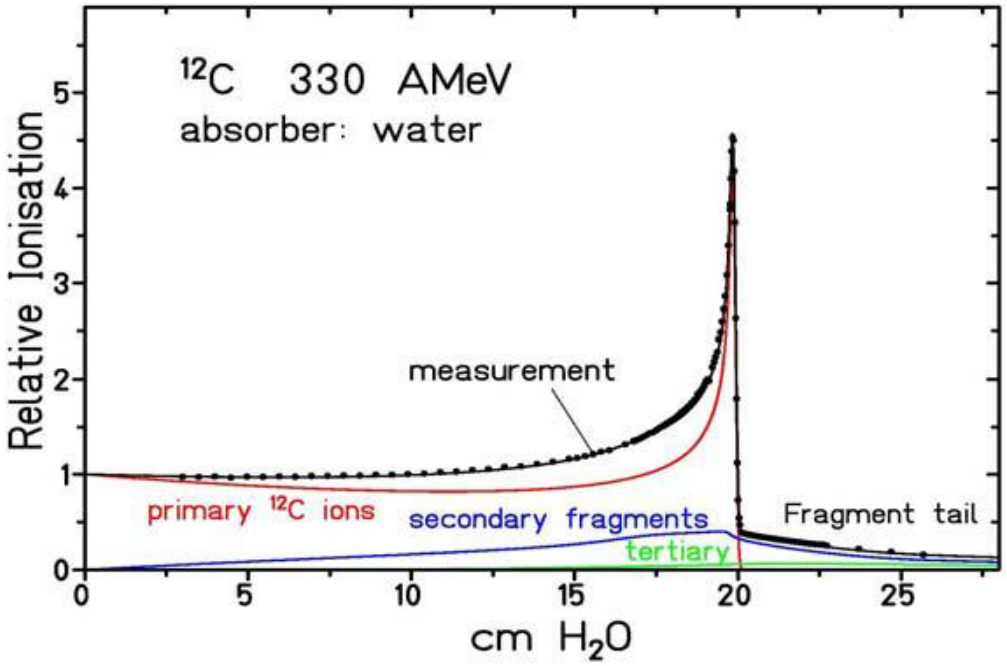

Figure 2.5 Bragg curve for 330 MeV/nucleon ^{12}C in water measured at GSI with large parallel-plate ionization chambers. The data points are compared to a model calculation (solid line). The calculated contributions from the primary particles (red line) and from nuclear fragments (blue line) are also shown. Image courtesy of [14].

The dose fraction delivered by fragments in the region before the BP is estimated to be about 20% for a 290 MeV/u carbon beam on a PMMA [15] and about 40% for a 400 MeV/u carbon beam on water [16].

In the end, an accurate knowledge of the primary ion beam fragmentation is necessary to obtain an accurate description of the biological effects inside and ouside the treatment volume. This problem will be further discussed in Chapter 4.

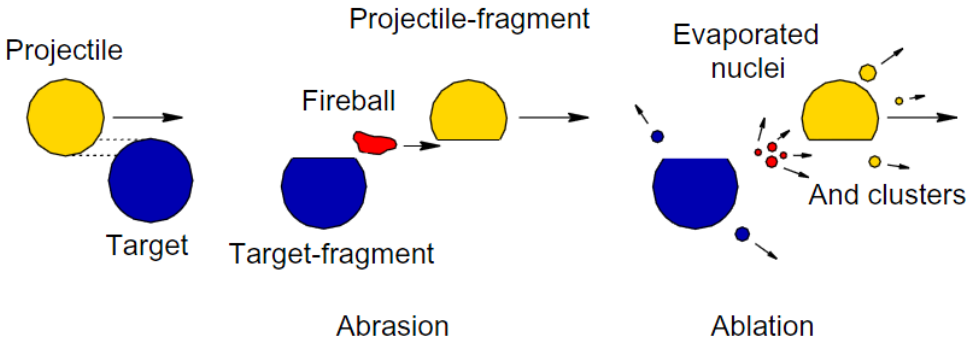

Figure 2.6 Basic steps of nuclear fragmentation. Image courtesy of [17].

2.2. Basic principles of microdosimetry

2.2.1. Introductory remarks

Radiation interacts with tissues depositing energy. The absorbed or physical dose *D*, expressed in units of Gray (Gy), that is Joules per unit mass (kg) of target volume, is defined by ICRU [18] as:

$$D = \frac{d\varepsilon}{dm},$$

where ε is the deposited energy and *m* is the mass of the target.

Broadly speaking, when depositing energy ionizing radiation can produce single and double strand breaks in the DNA helix, the latter of which is more likely to lead to the death of the cell, as illustrated in Figure 2.7. However, the severity of the cellular damage depends strongly on the particle track structure, or energy transfer density, as shown in Figure 2.8. The imparted energy per unit length of the particle track is described by the Linear Energy Transfer (LET). Different particles are characterized by different LET values and for example heavy ions have a high LET, typically ranging from several

tens to thousands keV/µm, whereas x-rays and gamma rays have low LET (up to a few keV/µm).

The Radiobiological Effectiveness (RBE) is introduced to compare the biological effects of different radiation types when depositing the same energy. The RBE is defined as the ratio of a dose of photons to a dose of any other particle to produce the same biological effect and depends on the type of irradiated tissue, particle type and energy, the absorbed dose and LET. In a more detailed picture, the RBE depends also on the early and late reactions following therapy [19]. In Figure 2.9 the dependence of RBE on LET can be appreciated.

In this framework, the aim of radiotherapy is to deliver to the malignant tissue in the target the so-called therapeutic dose necessary to kill the cancerous cells, while ideally sparing the surrounding healthy tissues. Even though in order to eliminate detrimental effects to heathy tissues surrounding the target volume the dose should ideally be zero both distally and laterally, there is always an unavoidable dose at least in the radiation entrance channel in the patient. Furthermore, based on the knowledge that biological tolerance is generally greatly increased when only a part of the healthy organ is included into the therapeutic dose volume, Treatment Planning Systems (TPSs) do ensure that the requirement for an inhomogeneous irradiation of the healthy tissue is met as strictly as possible. It is important to note that malignant and healthy tissues respond also differently to the same radiation, the latter in particular being slightly less radio-sensitive[2].

2 The reason behind this behaviour is not yet fully understood.

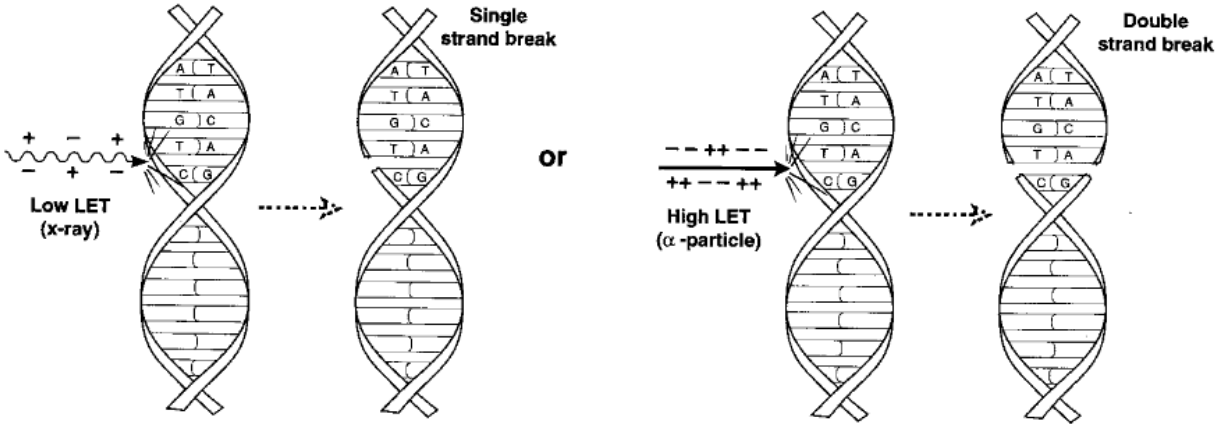

Figure 2.7 Illustration of DNA helix being damaged by incident radiation. Low LET particles such as x-rays are expected to produce single strand breaks while high LET particles such as carbon ions are expected to produce more biologically significant double strand breaks. Image courtesy of [20].

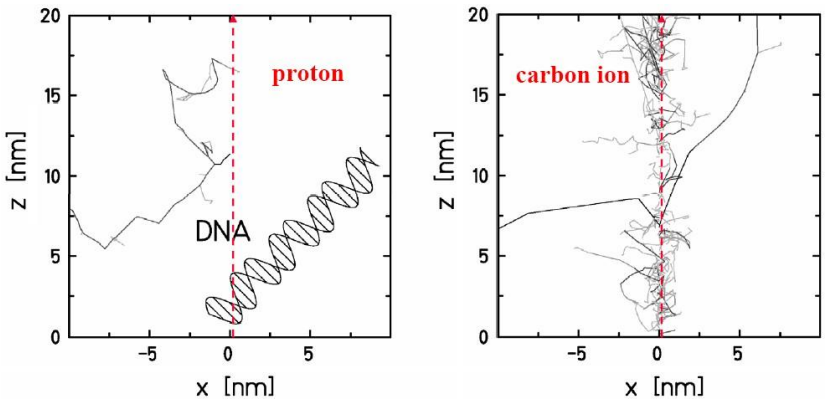

Figure 2.8. Structure of a proton and of a carbon track in nanometre resolution are compared with a schematic representation of a DNA molecule. In the picture it can be appreciated that the higher density of the secondary electrons produced by high LET primary carbon ions creates a larger amount of clustered DNA damage. Image courtesy of [8].

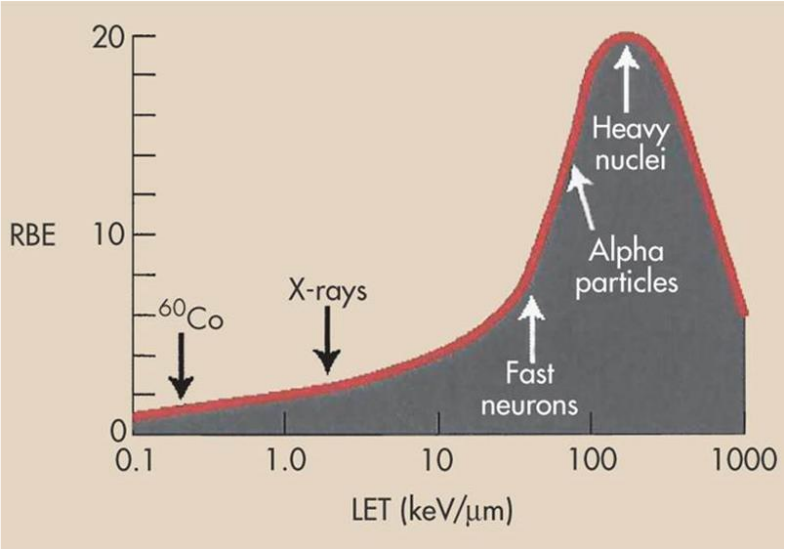

Figure 2.9. Dependency of RBE on LET. Image courtesy of [21].

In the clinical practice of Heavy Ion Therapy (HIT) the delivery of the physical dose to a macroscopic target volume is generally accomplished by superimposing several mono-energetic Bragg curves, each of which is associated to particles of a different kinetic energy. This result, as shown in Figure 2.10, in the so-called Spread Out of Bragg Peak (SOBP) which describes the whole physical dose being delivered to the patient. In particular the region of the SOBP where the highest doses are achieved is located in the tumor to kill the cancerous cells.

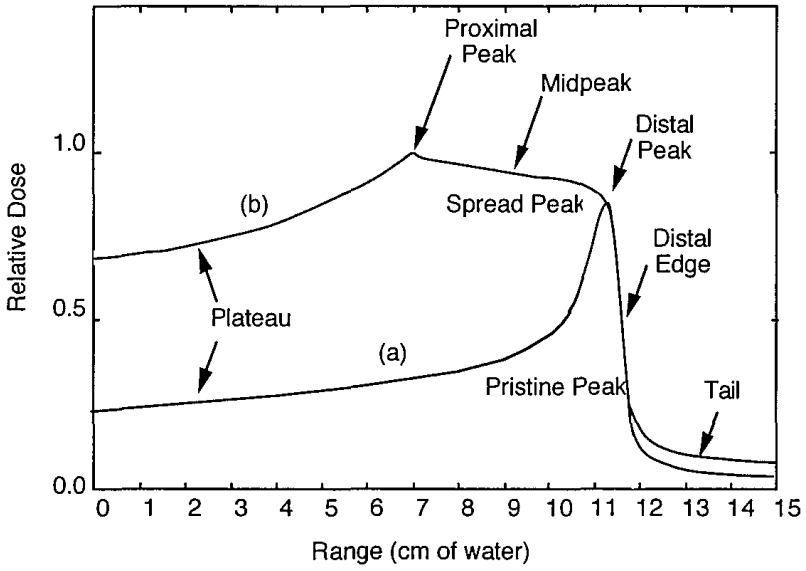

Figure 2.10 SOBP obtained by superimposing several mono-energetic pristine Bragg curves each of which is associated to particles of a different kinetic energy. In the SOBP it is possible to distinguish a plateau, a proximal peak, a distal peak, a distal edge and a tail.

The biological dose D_{bio}, expressed in Grays Equivalent (GyE) , is defined as

$$D_{bio} = RBE * D$$

where D is the physical dose. Since for primary carbon ions the RBE changes along the SOBP, it is necessary to have a non-uniform distribution of the physical dose D to obtain a flat biological dose over the target tumor volume, as pictured in Figure 2.11. The biological dose is calculated both for the irradiated volume and for critical structures close to the target as such that the TPS optimises the physical dose to be delivered to the target tumour and, at the same time, evaluates the secondary cancer risk to nearby healthy organs (Organs At Risk) which stand out of the treatment field.

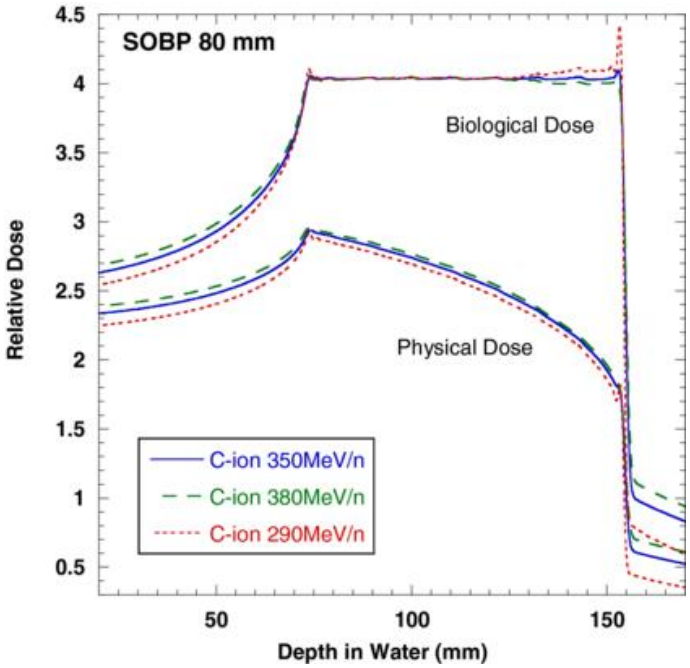

Figure 2.11 Physical and biological doses in a SOBP in water. An inhomogeneous physical dose is required to deliver a constant biological dose in the target tumor because the RBE varies with position in the SOBP.

2.2.2. Microdosimetry

Microdosimetry is the study of the energy deposition at the cellular level in the irradiated tissue by measuring the stochastic energy deposition events that occur in a micrometric site. These events can then be used for estimating the dose equivalent, or biological dose, and RBE of therapeutic and mixed radiation fields.

Formally defined by Rossi [22] as “the systematic study and quantification of the spatial and temporal distribution of absorbed energy in irradiated matter”, microdosimetry uses the concept of lineal energy, a stochastic quantity measured in units of keV/μm and formally defined by ICRU [18] as

$$y = \frac{\varepsilon}{\bar{l}}$$

where ε is the energy imparted to matter in a volume *V* by a single energy deposition event and $\bar{l}$ is the mean chord length of *V*, which is generally taken the size of a cell nucleus.

The stochastic nature of *y* is due to limitations in the definition of LET and other effects such as delta ray effect, variation in the LET value in the volume, energy and range straggling and chord length [23]. Being *y* a stochastic quantity it is possible to define both a probability distribution of lineal energy *f(y)* and *d(y)* as $d(y) = \frac{yf(y)}{\bar{y}_F}$, where the frequency mean lineal energy $\bar{y}_F$ is the first moment of *f(y):*

$$\bar{y}_F = \int_0^\infty yf(y)dy.$$

Another microdisimetric quantity is the specific energy *z*[3] defined as

$$z = \frac{\varepsilon}{m}$$

and measured in Gray, where m is the volume mass. As discussed for the lineal energy, similar microdosimetric distributions are defined for *z*, such as

$$d(z) = \frac{zf(z)}{\bar{z}}.$$

For a small volume the absorbed dose equals the mean value of the specific energy, that is

$$D \cong \lim_{m \to 0} \bar{z}$$

where

$$\bar{z} = \int_0^\infty zf(z)\,dz.$$

3 The specific energy should not be confused with the absorbed dose, both measured in Gray, the first being a stochastic quantity.

Microdosimetric spectra are traditionally displayed as a log-linear plot with the ordinate being *yf(y)* such that the area under the curve delimited by two values of *y* is proportional to the fraction of events in this range of *y*. Similarly, if the ordinate being used is *yd(y)* the area is proportional to the dose deposited in the lineal energy interval considered hence equal area under different regions of the function *yd(y)* reflect equal doses.

Microdosimetry is particularly useful when applied to radiotherapy with a mixed radiation field such as fast neutron therapy (FNT), boron neutron capture therapy (BNCT), proton therapy and HIT. This happens because the radiation damage depends on the lineal energy only and not on the particle type. The application of microdosimetry to high LET radiation is detailed in the ICRU report 36 [18] and in Rossi [22].

2.2.3. TEPC

The energy deposited in µm-sized sites can be measured experimentally with a Tissue-Equivalent Proportional Counter (TEPC), a spherical detector filled with a tissue-equivalent gas shown in Figure 2.12. The energy deposited in sites located in a tissue *t* and in a gas *g* is the same if the following equation is satisfied [24]:

$$\Delta E_t = \left(\frac{S}{\rho}\right)_t \rho_t d_t = \left(\frac{S}{\rho}\right)_g \rho_g d_g = \Delta E_g$$

where ΔE represents the mean energy deposited by a charged particle in a given tissue of density ρ, $\left(\frac{S}{\rho}\right)_t$ is the corresponding mass stopping power of the primary particles and d is the diameter of the considered sphere.

It should be remarked that the energy delivered by the particles traversing the detector fluctuates due to the stochastic nature of the energy deposition

process [18] therefore the lineal energy *y* changes from one event to another and a probability *f(y)* is instead measured.

The composition of the filling gas and that of the walls is to be chosen as close as possible to that of the tissue. Propane-based TEPCs are generally accepted as a good standard and represent the most frequently used layout [25]. The current state of the art for TEPC technology is represented by the mini twin TEPC with two sensitive volumes of 0.9 mm sizes [26].

An example of the filling gas composition is given in Table 2.1.

	H (%)	C (%)	N (%)	O (%)
Methane	10.2	45.6	3.5	40.7
Propane	10.3	56.9	3.5	29.3

Table 2.1 Elemental components (percent by weight) of a methane based and a propane based tissue equivalent gases. Table courtesy of [22].

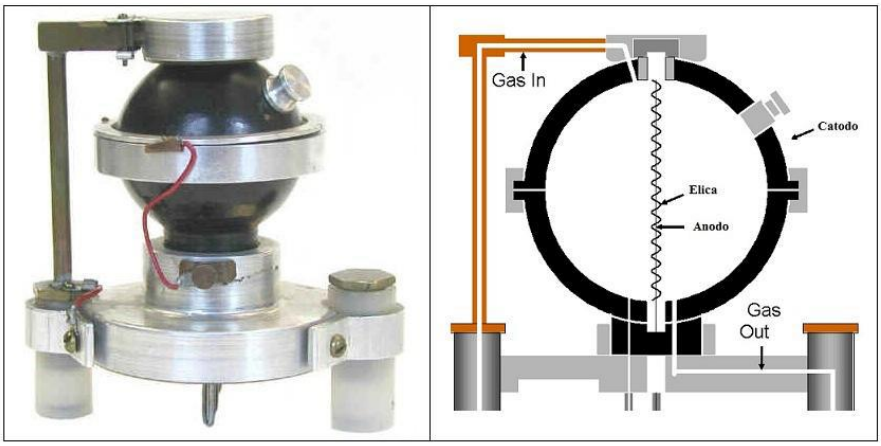

Figure 2.12 Picture and schematic of a Tissue Equivalent Proportional Counter.

A TEPC measures the distribution of ionizations created in the sensitive volume which is then converted into a distribution of energy imparted using a calibration factor. For a TEPC to correctly simulate tissue the Fano's theorem [4] must be satisfied. It should be noted that experimental measurements performed by TEPCs are affected by uncertainties and limitations, namely its relatively large physical size which limits spatial resolution and increases vulnerability to pile-up effects, the use of gas in the detection volume which leads to phase effects and wall effect errors and an inability to simulate an array of cells [22] [27]. This technology is not adequate for routine particle therapy Quality Assurance (QA) and when measuring *f(y)* in regions of radical change in the RBE as the distal part of the SOBP, due to the large size of the TEPC averaging the sub-millimetre RBE changes over the sensitive volume. Limitations on the use of this detector are comprehensively listed in ICRU report 36 [18] and in a systematic study by Lindborg [28].

As an illustration of a microdosimetric spectrum acquired with a TEPC, a *yd(y)* versus *log(y)* plot is shown in Figure 2.13 for a field due to mono-energetic neutrons. Three zones can be distinguished:

1. low-LET particles such as secondary electrons contribute to the first zone, from 0.3 to approximately 15 keV/μm;
2. higher LET particles such as recoil protons generated in the TEPC walls contribute to the zone from 3 to 135 keV/μm. The 135 keV/μm, a threshold always observed when spherical TEPCs are concerned and called proton edge, corresponds to the maximum ionization energy of the recoil proton, whereas the peak corresponds to the most probable energy transferred;

4 In a medium of constant atomic composition, the fluence of secondary particles is constant if the fluence of primary particles is constant. Under this condition the fluence is independent of the density variations provided that the interaction cross-sections and the stopping powers of concern are independent of density, a condition not always met due to polarization effects in solids [24].

3. heavier particles such as nuclear fragments produced in nuclear reaction processes or recoil nuclei contribute to the zone above 135 keV/μm.

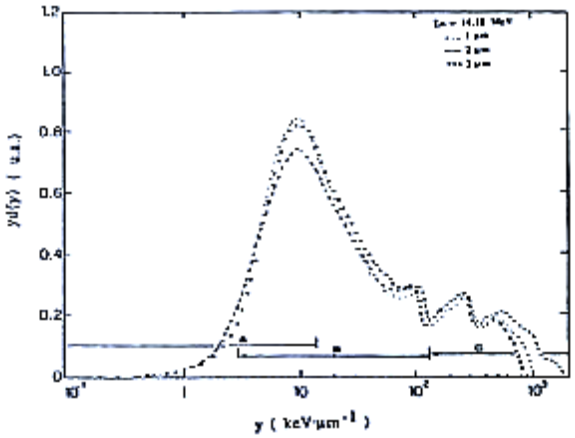

Figure 2.13. Microdosimetric spectrum *yd(y)* vs *log(y)* obtained by irradiating a spherical TEPC simulating sites of 1, 2, 3 um of diameter with 14.18 MeV mono-energetic neutrons. Three zones are highlighted: (A) low LET, (B) intermediate LET, (C) high LET. Image courtesy of [18].

Silicon based detectors offer significant advantages over TEPCs, namely a higher spatial resolution, a small size and the potential for real time read-out which make them well suited to radiation therapy QA for physical dose, dose equivalent measurements and RBE determination by means of the MKM model (see section 2.4). Because of the limited size of the sensitive volume a solid state detector would not be affected by deleterious averaging effects over regions where the physical dose is characterized by rapid build-ups, in contrast to TEPCs [29].

2.3. ΔE-E telescope detectors

In order to overcome known limitations in the use of common TEPCs, namely they poor performance under particle currents typical of clinical beams especially when hadron beams are concerned, and of miniaturized TECPs, which are still difficult to use [30], a two-stage silicon telescope detector has been developed over the last years by the research group lead by S. Agosteo and A. Fazzi at Politecnico di Milano. Being a solid state detector, it also possesses the advantages of a higher spatial resolution [31] when compared to TEPCs.

This novel monolithic silicon ΔE-E telescope detector, shown in Figure 2.14, consists of a ΔE sensitive volume whose thickness (2 μm) is much smaller than the path length of incident particles [32][5]. The ΔE stage can be used to determine the LET of the incident particles and it is in principle a solid state microdosimeter. The acquired microdosimetric spectra can then be used to evaluate the RBE profile using the Microdosimetric Kinetic Model (MKM), as described in the following section. The ΔE stage is coupled with the E stage, with a thickness (500 μm) bigger than the range of the incident particles. If the particles do not stop in the E stage, the device is effectively operating as a ΔE-ΔE detector. The information of LET in the ΔE stage coupled with the total energy deposition in the E stage allows to identify the particle. Since the telescope is able to discern the different types of particles present in the HIT radiation field, it is also possible in principle to estimate the partial contribution of each particle type to the RBE. It should be remarked that to obtain microdosimetric spectra from the ΔE stage signal comparable with those acquired with a TEPC, the distribution of the energy imparted in the silicon needs to be corrected for tissue equivalence.

The ΔE-E telescope has a titanium oxide dead layer of about 0.24 μm on top of the ΔE stage which has been found to affect the response of the detector at the lowest energies [30] [33]. The minimum detectable energy is

5 The range for a ^{12}C ions with energy 290 MeV/u in silicon is approximately 90 mm [32].

limited to approximately about 20 keV by the electronic noise, which means that the ΔE-E telescope detector can identify high LET particles only [34].

Even though for the sole purpose of identification of low-energy high LET particles just the ΔE stage would prove sufficient, its thickness of the order of microns can be tricky to accomplish on a freestanding layer leading to construction difficulties and the detector being too fragile [35]. This problem is instead easily to overcome with a monolithic ΔE-E probe constructed from a single silicon wafer [36]. The two ΔE and E stages are thus made out of a single silicon wafer and they share a deep P^+ electrode obtained through a high energy ion implantation which acts as a watershed for the charge collection processes [30]. A thin metallised N^+ layer is used as the entry window for the ΔE stage, which to fully deplete the telescope is biased at +5 V. The N^+ contact of the E stage is biased at + 100 V relative to the P^+ buried layer instead [37].

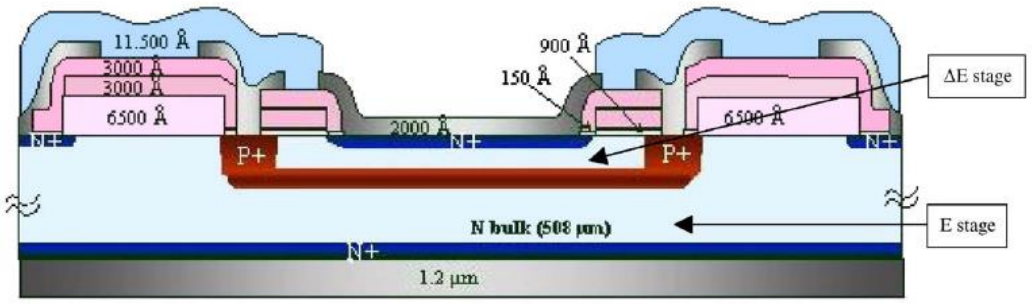

Figure 2.14. A schematic of a solid state monolithic ΔE-E telescope detector. The E stage and the ΔE stage are separated by a P+ electrode. Thin N+ layers are used as contacts for both the ΔE stage and the E stage. The detector is operated biased. Image courtesy of [38].

The pulses generated in the two stages, both of which are biased, contain information about the amount of energy deposited in the silicon and are collected and amplified by two independent electronic chains and acquired by a two-channel ADC in coincidence mode in order to maintain the time correlation between the ΔE and E signals.

The energy deposition in the two stages can be mapped into a 2D ΔE-E plot, an example of which is given in Figure 2.15 and Figure 2.16, where the energies deposited in the ΔE layer are plotted against either the energy deposited solely in the E stage or the energies deposited in both the ΔE and the E stages. Since energy deposition events produced by different charged particle types occupy distinct regions or loci in this 2D map, the ΔE-E telescope can be effectively used to characterise the secondary radiation field of a ^{12}C ions beam which generally comprises a variety of nuclear fragments.

In the past years, the response of a ΔE-E telescope when irradiated with heavy ions beams has been fairly studied [39] [40] [34] and the detector is nowadays evaluated as a possible alternative and improvement over TEPCs for microdosimetric spectra measurements for HIT.

It should be remarked that measurements close to the field edge and detailed microdosimetry along the BP and SOBP as obtained with a ΔE-E telescope would be impossible with a TEPC, which lacks the sub-millimetre spatial resolution of the telescope.

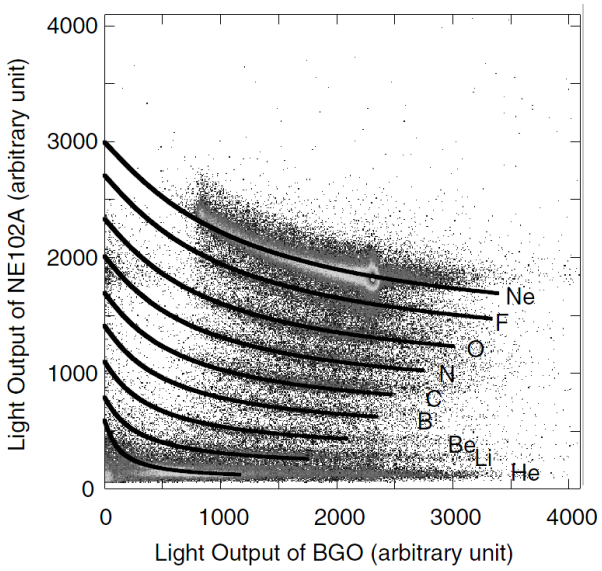

Figure 2.15. Example of the ΔE-E telescope response when irradiated with 400 MeV/nucleon 22Ne and plotted in a ΔE-E 2D plot, the NE102A being the ΔE layer and the BGO being the E layer of the telescope. Image courtesy of [15].

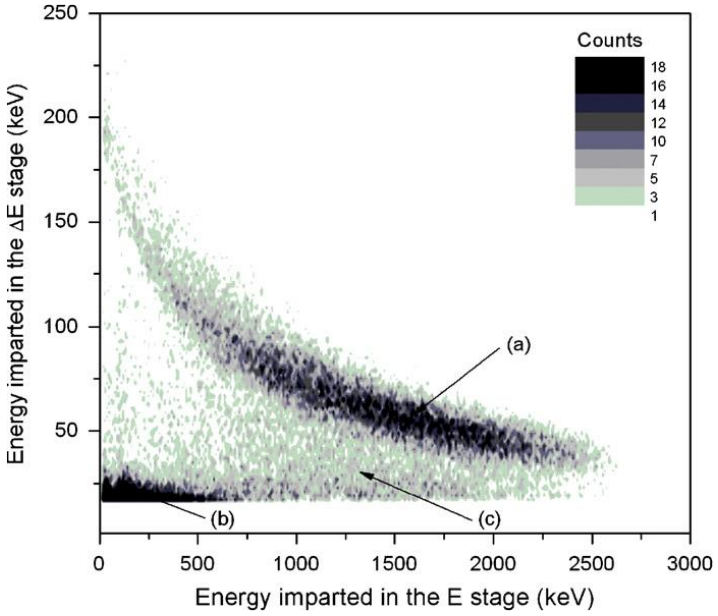

Figure 2.16. ΔE-E plot acquired with a pixelated silicon telescope when irradiated with 2.7 MeV mono-energetic neutrons. Three different regions can be distinguished based on LET: (a) high-LET recoil protons, (b) low-LET secondary electrons, (c) intermediate region. Image courtesy of [34].

A comparison between microdosimetric spectra acquired with a TEPC and with a silicon ΔE-E monolithic telescope, both irradiated with 2.7 MeV mono-energetic neutrons, was described by Agosteo et al, 2006 [41] and some discrepancies were found especially in the high-energy part of the spectrum. Those discrepancies were ascribed to geometrical effects due to the ΔE stage having a sensitive area not comparable to the length distributions of the particles' tracks [41]. Therefore to minimize such geometrical effects a second configuration of the ΔE-E telescope detector was developed and described by Agosteo et al, 2008 [34] and it is shown in Figure 2.17. In this configuration the ΔE stage of the detector is effectively constituted by a matrix of cylindrical ΔE stages of micrometric dimensions, each one about 2 µm in thickness and 9 µm in diameter separated by a pitch of 41 µm. Each ΔE stage is surrounded by a guard of 14 µm in diameter which has the effect of confining the sensitive volume laterally. The ΔE sensitive volumes were rendered of comparable dimensions to those of the sites simulated with a

cylindrical TEPC. The ΔE stages are coupled with a single E stage, 500 μm thick. This configuration was used in the experiment detailed in chapter 5 and is generally referred to as a ΔE-E pixelated telescope detector in contrast to the monolithic configuration.

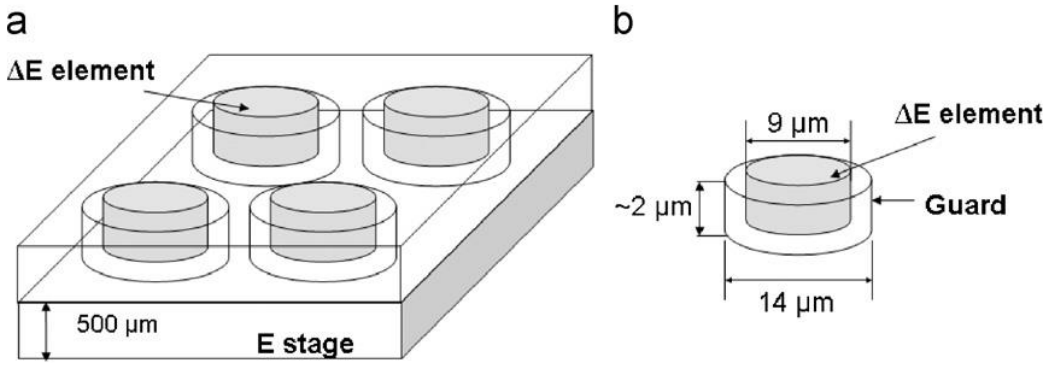

Figure 2.17. Schematic of a pixelated silicon telescope detector with the E stage and the pixels constituting the ΔE layer. A single pixel is pictured on the right detailing the surrounding guard. Image courtesy of [34].

A further non-pixelated configuration, which has been used in the experiment detailed in chapter 6, has been developed in which the titanium dead layer on top of the ΔE layer has been substituted with a silicon oxide dead layer. Titanium, which has a much higher Z with respect to Oxygen, is in fact expected to disturb more the incoming field. On the other hand the detector is expected to be subject to a much higher radiation damage in this new configuration.

2.4. The MKM Model

The RBE is an input to the clinical TPS to define the HIT delivery parameters to the patient. RBE is usually determined by means of experiments with different cell lines irradiated with different particles beams [42]. The Microdosimetric Kinetic Model (MKM), developed at HIMAC, Japan [43] [9] [44] [11] [45] was originally developed to calculate the survival curves of HSG tumour cells in response to treatment with mono-energetic heavy ions beams [11] and the RBE was calculated from the microdosimetric spectra of the lineal energy as the quotient of the energy imparted in a single energy deposition event by the mean chord length. It was subsequently shown that a modified MKM, which considers the over-killing effect in the high-LET region, can calculate the RBE also for a SOBP for carbon ions [46].

In the modified MKM the survival curves can be estimated using a saturation parameter for correction of the saturation of the MKM, in other words using the dose-mean lineal energy corrected for saturation. In particular the surviving fractions S of the HSG is expressed by the linear-quadratic model in function of the dose D and of the parameter α, the latter being

$$\alpha = \alpha_0 + \frac{\beta}{\rho \pi r_d^2} y^*$$

with the following parameters:

$\alpha_0 = 0.13\ Gy^{-1}$ as a constant that represents the initial slope of the survival fraction curve in the limit of zero LET.

$\beta = 0.05\ Gy^{-2}$ as a constant independent of the LET

ρ is the density of the tissue

$r_d = 0.42\ \mu m$ is the radius in the sub-cellular domain the MKM

y^* as the saturation-corrected dose averaged lineal energy to consider the over-killing effect and is a measurable physical value calculated with the saturation parameter $y_0 = 150\ keV/\mu m$ as in Tamura et al [11] and Linh et

al [37] to match the calculation method used at HIMAC in experiments with the TEPC.

The aforementioned equation establishes a relation between y^* and α irrespective of the ion species which implies that an excessive local energy deposition is inefficient in promoting a given biological effect [18] and ultimately leads to a reduction of the RBE itself, an effect known as the saturation effect.

The RBE_{10} is then estimated as

$$RBE_{10} = \frac{2\beta D_{10,R}}{\sqrt{\alpha^2 - 4\beta \ln(0.1)} - \alpha}$$

where $D_{10,R} = 0.5\ Gy$ is the 10% survival dose of the reference radiation[6] for HSG cells [46]. The resulting RBE_{10} is used to evaluate the biological dose in order to obtain a SOBP over the target volume. The RBE_{10} determined with the MKM model has been compared to cellular experimental measurements [42].

These and other parameters of the modified MKM as used in Chapters 5 and 6 are further detailed in Tamura et al [11]. As in the analytical calculations for the RBE values carried out by Tamura et al [11], the statistical errors of the calculations in the simulated results for the RBE_{10} in this thesis work was the standard deviation estimated form multiple calculations under same conditions.

6 200 kVp X-rays.

3. Methodology

3.1. The simulation study

In this thesis work the GEANT4 Monte Carlo code has been used for the purpose of characterizing the response of the ΔE-E telescope detector both at the CNAO HIT beam line and at the ANU 14UD facility.

In a first stage the accuracy of the GEANT4 physics models in describing the Bragg Peak of ^{12}C ion beams is assessed by comparing simulated results against experimental measurements available in the literature. This study, detailed in Chapter 4, is aimed at quantify the reliability of the simulated results presented in Chapter 5 and Chapter 6.

At the beginning of Chapter 5 the CNAO HIT radiation field is characterized in terms of energy deposition and secondary fragments in a water phantom, a box of 30 cm side as it is typically used in clinical Quality Assurance (QA). This study is preliminary to the characterization of the ΔE-E telescope detector response examined using ΔE versus ΔE+E energy depositions plots. As already detailed in Chapter 2, the telescope is operated in coincidence, meaning that only particles depositing energy in both stages are counted as hits. As a side note, secondary particles generated in the detector itself have their energy deposition added to that of their respective parent particles which are incident on the device. The detector response is studied by having it placed both in-field, meaning inside the incident ^{12}C beam field as shown in Figure 3.1, and out-of-field with the detector always placed face-on with respect to the primary beam as shown in Figure 3.2 and Figure 3.3. This latter out-of-field configuration is relevant in the clinical practice for the evaluation of the dose delivered to healthy tissues surrounding the tumour, which is the target of the treatment. The simulated number of particles is varied for each depth and position combination in order to obtain statistically meaningful results.

Finally, the ΔE stage of the telescope is characterized for microdosimetry measurements[7]. Using as a mean chord length the thickness of the ΔE silicon layer itself along the ^{12}C ion beam direction, microdosimetric spectra are obtained both in-field and out-of-field. Furthermore, the RBE10 values for various depths in the water phantom are estimated using, as discussed in Chapter 2, the MKM modified model implemented in a MATLAB® macro.

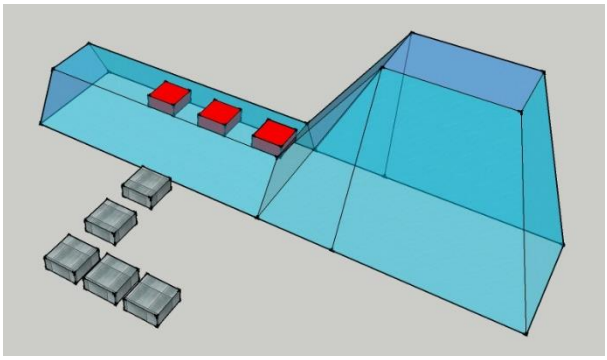

Figure 3.1 In-field configuration: the detector is placed inside the field due to primary particles, at different depths along the beam path (red boxes). In the figure red and grey boxes represent detector positions whereas the blue solid represents the 3D SOBP and plateau in the water medium target due to primary carbon ions coming from the figure's upper-left angle. It should be noted that the detector is to be placed at each position one at a time and not at all of them simultaneously, in order to prevent perturbation of the radiation field. In this figure, grey boxes are detector positions out of field, as explained in Figure 3.2.

[7] Provided the incoming primary beam is normally incident to its surface

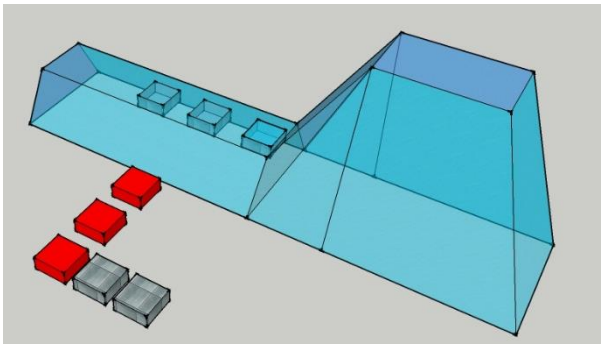

Figure 3.2 Out-of-field configuration: the detector is placed outside the field due to primary particles, at different distances from the axis (red boxes). In the figure red and grey boxes represent detector positions whereas the blue solid represents the 3D SOBP and plateau in the water medium target due to primary carbon ions coming from the figure's upper-left angle. It should be noted that the detector was placed at each position one at a time and not at all of them simultaneously, in order to prevent a distortion in the radiation field analysis.

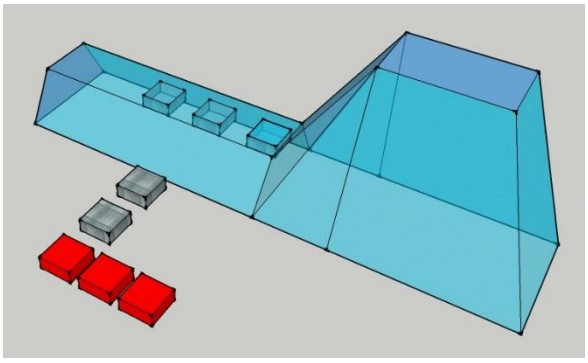

Figure 3.3 Out-of-field configuration: the detector is placed outside the field due to primary particles, at different depths along the axis but at a fixed distance from the axis (red boxes). In the figure red and grey boxes represent detector positions whereas the blue solid represents the 3D SOBP and plateau in the water medium target due to primary carbon ions coming from the figure's upper-left angle. It should be noted that the detector was placed at each position one at a time and not at all of them simultaneously, in order to prevent a distortion in the radiation field analysis.

3.2. Overview of the Geant4 Toolkit

A Monte Carlo method consists of mathematical techniques for sampling values of a random variable, given its cumulative distribution function [22]. Monte Carlo simulation techniques, nowadays used in many areas of scientific research and industrial development as investigation tool, are probably the most accurate method of describing particle transport within a medium [47] and they represent a tool to obtain a 3D description of energy deposition distributions, radiation field characterizations and related parameters [48]. The accuracy of the results is among the reasons Monte Carlo simulations are successfully applied to radiotherapy and HIT in particular to retrieve quantities which would not be easily measured in experiments, a key point confirmed by recent papers when GEANT4 is used [49] [48] [50] [51] [52].

Generally speaking, computer-generated particle tracks are consistent with the reality if the physics underlying the particle processes is well described and, in particular, particle interaction cross sections need to be accurately known. Therefore the choice of the physics models most suitable for a given application is of the foremost importance.

Given the amount of computational time needed for the simulations, the GEANT4 Toolkit and other Monte Carlo codes are not generally directly employed for clinical Treatment Planning Systems (TPSs), but are instead used to systematically generate data of physical quantities (e.g. dose kernels) which will in turn constitute input values for the TPSs [53] [54] [55].

GEANT4 is a general-purpose Monte Carlo simulation Toolkit initially developed for High-Energy physics and currently widely used for applications ranging from space science to medical physics. GEANT4 is developed and maintained by an international collaboration. It can be used for radiotherapy applications to calculate fluencies, for dose verification of TPSs used in the clinical practice, to characterise and optimise novel detectors and to understand specific aspects of experimental

measurements. For the scope of improving the accuracy of the biological dose distribution in TPSs, various studies have shown that GEANT4 can be a useful investigation tool for HIT [56] [13] [53] [48] [50]. The Toolkit has also been recently validated with respect to published experimental measurements by reproducing the Bragg Peak in water and polyethylene along with the secondary fragment yields for different energy ranges of ^{12}C ions [52] [53] [48] [51] [50]. Nevertheless, the Toolkit validation process for applications in HIT is still incomplete and needs to be complemented with more in-depth studies especially at the microdosimetric level [48] [53].

For the scope of this thesis work, the software ROOT [57] was used for the analysis of the GEANT4 simulated results.

The simulations discussed in this thesis work were performed with GEANT4 version 10.00 with an application originally developed by S. Guatelli and D. Bolst, Centre for Medical Radiation Physics, University of Wollongong, and adapted to each of the case studies under investigation.

Three mandatory classes need to be implemented in a GEANT4 application, defining the geometry, the beam settings and the physics models. The G4DetectorConstruction class defines the geometry and the materials involved in the simulation set-up such as those concerning detectors, targets and all volumes present in the physical set-up, whereas the G4PrimaryGeneratorAction class is used to define the incident radiation field in terms of particle type, energy, momentum and point of origin. A third class, the G4PhysicsList, is used to activate the set of physics processes and models relevant to a given particular use in order to effectively model particle interactions such as electromagnetic and hadronic processes.

GEANT4 offers alternative physics models to describe both electromagnetic and hadronic physics processes and it is up to the user to decide which physics approach fits the simulation requirements in terms of accuracy of the results and computing time. A detailed description of all physics models included in GEANT4 is given in the Physics Reference Manual [58] whereas

a brief discussion of the models activated in the GEANT4 simulations performed in this thesis is postponed to the chapters where each case study is analysed.

An important parameter that may be set in the PhysicsList is the cut, which although used to fix the energy threshold of production of secondary particles, in GEANT4 is implemented as the corresponding particle's range. If a secondary electron has a range bigger than the cut, it is originated and tracked in the simulation, otherwise its kinetic energy is considered local energy deposition and the particle is not tracked [59]. It is fundamental to appropriately set the cut based on considerations such as the accuracy of simulation results, which would require a lower cut, and the need to limit as much as possible computing time, which would be possible by setting a higher cut. In GEANT4 the CutPerRegion is also available to define different cuts for different geometrical components belonging to the same simulated experimental set-up.

4. Validation of GEANT4 for Heavy Ion Therapy

This chapter is devoted to the validation of the GEANT4 physics models for Heavy Ion Therapy, a fundamental step towards the assessment of the accuracy of the simulation results presented in Chapter 5 and Chapter 6.

Various experiments have been carried out in the past years to measure the range of the primary carbon ions and the characteristics of the secondary nuclear fragments [15] [60] [52] [48] and it has been shown that GEANT4 is capable of reproducing accurately the experimental Bragg Peak position for carbon ion beams of energies of clinical interest, both in water and PMMA[8] [50] [48]. Recently GEANT4 has also been validated with respect to experimental measurements in the case of low-energy carbon ion beams in the range from 60 to 100 MeV/nucleon [49] [51] comparing alternative nuclear reaction physics models (QMD, BIC, INCL++). Even though the validation of the GEANT4 physics models for Heavy Ion Therapy (HIT) is still far from being conclusive, these preliminary studies have shown that the INCL++ model gives more realistic predictions for fragment production rates and their energy spectra when compared over alternatives [49] [51].

This chapter is dedicated to the comparison between the experimental measurements for the Bragg Peak position due to carbon ion beams in water performed at GSI and documented in Haettner [61] and the GEANT4 simulated results. Figure 4.1 shows the experimental set-up adopted in Haettner [61] for measuring the absorption of primary incident carbon ions of energy 200 MeV/nucleon and 400 MeV/nucleon in water. This benchmarking is particularly important for HIT because:

[8] PMMA, also known as Lucite or Perspex, is used as a substitute for human tissue whenever the latter cannot be used. Water is also used as a substitute, mainly because it has radiation absorption properties sufficiently close to those of human tissue [18]. Typical PMMA composition is given in Table 4.1

- the energy of the carbon ions beams is of clinical interest;
- the experimental Bragg Peak position is determined with a millimeter spatial resolution.

In fact it has been shown that for patient treatment a high accuracy for both the dose value (3%) and its location (1 mm uncertainty) in the target is necessary [52]. Large physics uncertainties originate mainly in the cross sections of inelastic reactions of primary carbon ions with nuclei of the tissue, a process which gives rise to fragmentation [56]. The proportion of primary carbon ions reaching the Bragg Peak without occurring a nuclear interaction in the tissue decreases significantly along their path, as shown in Table 4.2. It is worth recalling that different fragments with different energies and trajectories modify the dose distribution along the primary beam path, potentially questioning the high conformability of the carbon ions beam dose deposition. In particular, low-Z fragments are subject to larger scattering angles and are thus responsible for the spread of the dose both beyond the Bragg Peak and laterally. Also the RBE of produced fragments is different [51].

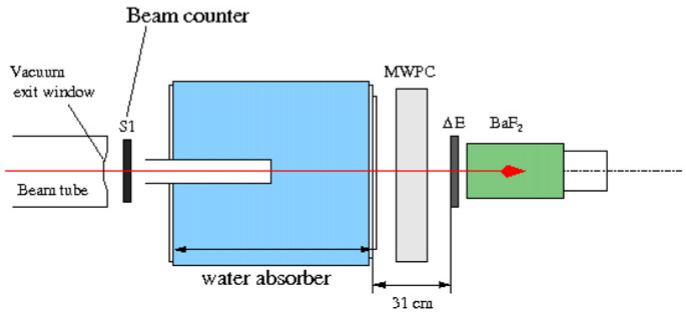

Figure 4.1. Experimental setup used for measuring the absorption of primary ^{12}C ions in water. Image courtesy of [61].

H	C	O	Density (g/cm^3)
8.05	31.96	59.98	1.31

Table 4.1. Standard PMMA composition used in the simulations. Mass percentage of each component is given.

Energy (MeV/nucleon)	100	200	300	400
N/No	0.86	0.66	0.45	0.27

Table 4.2: Proportion of primary carbon ions, with initial energy 100, 200, 300 and 400 MeV/nucleon reaching the Bragg Peak without occurring in a nuclear interaction in a thick water target. GEANT4 simulated results. Table courtesy of [62].

4.1. The Geant4 application

An application originally developed by Dr. Susanna Guatelli and David Bolst using GEANT4, version 10.0, was adapted to this case study.

The simulation world volume was modelled as a 3 m side vacuum cube containing a 35 cm side water box as to reflect the experiment carried out by Haettner [61]. The whole experimental set-up is depicted in Figure 4.2.

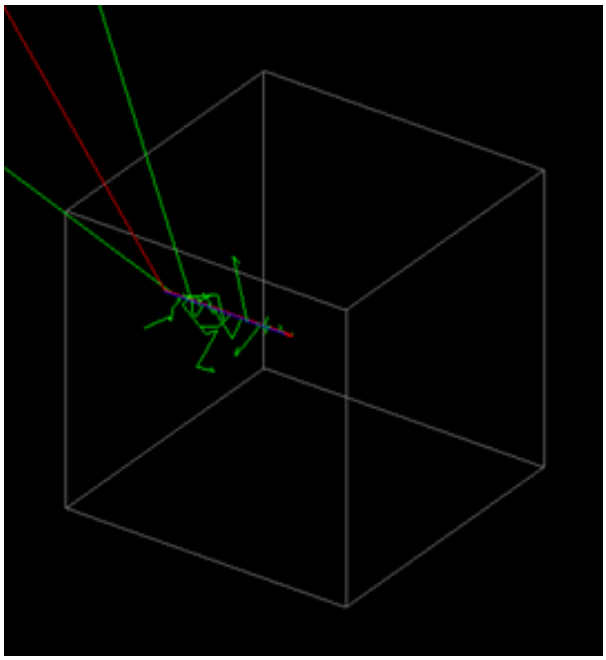

Figure 4.2. Experimental set-up of the GEANT4 simulation. The water box, is placed in the center of the world, is traversed by simulated particles' tracks.

The radiation field was simulated using a ^{12}C beam generated at 1 m from the phantom target surface along the x-axis, with initial direction normal to the phantom surface itself. The beam initial energy was set either to 200 MeV/nucleon or 400 MeV/nucleon, to match the reference experimental conditions described in Haettner [61]. The initial energy spread was modelled with a Gaussian distribution with a standard deviation of 2 MeV/nucleon for the 400 MeV/nucleon beam to match that of the experiment as detailed in Danielson's [63]. The initial spatial width of the beam was simulated by picking the originating position in the yz-plane from a Gaussian distribution with a suitable standard deviation σ given by

$$FWHM = 2\sqrt{2\ln 2}\sigma$$

The experimental FWHM was 4 mm for both the 200 and the 400 MeV/nucleon beams.

Since the position and shape of the Bragg Peak are determined in large part by the electromagnetic interactions of particles [48], alternative GEANT4 electromagnetic physics packages (*Standard, Low Energy* based on *Livermore* data libraries and, alternatively, *Penelope*) available with the GEANT4 toolkit to model electron, positron and photon interactions have been carefully considered. In particular, ionization and multiple scattering of heavy charged particles are modelled with one unique physics model. In this case the energy loss is modelled based on ICRU parameterizations (up to few MeV) and then Bethe-Bloch formula for higher energies [58]. GEANT4 then offers alternative physics lists to model electromagnetic interactions of charged particles and photons such as *Standard Package option 1, 2, 3, Livermore* and *Penelope* physics list as listed in Table 4.3. In this work all these alternative physics lists have been compared to the experimental measurements. It is important to notice that the different GEANT4 electromagnetic constructors adopt the same physics models to describe heavy charged particle interactions and the interactions of photons, electrons and positrons only are described differently.

Constructor	Comments
G4EmStandardPhysics	Default. Physics models valid between 1 keV and ~TeV
G4EmStandardPhysics_option1	The option "fMinimal" is used for multiple scattering step limitation, which provides accuracy and CPU performance.
G4EmStandardPhysics_option2	*G4WentzelVIModel* is used for muon multiple scattering, *G4KleinNishinaModel* used for the Compton scattering simulation
G4EmStandardPhysics_option3	ICRU73 based ion model; increased number of bins in physics table (220; 84 bins by default); *G4WentzelVIModel* is used for muon multiple scattering. *G4KleinNishinaModel* used for the Compton scattering simulation
G4EmLivermorePhysics	Physics models based on Livermore Evaluated Data Libraries. Physics models are valid between 250 eV and GeV scale.
G4EmPenelopePhysics	Physics models based on Penelope Monte Carlo code. Physics models are valid between 100 eV and GeV scale.

Table 4.3: Physics Lists EM constructors in GEANT4 10.0 [64].

The threshold of production of secondary electrons and positrons was set equal to 10 mm for the world volume and equal to 0.1 mm for the water box[9]. This cut was selected because it is 1/10 of the smallest voxel side of the phantom, where the energy deposition is recorded.

GEANT4 offers also alternative and complementary physics models to describe hadronic interactions. Broadly speaking, the inelastic interactions between primary carbon ions and nuclei in the tissue are commonly sub-divided into an initial fast stage when nuclei interact strongly with each other

9 As a reference, 1 mm in water corresponds to a kinetic energy of 350 keV for electrons and of 2.9 keV for photons [53].

(cascade), a pre-equilibrium phase when fast particles leave a highly-excited nuclei followed by a de-excitation process which brings the nuclei back to their fundamental state [50].

The GEANT4 binary cascade model, commonly referred to as *BIC*, is described in [58]. The model treats the inelastic collision between two nuclei as a sequence of individual nucleon-nucleon collisions in the region where the colliding nuclei overlap [50]. It is associated with a native handler provided by GEANT4 which chooses among three different statistical de-excitation models (*Fermi Break-up, Evaporation* and *Multi-Fragmentation*, depending on the A and Z of a given nucleus) to bring the nuclei to their fundamental state. The GEANT4 physics list *QGSP_BIC_HP* has been used in this work, including the *Binary Cascade Light Ion*, modelling ion inelastic interactions, an extension of the *BIC* model valid approximately from 80 MeV/nucleon to 10 GeV/nucleon [53].

The *Quantum Molecular Dynamic* model, *QMD* [65], is an alternative approach to *BIC* to simulate interactions between ions developed by Niita et al. [66]. It also uses the GEANT4 native de-excitation handler (*Fermi Break-up, Evaporation* and *Multi-Fragmentation*, depending on A and Z) and, compared to the *BIC,* it treats each nucleon of both the projectile and the target as a participant. Finally, in the *G4IonINCLXXXPhysics* (*INCL*) intra-nuclear cascade model the projectile is described as a collection of independent nucleons characterized by a Gaussian momentum and position distributions [51]. Some nucleons are considered as spectators whereas the others generate an intra-nuclear cascade in the target as described in Boudard [67].

4.2. Simulation results

In a first stage the Brag Peak was modelled by activating alternative electromagnetic physics list and no hadronic physics component. Figure 4.3 and Figure 4.5 show the results of these simulations respectively for 200 MeV/nucleon and 400 MeV/nucleon carbon ions beam. As expected, the results show no difference of significance concerning the Bragg Peak position.

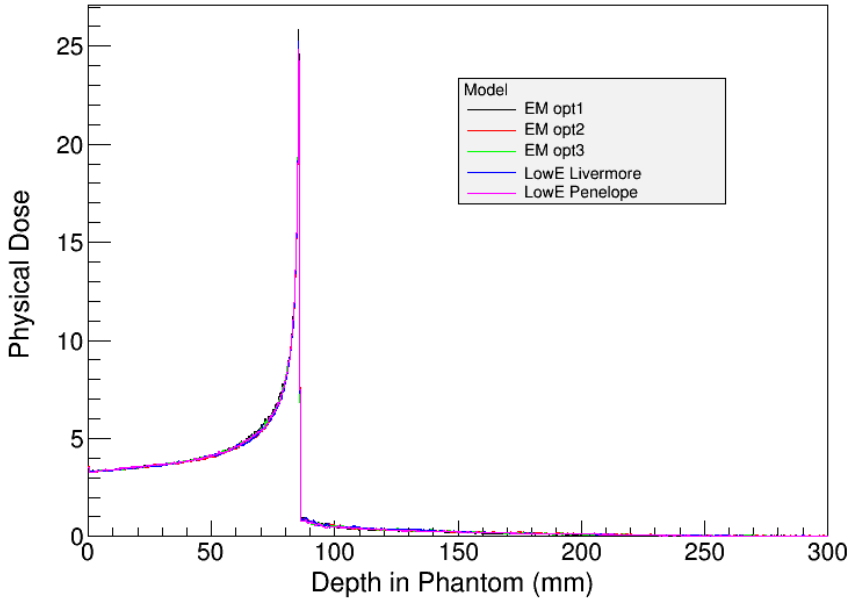

Figure 4.3: Bragg peak calculated activating different electromagnetic physics lists and no hadronic model for 200 MeV/nucleon carbon ions beam.

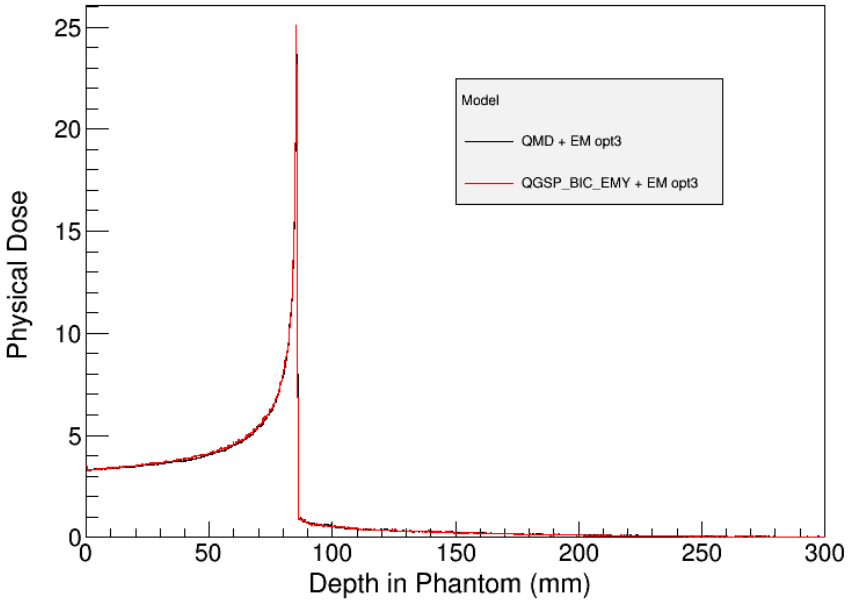

Figure 4.4: Bragg peak calculated activating different hadronic physics lists with *electromagnetic physics list option 3* for 200 MeV/nucleon carbon ions beam.

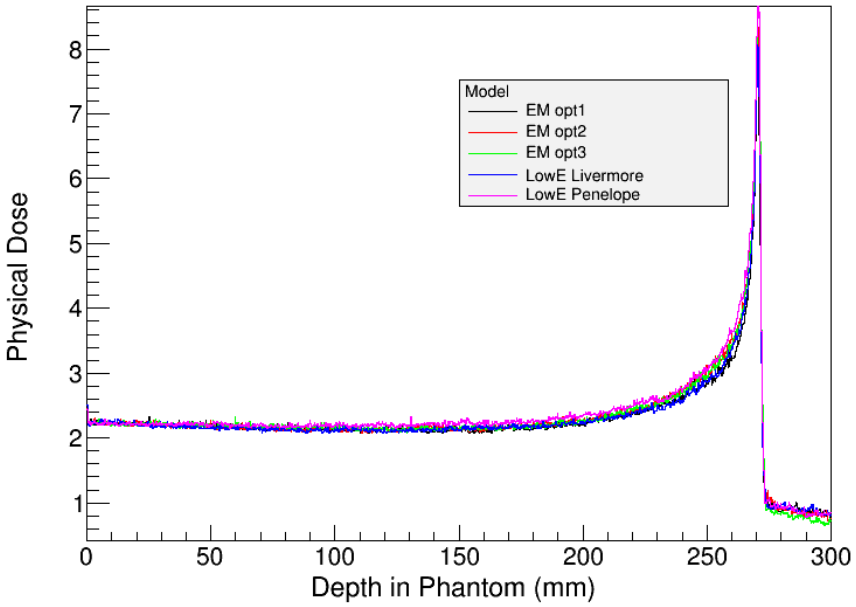

Figure 4.5: Bragg peak calculated activating different electromagnetic physics lists and no hadronic model for 400 MeV/nucleon carbon ions beam.

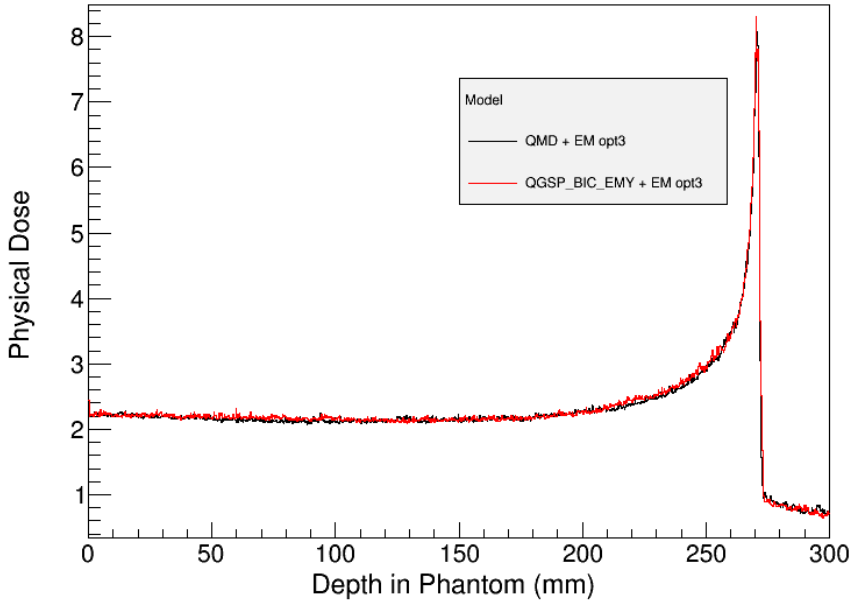

Figure 4.6. Bragg peak calculated activating different hadronic physics lists with *electromagnetic physics list option 3* for 400 MeV/nucleon carbon ions beam.

The second comparison has been performed using the *electromagnetic standard package option 3* and adding either the *QMD* or the *QGSP_BIC_HP* physics list to describe the hadronic physics. As expected, no change in the Bragg Peak position was found either. Results are shown in Figure 4.4 for the 200 MeV/nucleon primary carbon ions and in Figure 4.6 or the 400 MeV/nucleon primary ions. For the 400 MeV/nucleon, Figure 4.7 and Figure 4.8 show the percentage difference on the energy deposition along the Bragg curve obtained using QGSP, INCL++ and QMD as hadron physics models, the latter being set as reference.

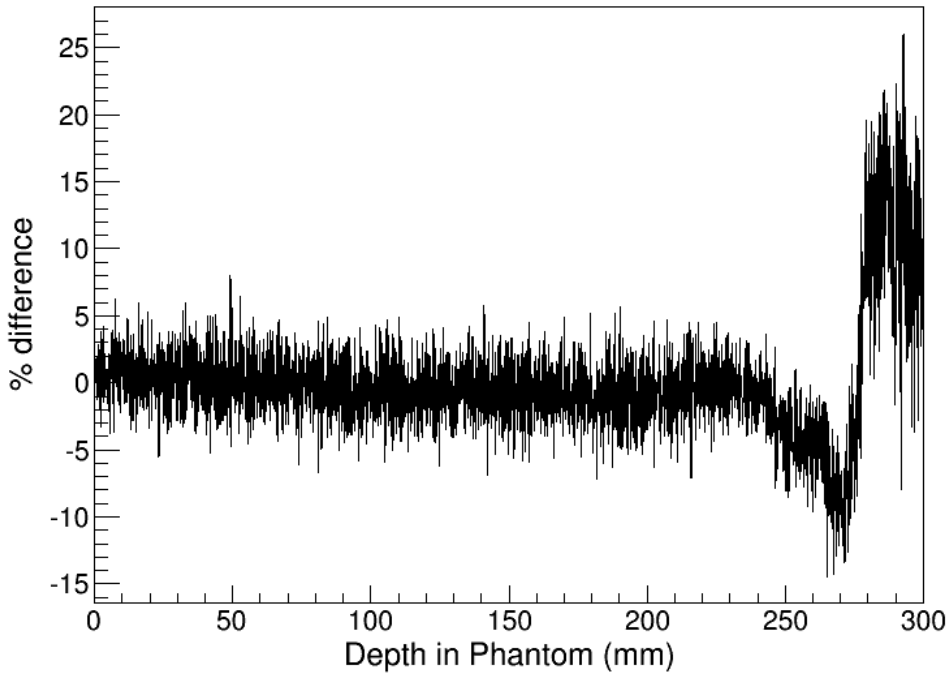

Figure 4.7. Percentage difference on energy deposition between *INCL++* and *QMD* physics lists, with *QMD* as a reference. The *electromagnetic standard package option 3* was selected for both the simulations as the electromagnetic model.

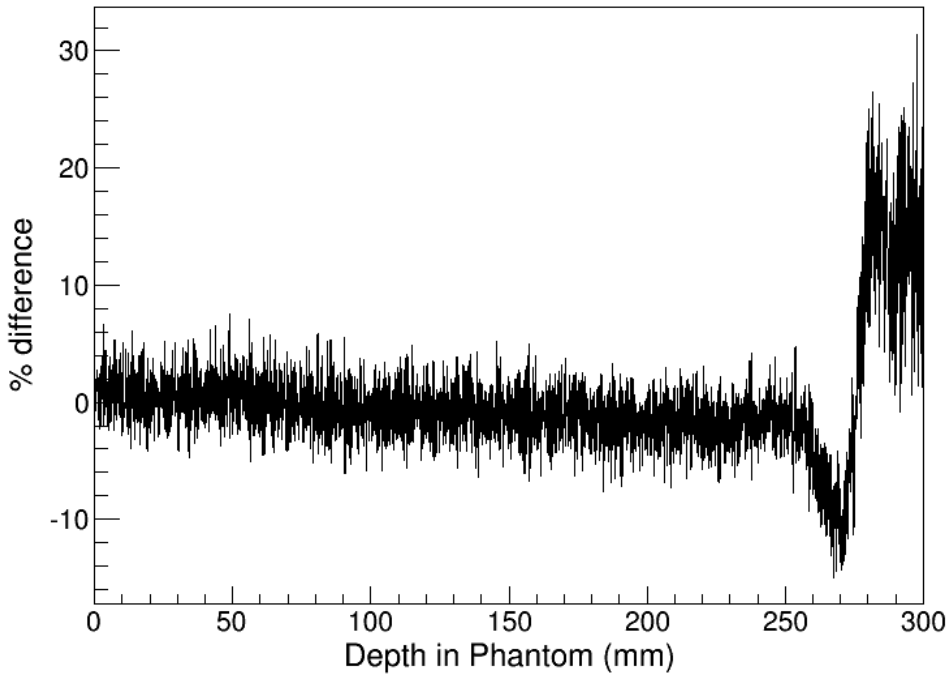

Figure 4.8. Percentage difference on energy deposition between *QGSP_BIC_HP* and *QMD* physics lists, with *QMD* as a reference. The *electromagnetic standard package option 3*

was selected for both the simulations as the electromagnetic model.

Even though there is no significant difference along most of the Bragg curve, there is a relevant mismatch in the tail of the curve where the dose is completely due to secondary fragments. This constitutes a clearly indication of the urgent need for further investigation on the accuracy of GEANT4 simulations concerning fragments yields and energy and angular spectra for carbon ion beams with clinical energy.

Having selected the *electromagnetic standard package option 3* coupled with the *QMD* model, which are currently recommended for HIT applications [49] [68], comparisons between the experimental results in Haettner [61] and GEANT4 simulations are shown in Figure 4.9 for the 200 MeV/nucleon beam and in Figure 4.10 for the 400 MeV/nucleon beam. The experimental accuracy on the Bragg Peak position is claimed to be of 1 mm [61] whereas for the simulated results it is 0.1 mm.

In conclusion, a good agreement was found for the 200 MeV/nucleon beam whereas the simulated Bragg Peak position for the 400 MeV/nucleon beam shows a position mismatch of a couple of millimeters, as already found by Danielsen [63]. This result indicates that there is room for improvement for the GEANT4 physics at the higher end of the clinical energies range.

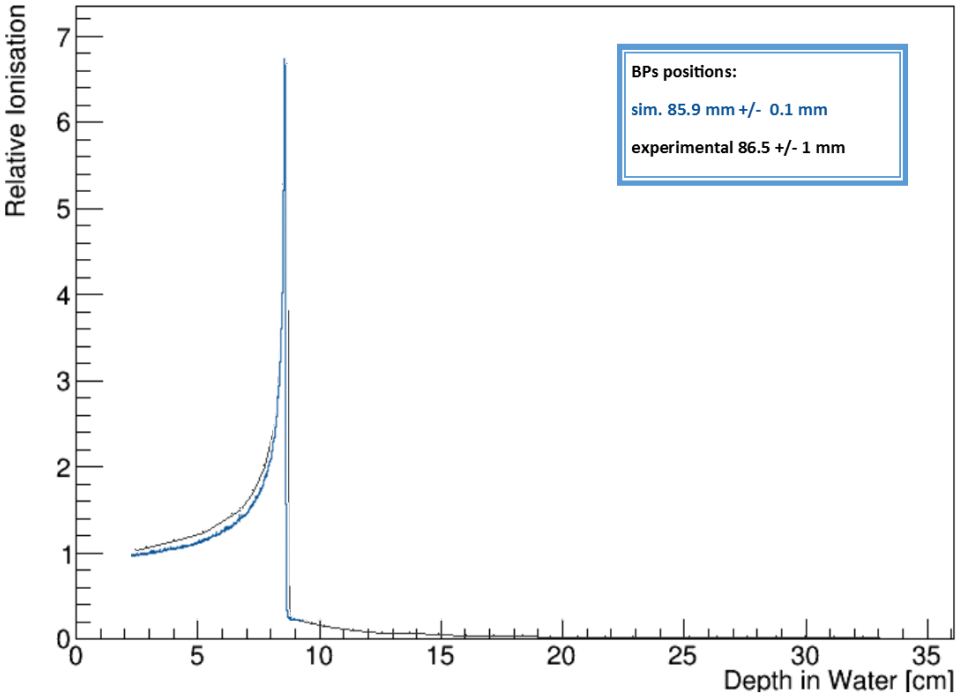

Figure 4.9. Bragg Peak position for 200 MeV/nucleon carbon ions beam in water. Experimental result is plotted in black, simulated one in blue.

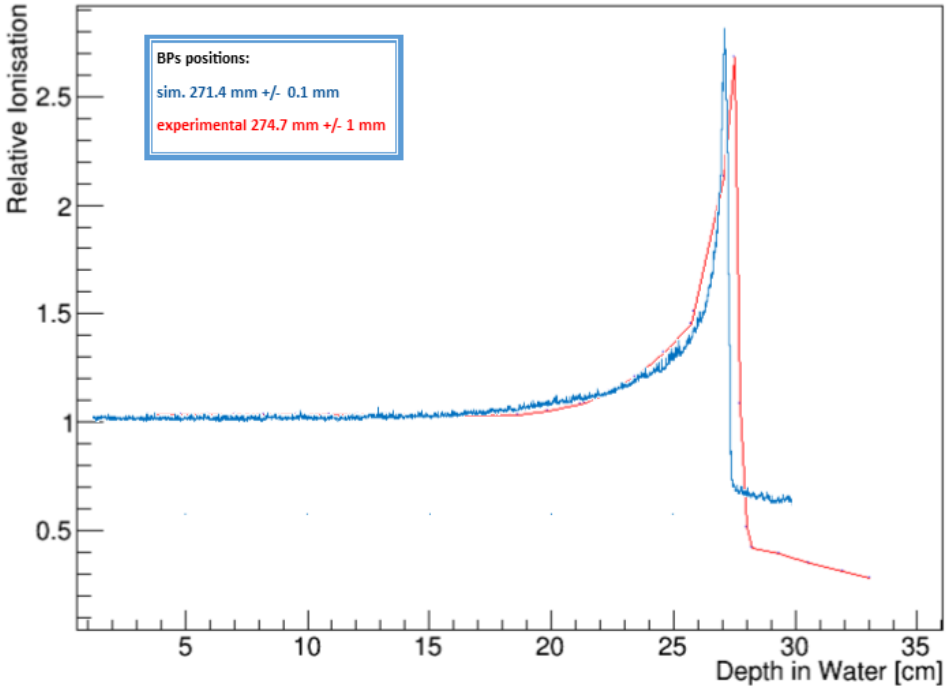

Figure 4.10. Bragg Peak position for 400 MeV/nucleon carbon ions beam in water. Experimental result is plotted in red, simulated one in blue.

In the future a validation of GEANT4 simulated results for fragment yields and energy/angular spectra against experimental data published in Haettner [61] will be carried out. In fact there is urgent need for improvement as none the of available GEANT4 physics model is currently able to accurately reproduce the experimental data neither in terms of number of produced fragment yields nor of their energy/angular distributions [51] [49] [63] with either QMD [52] or INCL [51] claimed to be giving the most reliable data for low-energy carbon ions.

5. ΔE-E telescope characterization with a clinical carbon ion beam at CNAO

5.1. Experiment set-up

This chapter investigates the simulated response of a pixelated silicon ΔE-E telescope detector irradiated by a ^{12}C clinical beam at the CNAO facility, for which the experimental configuration is shown in Figure 5.1. The carbon ions are incident on a PMMA phantom box containing water. The ΔE-E telescope was then placed in the water held by a PMMA box slightly larger than the detector itself and the same configuration was modelled in the GEANT4 simulation. It is important to notice that, at the time of the writing of this thesis, the experimental data were not available, and therefore the simulation results are presented without comparison to experimental measurements. In spite of this, the simulation results offer a solid ground for describing the expected behavior of the detector.

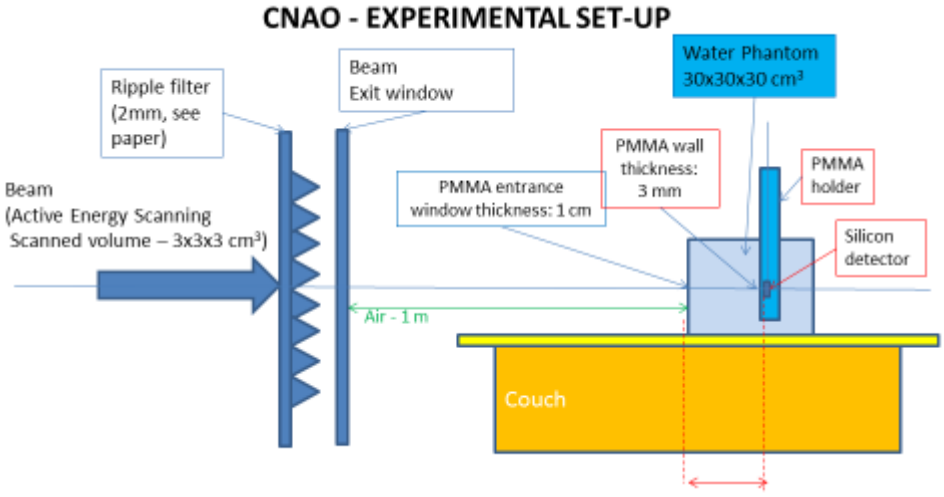

Figure 5.1: CNAO experimental set-up.

5.2. The GEANT4 application

The experimental set-up of the simulation shown in Figure 5.2 consisted of a world volume modelled as a cube of 2 m side, filled with air. Inside the simulated world, the PMMA box, water content, ripple filter and PMMA holder were all simulated to match actual material compositions and dimensions.

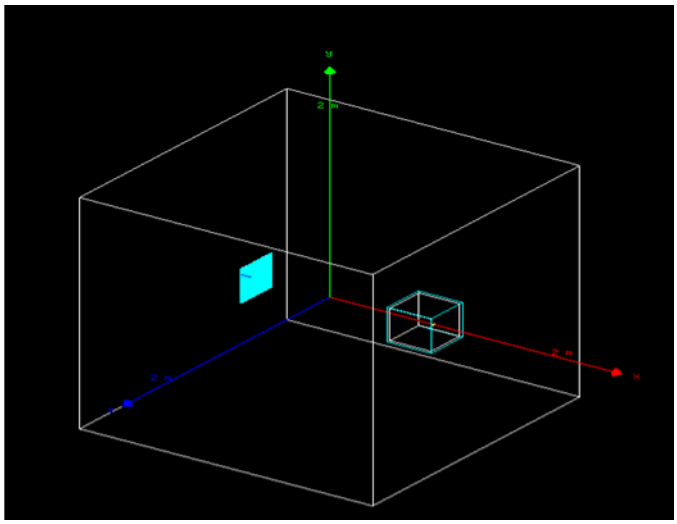

Figure 5.2: Experimental set-up of the Geant4 simulation. The ripple filter is visible on the left (light blue) and the PMMA box with the water target on the right (blue and white frames delimit the boxes).

The radiation field was simulated using a ^{12}C beam generated at 1 m from the phantom surface along the x-axis with initial direction normal to the surface itself. While the x position was kept constant, particles were generated with the y and z coordinates from a squared area of 3 cm per side, corresponding to the real configuration of the CNAO beam line. Primary particles were generated with different kinetic energies depending on a weighting factor listed in Table 5.1 and resulting in the energy spectrum shown in Figure 5.3.

Based on the results shown in Chapter 4 in this study the electromagnetic interactions were modelled using the GEANT4 *Standard Option 3* physics list, whereas the ion hadron interactions were described by means of the *QMD* model. The Binary Cascade model was adopted to model the hadronic inelastic scattering of protons, neutrons and pions. Elastic scattering was modelled as well. The HP data libraries were activated to describe in detail the interaction of neutrons with energies below 20 MeV.

The following cuts were applied: 20 mm to the whole world, 2 mm to the PMMA and water phantoms and 1 μm to a region cladding the detector with a 2 mm thickness on each side of the detector itself. These values were chosen to optimise the computing efficiency of the simulation, without sacrificing the accuracy of the simulation results in the evaluation of the energy deposition in the ΔE-E telescope.

Slice	Energy (MeV/u)	Weight
1	328.1	0.01083107
2	330.2	0.02375417
3	332.2	0.02882543
4	334.1	0.02856271
5	336.1	0.03081029
6	338.1	0.03054569
7	340.1	0.03401608
8	342.1	0.03603699
9	344	0.034382
10	346	0.05978265
11	348	0.03673941
12	349.9	0.04458568
13	351.9	0.04950121
14	353.8	0.05683604
15	355.7	0.06194062
16	357.7	0.08632996
17	359.6	0.08724053
18	361.5	0.25927945

Table 5.1. Primary carbons are generated with different initial kinetic energies; each kinetic energy has a defined weight and corresponds to a different range (corresponding to a “slice” of

the tumor to irradiate). The weight for each slice is provided in the Table. The data are experimental.

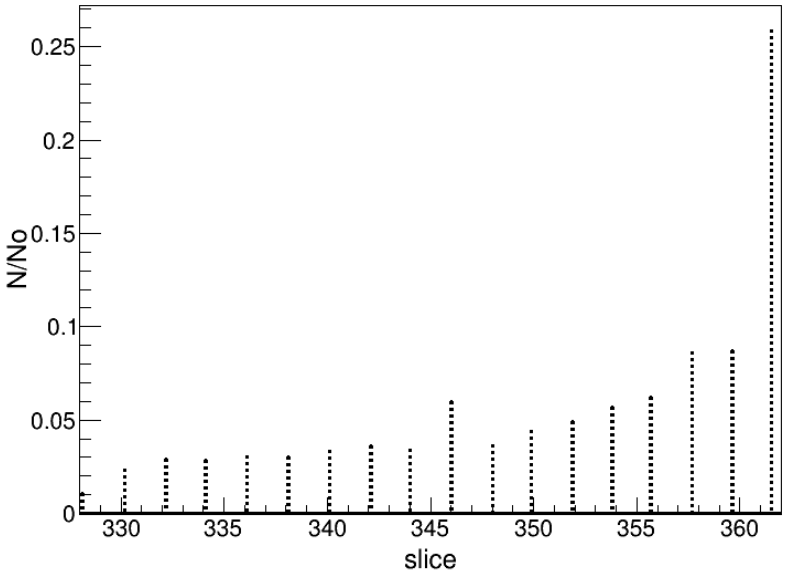

Figure 5.3. Simulated energy spectrum: number of primary particles generated per slice normalized to the total number of generated primaries.

5.3. Characterization of carbon ions radiation field

In a first stage, the ^{12}C radiation field was characterized in terms of fragment yields and their energy deposition in the phantom, a study preliminary to the characterization of the ΔE-E telescope. Figure 5.4 shows the Spread Out of Bragg Peak (SOBP) in the phantom, obtained with incident ^{12}C ions generated as described in the previous section. As expected, the SOBP is characterized by a low entrance physical dose, a larger energy deposition in the SOBP and a characteristic tail entirely due to the contribution of the secondary fragments. In the first and the last centimeter the material is actually PMMA of the box in which the water is contained and that explains the higher energy deposition.

The precision in the energy deposition position is 0.1 mm and the statistical error in the energy deposition itself is less than 1%. A total of $4 \cdot 10^6$ primary particles was used in the simulation to achieve the required statistical uncertainty.

The average number of secondary particles produced by one incident primary as it undergoes nuclear reactions in the water phantom target is summarized in Table 5.2. Protons are the result of nuclear fragmentation and of recoil protons generated in the PMMA and water by elastic reactions between neutrons and hydrogen nuclei. Among others, ^{4}He and neutrons have the largest yields and are mainly due to primary particles undergoing fragmentation. ^{16}O comes mainly by elastic scattering in PMMA or, mainly, water.

^{1}H	^{2}H	^{3}H	^{3}He	^{4}He	^{5}He	^{5}Li
56.549	1.201	0.238	0.215	1.496	0.022	0.019
^{6}Li	^{7}Li	^{7}Be	^{8}Be	^{9}Be	^{9}B	^{10}B
0.093	0.136	0.062	0.023	0.039	0.018	0.154
^{11}B	^{11}C	^{12}C	^{13}C	^{13}N	^{14}N	^{15}N
0.236	0.117	0.564	0.124	0.021	0.196	0.366
^{15}O	^{16}O	^{17}O	Z>8	Neutrons		
0.139	6.594	0.104	0.006	4.543		

Table 5.2: Secondary particle yields produced by one incident ^{12}C. In the table the value of ^{12}C includes only secondary ^{12}C ions generated by heavier nuclei fragmentation processes or elastic scattering in the PMMA phantom. ^{16}O comes mainly by elastic scattering in PMMA or, mainly, water.

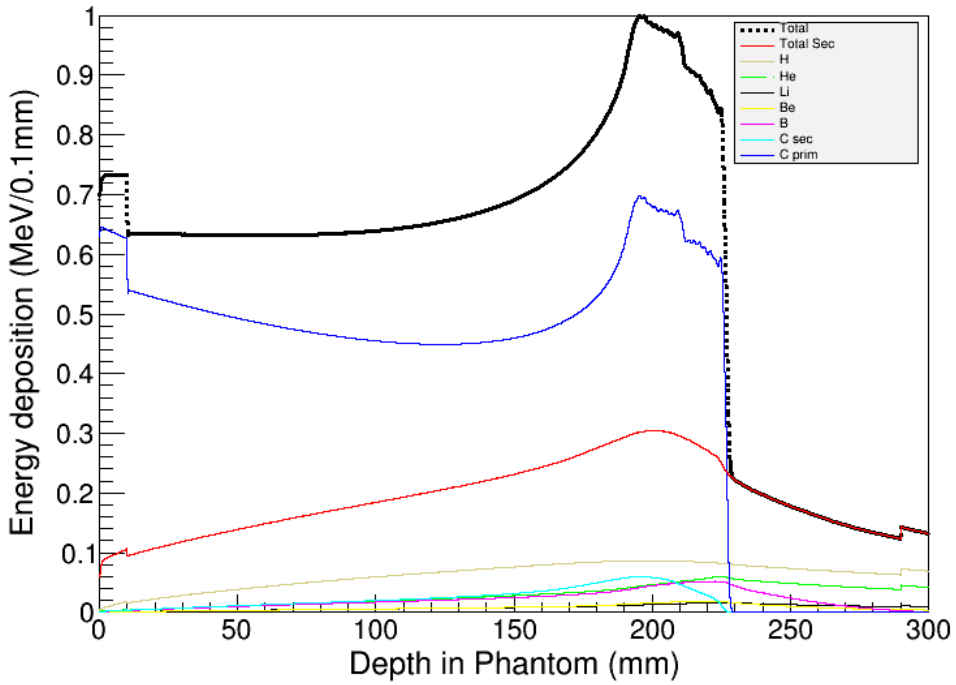

Figure 5.4. SOBP produced by a clinical ^{12}C ion beam and its secondary fragments in a phantom, modelling the patient. The blue line shows the energy deposited by primary ^{12}C whereas the red line shows the total contribution of the secondary particles. Note that the origin is placed at the front of the 10 mm thick PMMA phantom surrounding the water target, which explains the higher energy deposition. The energy deposition in MeV is normalized to the total number of primary particles. The bin of the x axis is 0.1 mm.

The distribution of the point of origin of secondary nuclear recoils generated in the water phantom is projected in the 2D plots in Figure 5.5 and the in all figures to Figure 5.12. The beam is incident on the phantom from the bottom of the figures. The spatial resolution is 1 mm^2 and the scale is normalized to the number of incident primary carbon ions. The region with the greater production of secondary particles is inside the primary beam path up to the SOBP but particularly for protons and oxygen ions the generating region is mostly scattered all over the water target. The reasons for finding oxygen ions generating away from the primary beam field is mainly attributable to neutron scattering.

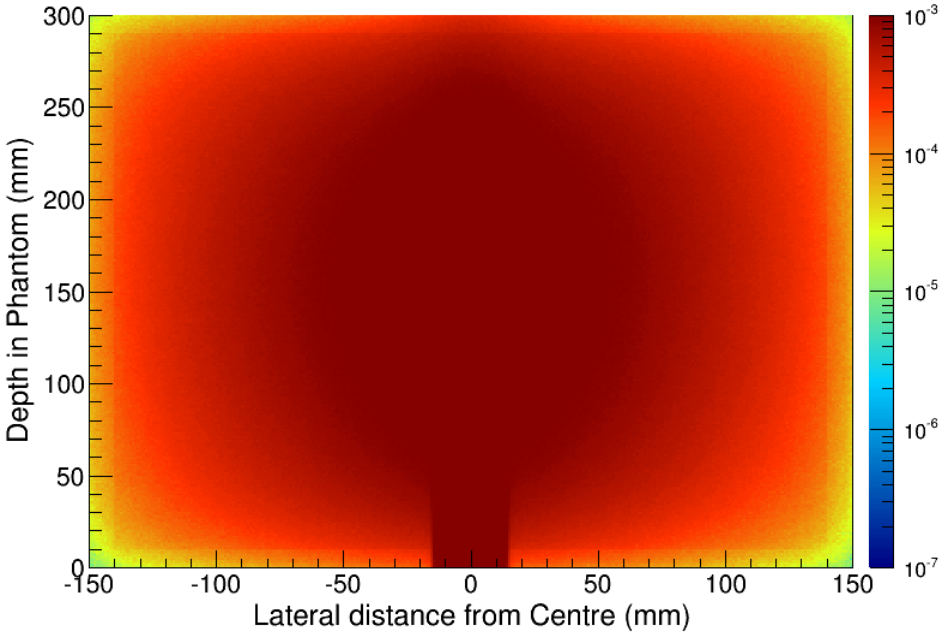

Figure 5.5. 2D distribution of the point of origin of secondary ^{1}H normalized to the number of incident primary carbon ions.

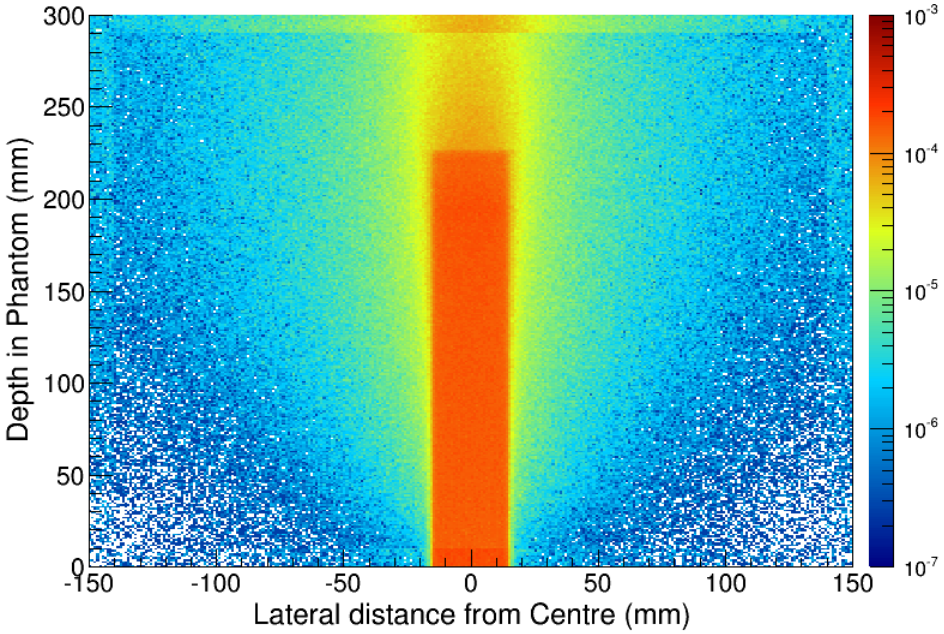

Figure 5.6. 2D distribution of the point of origin of secondary ^{4}He normalized to the number of incident primary carbon ions.

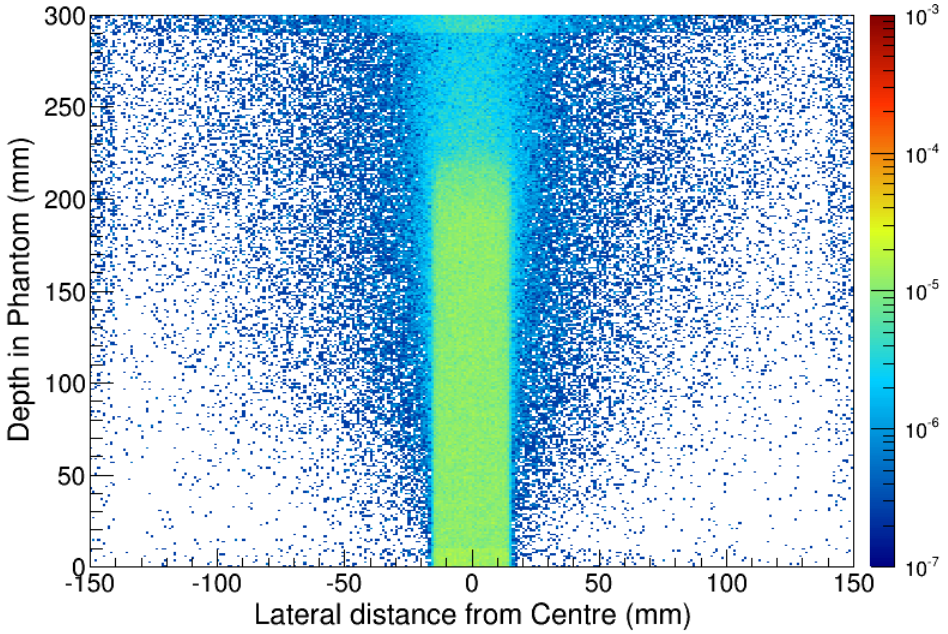

Figure 5.7. 2D distribution of the point of origin of secondary ^{6}Li normalized to the number of incident primary carbon ions.

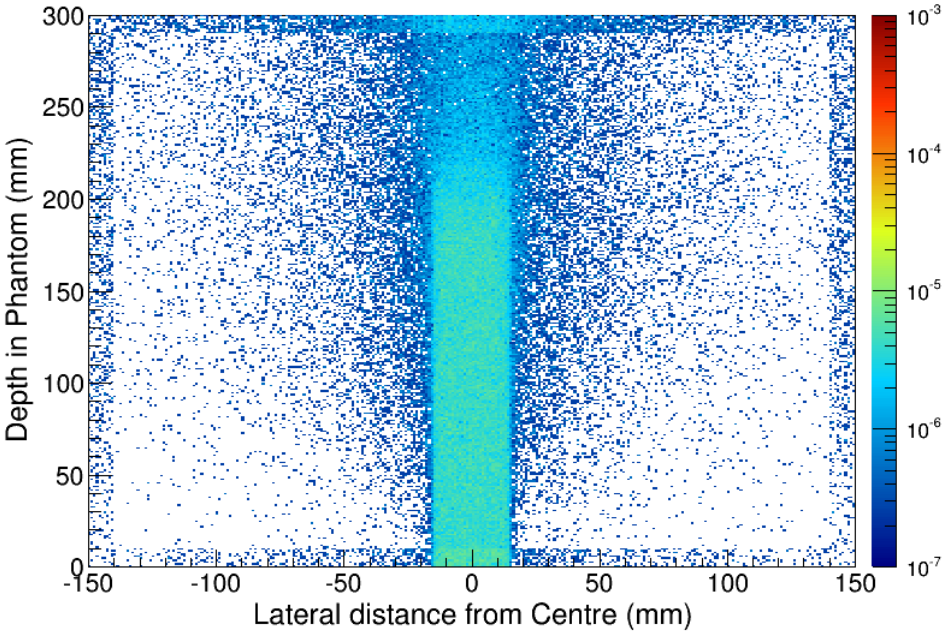

Figure 5.8. 2D distribution of the point of origin of secondary ^{9}Be normalized to the number of incident primary carbon ions.

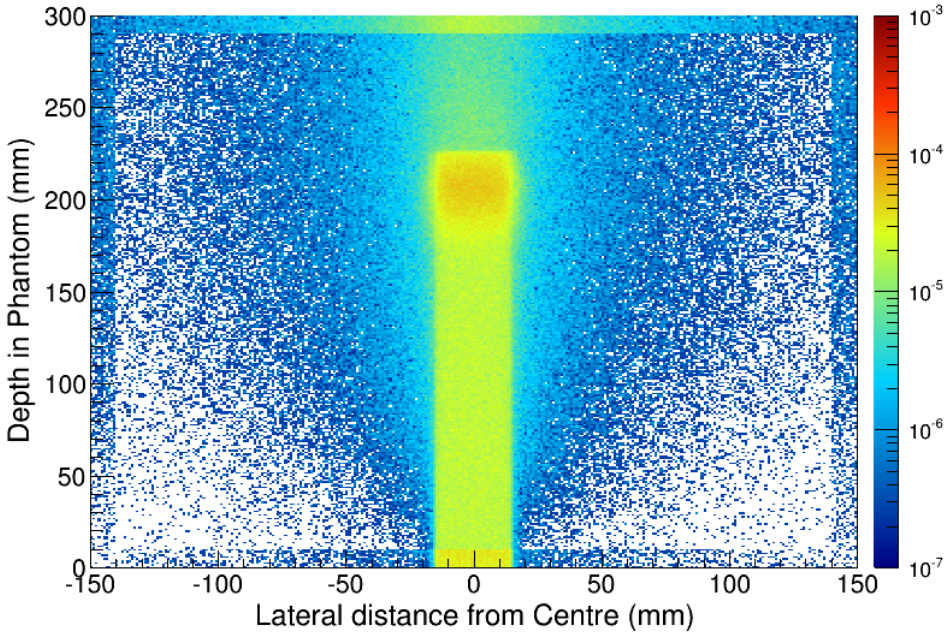

Figure 5.9. 2D distribution of the point of origin of secondary ^{11}B normalized to the number of incident primary carbon ions.

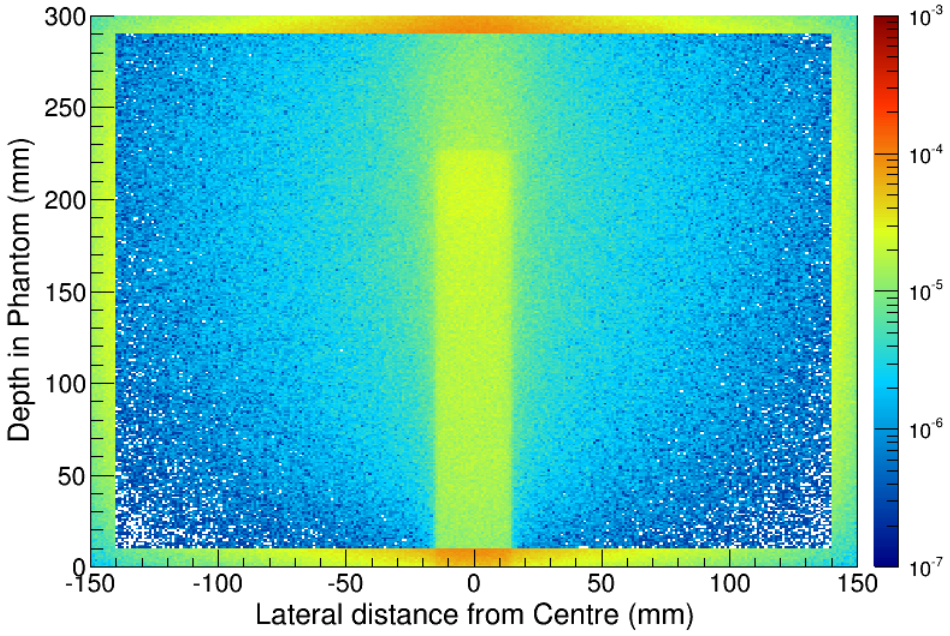

Figure 5.10. 2D distribution of the point of origin of secondary ^{12}C normalized to the number of incident primary carbon ions.

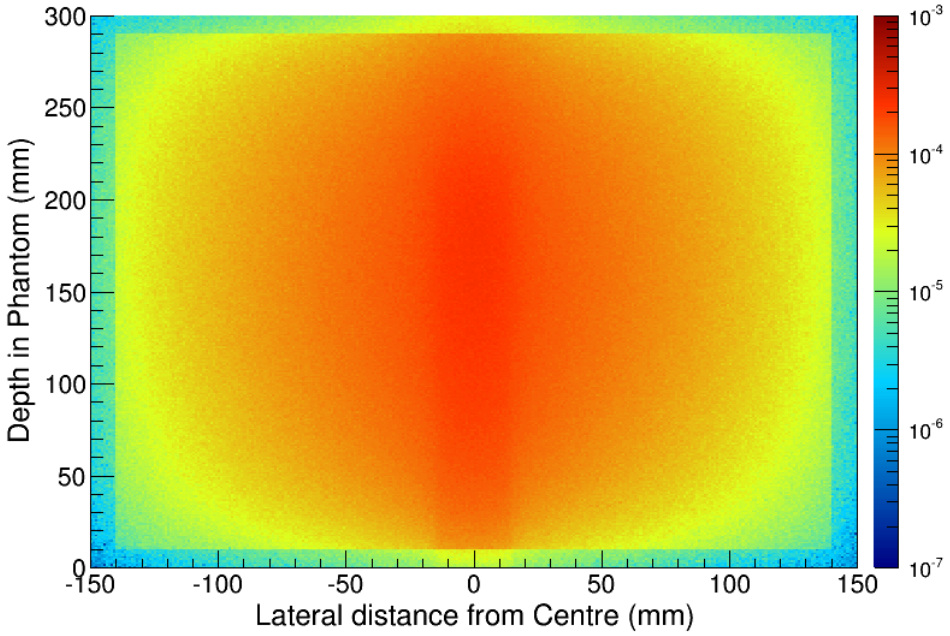

Figure 5.11. 2D distribution of the point of origin of secondary ^{16}O normalized to the number of incident primary carbon ions.

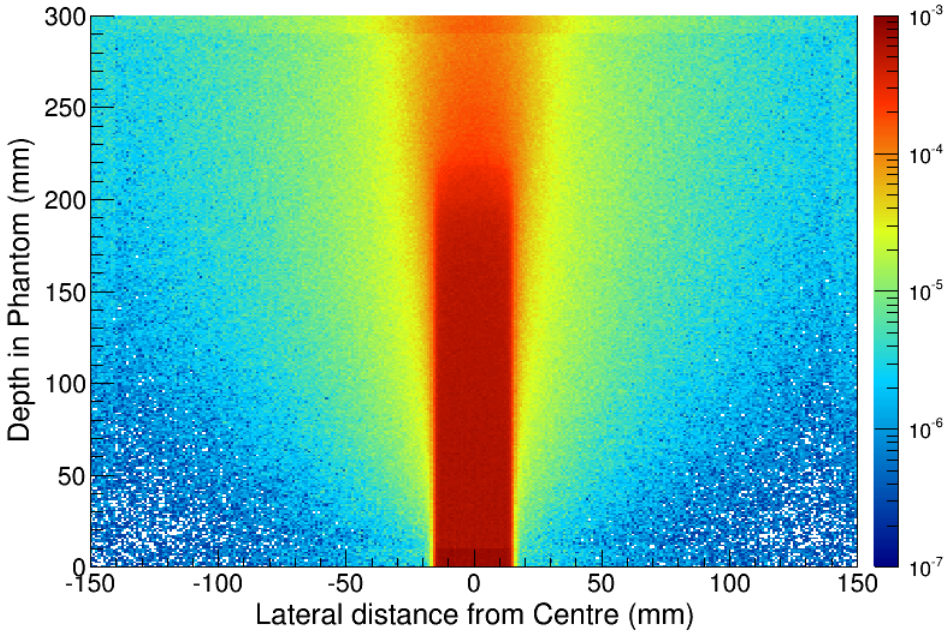

Figure 5.12. 2D distribution of the point of origin of secondary neutrons normalized to the number of incident primary carbon ions.

The superior energy deposition conformality of a carbon ion beam with respect to other radiotherapy techniques (e.g. x-ray and proton therapy) becomes evident by observing the plots from Figure 5.13 through Figure 5.21. The 2D energy deposition distribution of the secondary particles is plotted with a precision of 1 mm^2 and the scale is normalized to the number of incident carbon ions. Plots are given as a top-view of the PMMA box and its water content.

Lighter nuclei have a greater distribution of energies experiencing a greater scattering in the phantom with respect to heavier nuclei. Since they are more easily scattered they are also more likely to deposit their energy away from the primary beam, in the out of field region, as can be depicted from Figure 5.13 and Figure 5.14. The opposite is true for heavier fragments, as shown in Figure 5.17 and Figure 5.20. In fact, the energy deposition out-of-field is larger for protons and helium ions so the detector response is expected to be dominated by these contributors when placed away from the beam axis. It can also be observed that the energy deposition of the secondary particles is maximized in the SOBP region.

Finally, neutrons are most likely to undergo multiple elastic collisions with nuclei in the phantom thus depositing their energy away from the primary beam but since they are uncharged particles they are not detected directly and the charged particles resulting from their interactions with a target material are detected instead.

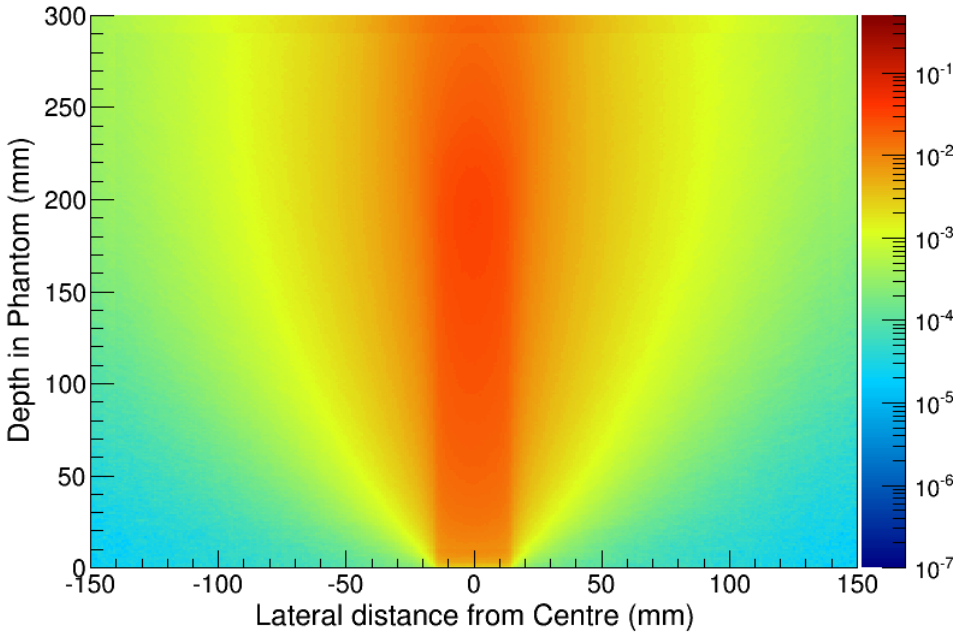

Figure 5.13. 2D energy deposition in the target due to H.

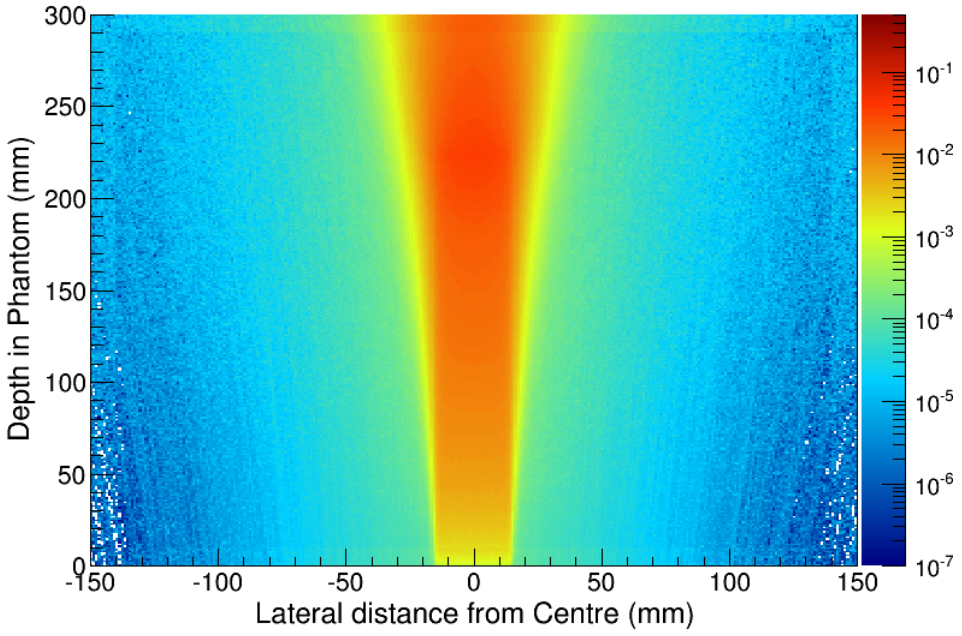

Figure 5.14. 2D energy deposition in the target due to He.

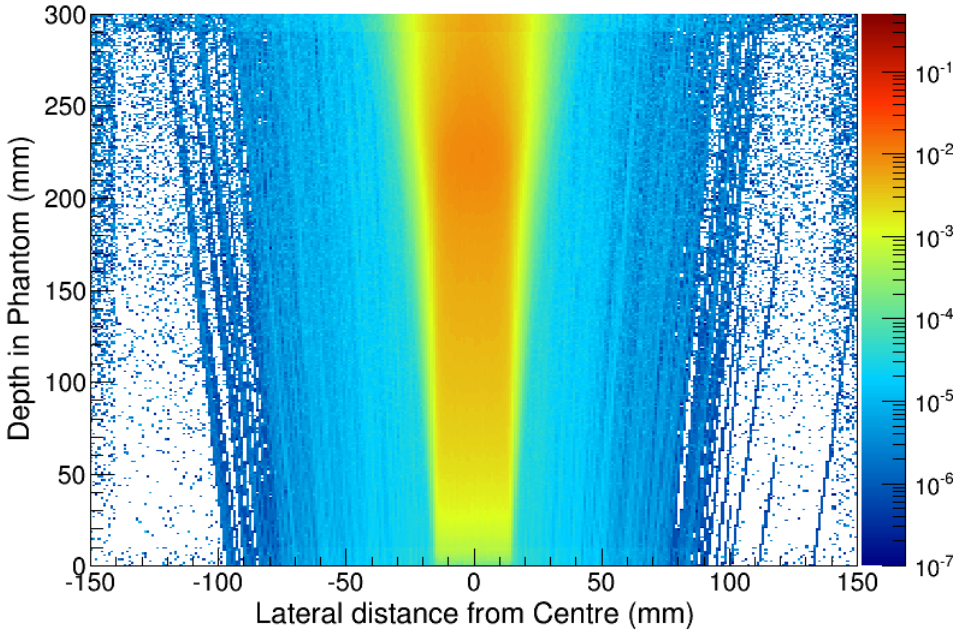

Figure 5.15. 2D energy deposition in the target due to Li.

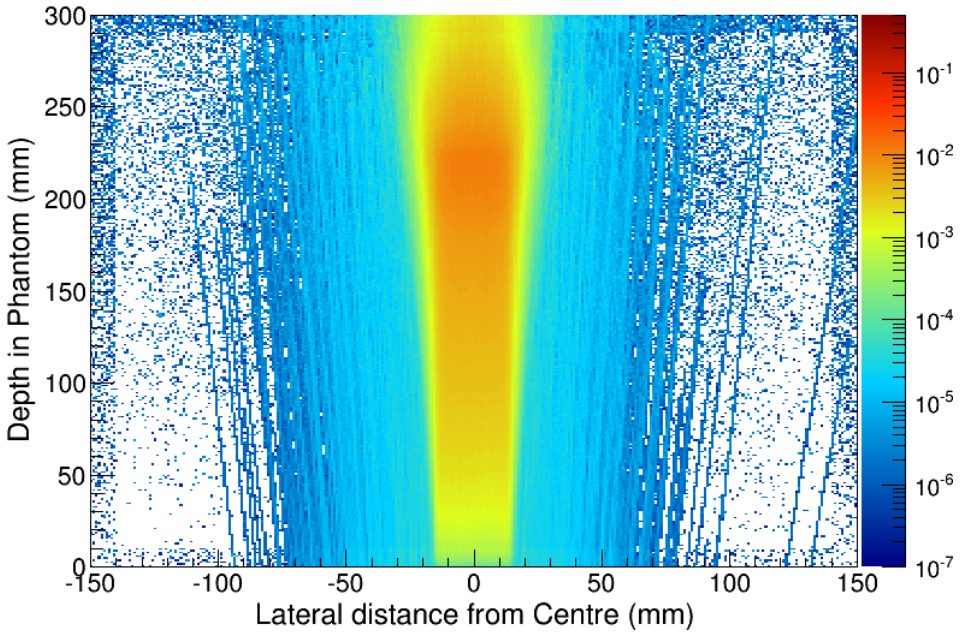

Figure 5.16. 2D energy deposition in the target due to Be.

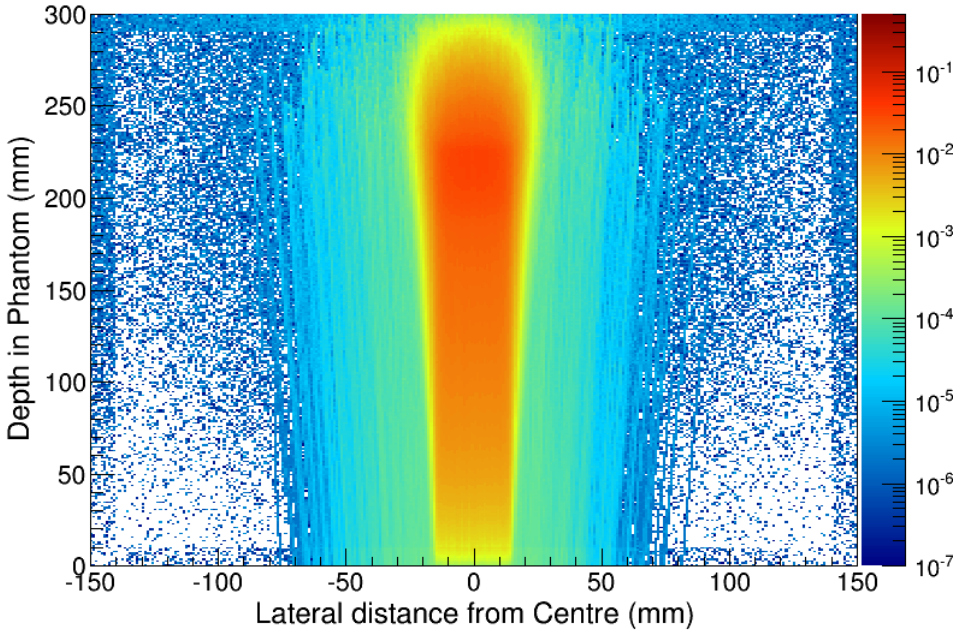

Figure 5.17. 2D energy deposition in the target due to B.

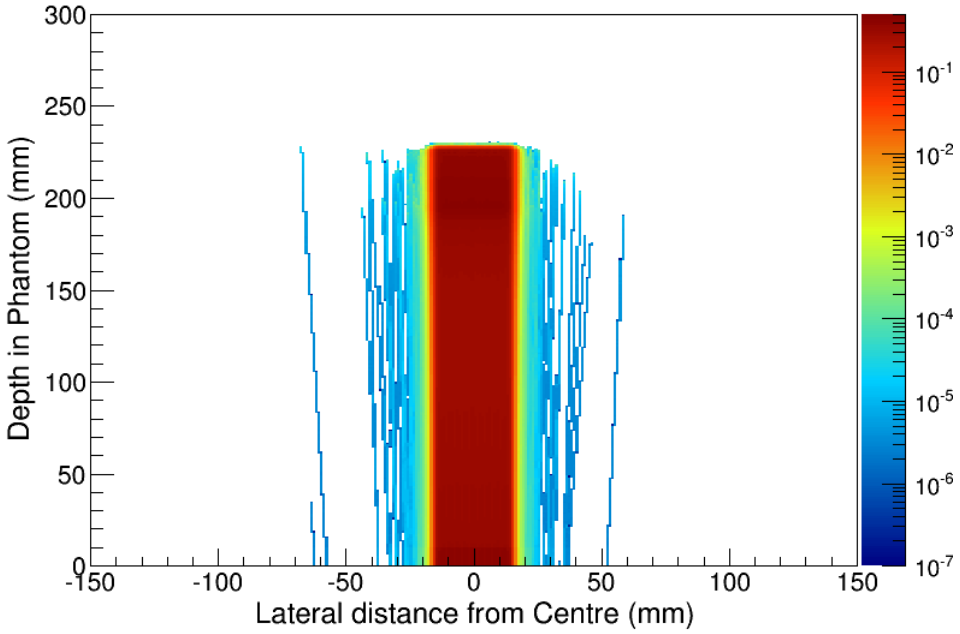

Figure 5.18. 2D energy deposition in the target due to C (primaries).

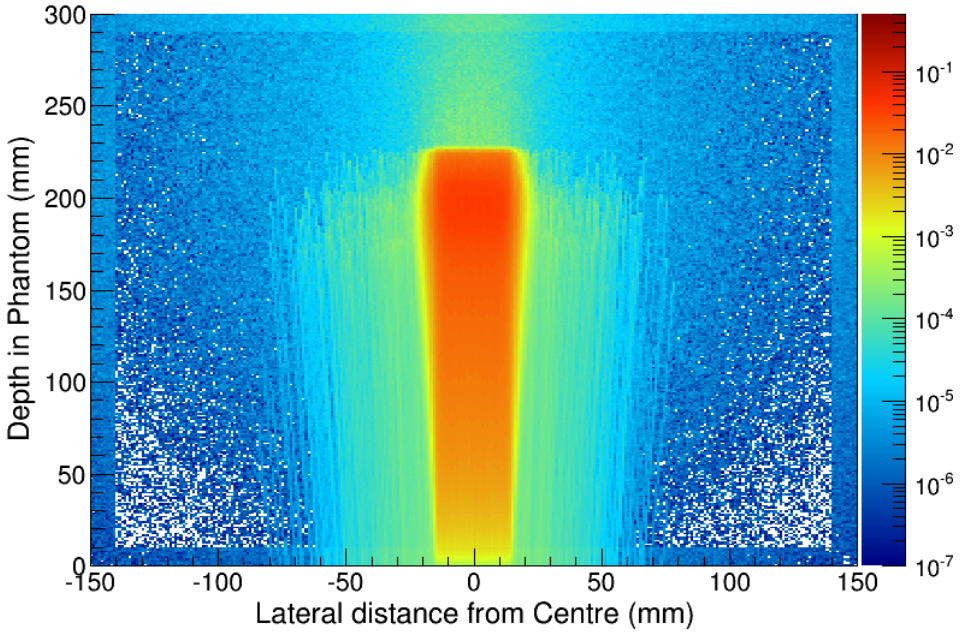

Figure 5.19. 2D energy deposition in the target due to C (secondaries).

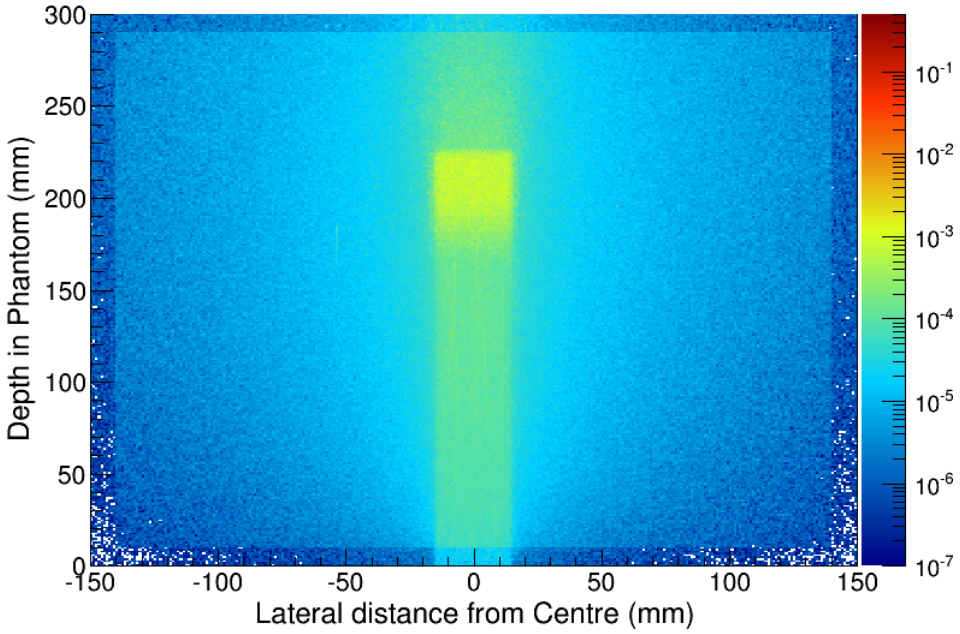

Figure 5.20. 2D energy deposition in the target due to O.

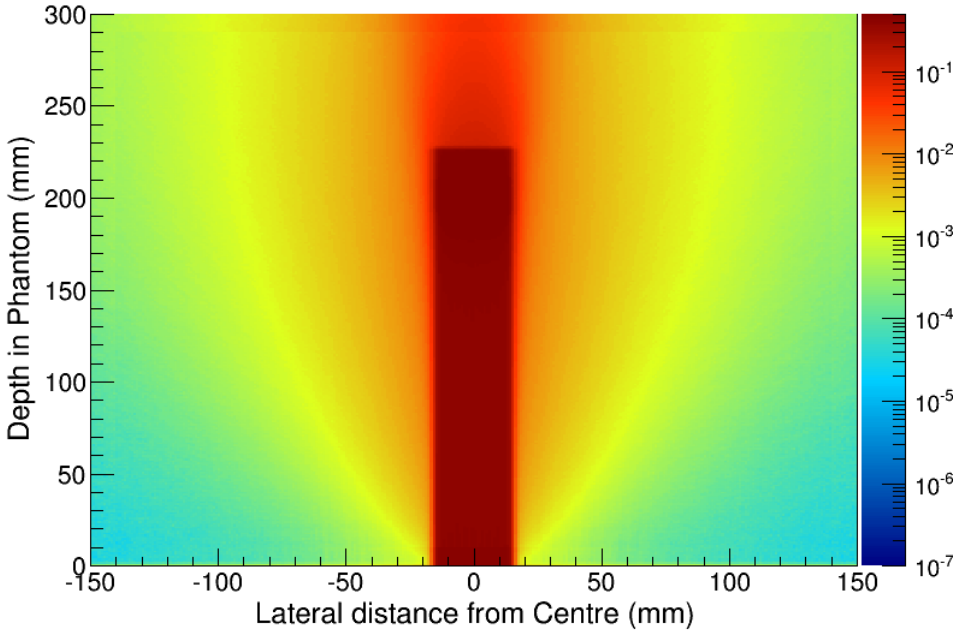

Figure 5.21. Total 2D energy deposition in the target due to primary particles and secondary particles.

5.4. Characterization of the ΔE-E telescope response

The response of the detector is shown in 2D plots with the energy deposited in the ΔE stage on the vertical axis and the energy deposited in both the ΔE stage and E stage on the horizontal axis.

For the purpose of the characterization of the telescope response, the detector was simulated as operated in coincidence, hence only particles depositing their energy in both the ΔE and the E stages were counted, as the real device actually operates.

Using SRIM [32], it was found that the minimal energy required for an incident ^{12}C to have coincidence events in both the telescope stages is 1250 keV. This is the energy required to traverse the ΔE stage (whose thickness is 1.8 μm) and reach the E stage. Table 5.3 lists the energy thresholds for detecting different types of nuclear fragments.

Particle	Energy threshold (keV)
^{1}H	200
^{4}He	440
^{6}Li	530
^{8}Be	680
^{10}B	1040
^{12}C	1250
^{14}N	1410
^{16}O	1410

Table 5.3: Minimum kinetic energy of different fragments to produce coincidence events in the ΔE-E telescope.

By applying the relationship below [32]

$$\frac{R_{Z_1A_1}}{R_{Z_2A_2}} = \frac{Z_2^2 A_1}{Z_1^2 A_2}$$

which holds for two non relativistic heavy charged particles with the same velocity and of range respectively $R_{Z_1A_1}$ and $R_{Z_2A_2}$ and whose atomic numbers are Z_1 and Z_2 and mass numbers A_1 and A_2. If one of the two considered particles is a proton then the relationship can be re-written as [32]

$$R_P = \frac{Z^2}{A} R_{ZA}$$

with R_P being the range of the proton and the other parameters corresponding to the second considered particle. Both the relations stated above hold in a non-relativistic case and can therefore be safely applied in this study [32].

From the NIST database [69] it is known that a proton with kinetic energy 8 MeV has a range of 500 μm in silicon, comparable to the thickness of the ΔE-E telescope detector, and based on the considerations above the kinetic

energies of nuclear recoils to stop completely in the detector are provided in Table 5.4. The maximum energy deposition for all particles occurs when they have a range in silicon matching the detector thickness.

Particle	Energy (MeV)
^{1}H	8
^{4}He	32
^{6}Li	62
^{8}Be	99
^{10}B	138
^{12}C	185

Table 5.4: Kinetic energy of different types of particle to completely stop in the detector. Values have been extrapolated from the proton range in silicon accessed from NIST database, in the non-relativistic hypothesis [32].

5.4.1. In-field configuration

The detector response was first characterized by placing the device on the main axis of the incident beam, at various depths in the phantom before, at and after the SOBP, in a so-called in-field configuration as explained in Chapter 3. Positions are listed in Table 5.5.

Depth in phantom[10] (mm)	Region	Primary particles generated
50	Plateau	$82*10^6$
150	Plateau	$62*10^6$
170	Plateau	$240*10^6$
190	SOBP	$62*10^6$
195	SOBP	$80*10^6$
210	SOBP	$240*10^6$
220	SOBP	$240*10^6$
225	SOBP	$240*10^6$
230	Distal edge	$240*10^6$
250	Tail	$240*10^6$

Table 5.5: Positions where the ΔE-E telescope was placed along the SOBP, in the in-field configuration. The column on the right indicates the number of events generated in each simulation to obtain statistically meaningful results.

The number of primary particles or events generated in each simulation, for each depth, is indicated in Table 5.5 as well. At greater depths a larger number of events is simulated to obtain statistically meaningful results, as the straggling causes a lower fraction of incident particles reaching the detector thus lowering the statistics.

For the positions indicated in Table 5.5, the response of the detector is shown in Figure 5.22 and then in all figures to Figure 5.31 using ΔE-E plots

10 Depths comprise the 1 cm PMMA phantom thickness.

with the total energy deposition in the telescope shown in the x-axis and the energy deposition in the ΔE stage only in the y-axis. As a reminder, energy depositions events in the two stages are acquired in coincidence as in the real detector. The frequency of the energy deposition events is normalized with respect to the number of the events generated in the simulation.

The ΔE-E plot in Figure 5.22 is characterized by a clustered energy deposition in the detector between 10 and 15 MeV due to primary carbon ions. The amount of H and He nuclei is negligible and mainly due to few fragmentation processes occurring in the PMMA and in the air medium at the entrance of the phantom. At greater depths in the phantom the clustered energy deposition of incident carbon ions moves to the right of the ΔE-E plot as the LET becomes higher with lower kinetic energies. At the same time the primary particles are subject to more fragmentation events, therefore loci corresponding to different particle types become visible. This can be clearly observed in Figure 5.24 for light fragments whereas in Figure 5.27 and Figure 5.28 the loci corresponding to fragments heavier than H and He are also visible.

The maximum energy deposition in the detector as a whole due to primary carbon ions is somewhere around 180 MeV, corresponding to the kink in the plot seen in Figure 5.25 and then all figures to Figure 5.28. This value is consistent with the expected one for ^{12}C as listed in Table 5.4. It can also be noted that at this depth carbon ions crossing the detector outnumber those stopping in the detector.

In Figure 5.29, Figure 5.30 and Figure 5.31 it can be seen that almost all primary carbon ions have come to a complete stop, with loci of secondary fragments still distinguishable in the plots. Heavier fragments such as oxygen but mostly fluorine and neon are also present. Fragments' kinks can be compared to the corresponding expected kinetic energies of the fragments, required to have the range equal to the thickness of the device, as listed in Table 5.4. The statistics in the tail region of the SOBP is much lower than for previous regions due straggling increasing with the depth in

the phantom resulting in less secondary particles overall. In this region secondary fragments are the most abundant contributors to the energy deposition.

These results show that the ΔE-E telescope is a suitable candidate for QA for HIT. In fact, once the position of the kink of each locus has been measured, it is possible to retrieve the kinetic energy of the incident carbon ion or fragment. The device can therefore be used to characterize the ^{12}C radiation field in terms of fragments, which is particularly important in the distal edge of the SOBP and out of field. Finally the detector has a sub-mm spatial resolution, which is crucial in the distal edge of the SOBP where the energy deposition and radiation field change dramatically over a short distance.

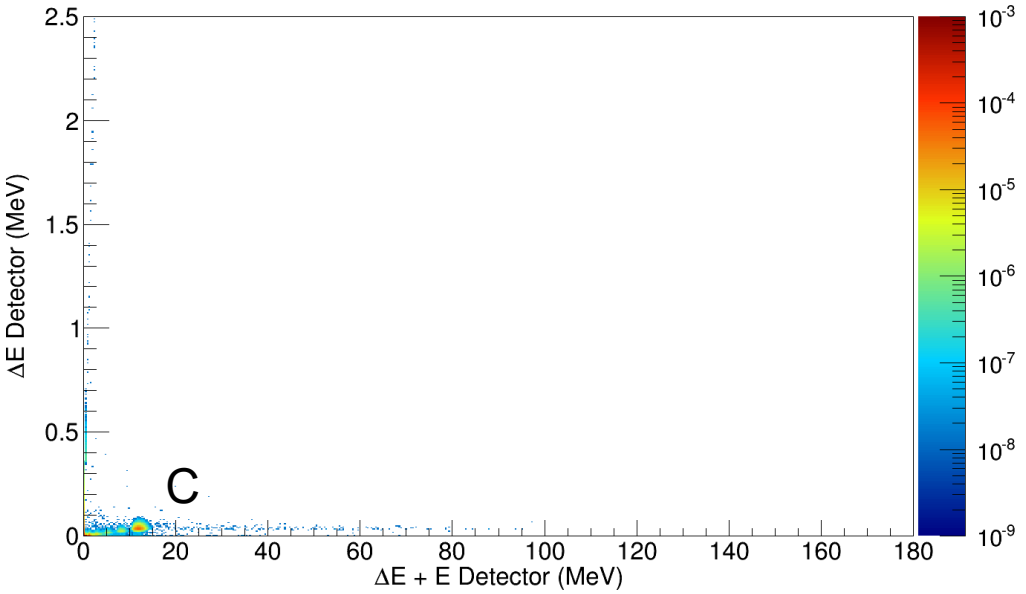

Figure 5.22. ΔE-E plot for telescope placed in-field at 50 mm in the phantom. There is a clustered energy deposition in the detector between 10 and 15 MeV due to primary carbon ions. The amount of H and He nuclei is negligible.

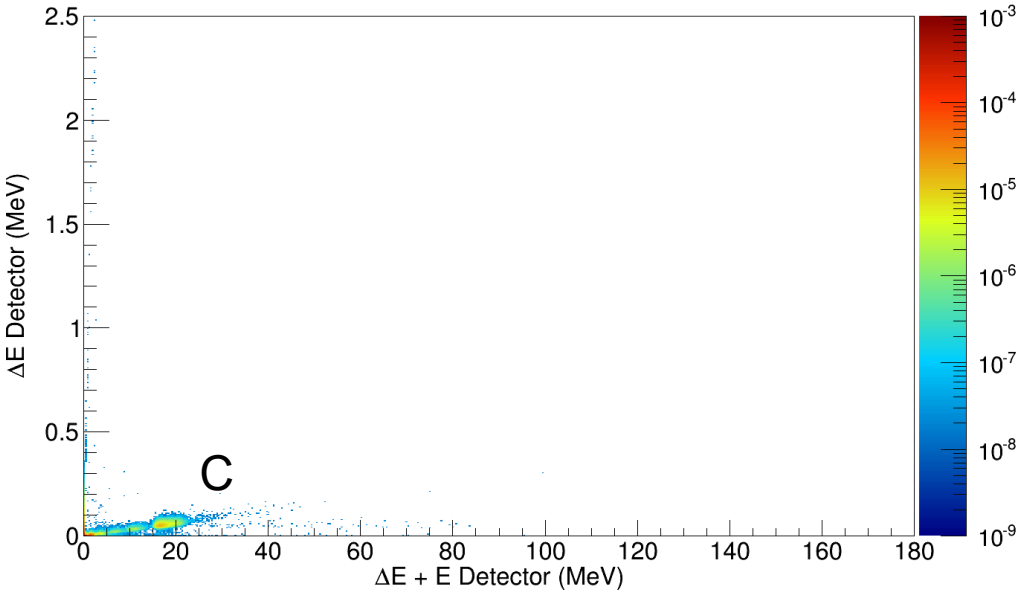

Figure 5.23. ΔE-E plot for telescope placed in-field at 150 mm in the phantom.

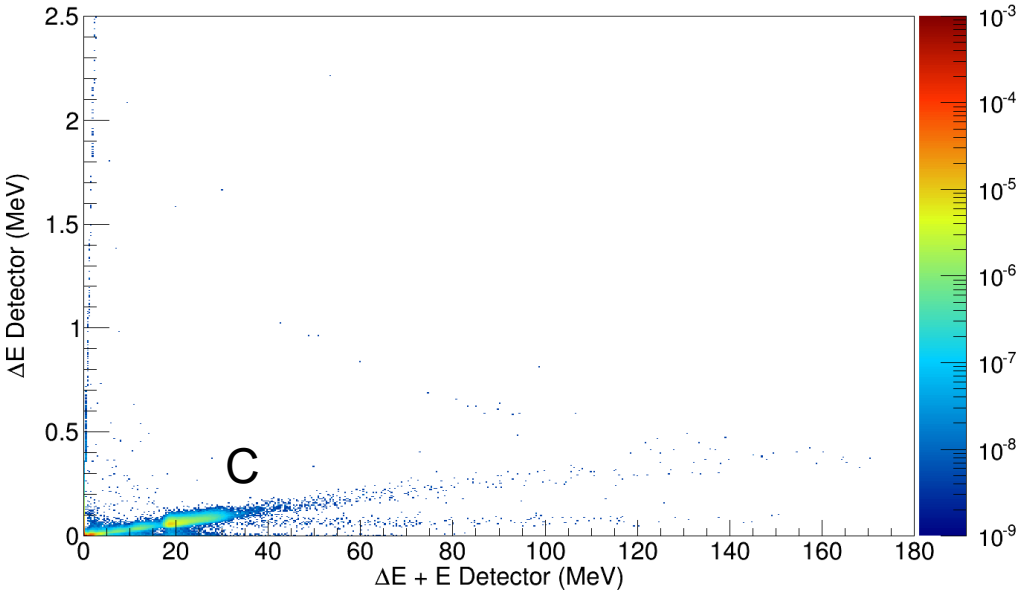

Figure 5.24. ΔE-E plot for telescope placed in-field at 170 mm in the phantom.

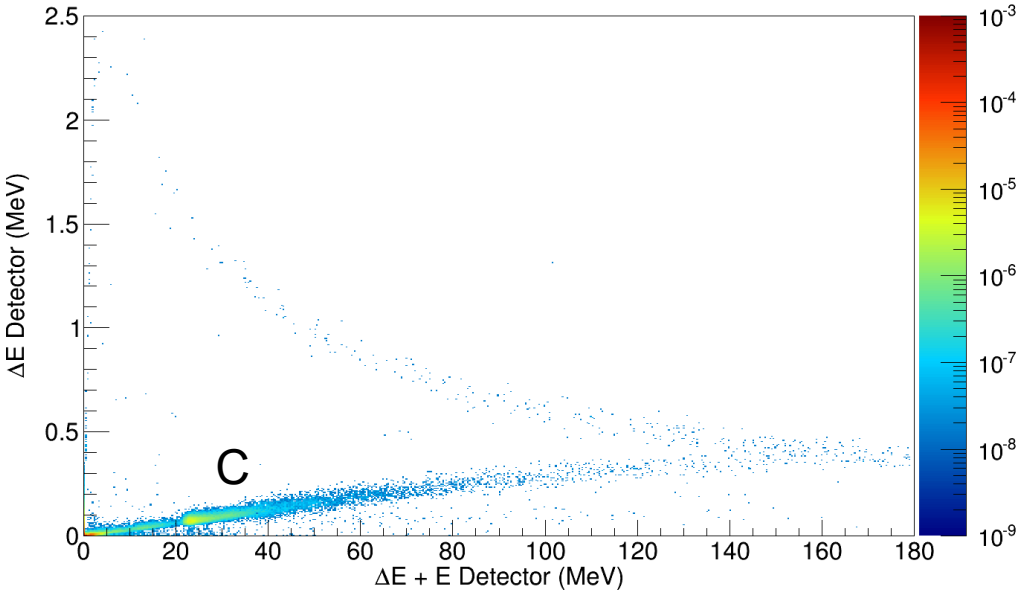

Figure 5.25. ΔE-E plot for telescope placed in-field at 190 mm in the phantom. The maximum energy deposition in the detector as a whole due to primary carbon ions is somewhere around 180 MeV, corresponding to the kink in the plot.

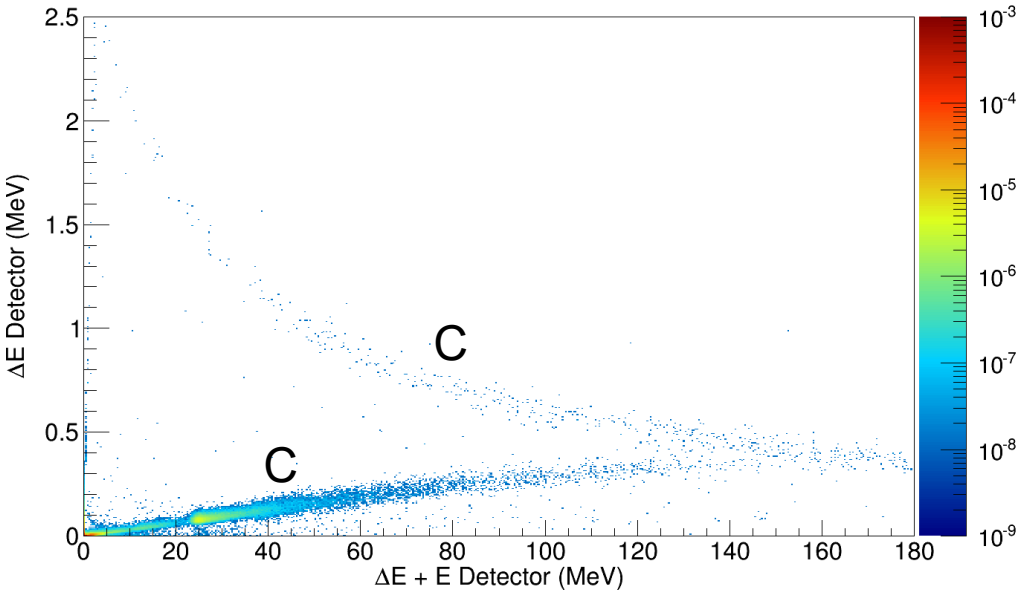

Figure 5.26. ΔE-E plot for telescope placed in-field at 195 mm in the phantom.

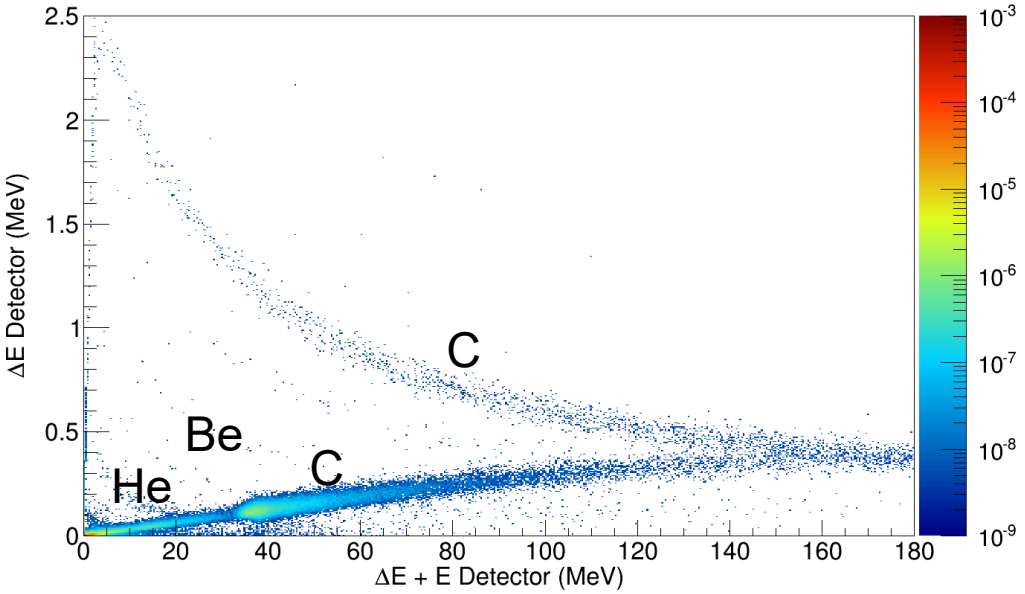

Figure 5.27. ΔE-E plot for telescope placed in-field at 210 mm in the phantom. The maximum energy deposition in the detector as a whole due to primary carbon ions is somewhere around 180 MeV, corresponding to the kink in the plot. Loci of secondary fragments are visible.

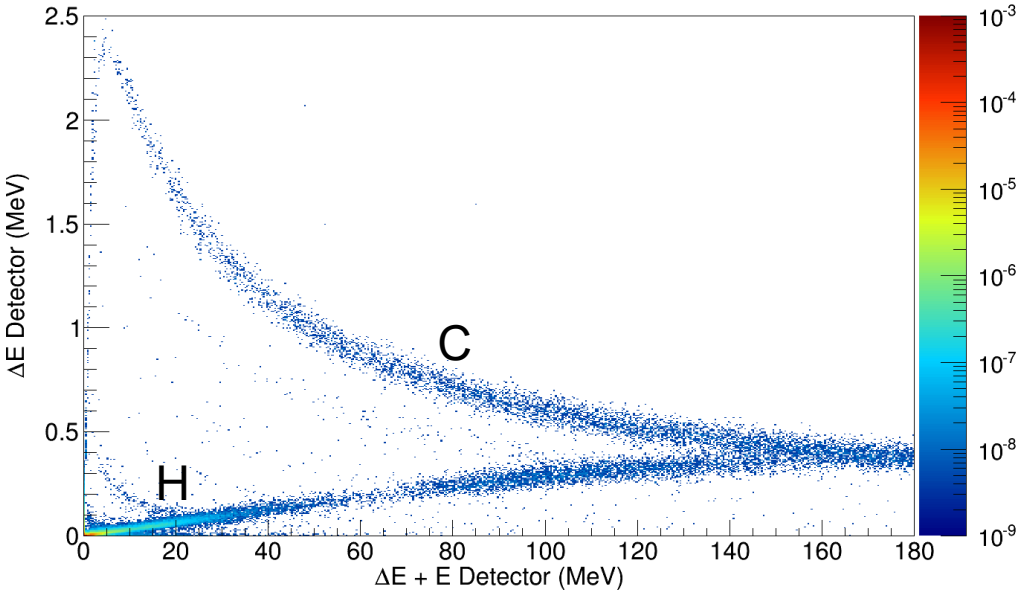

Figure 5.28. ΔE-E plot for telescope placed in-field at 220 mm in the phantom.

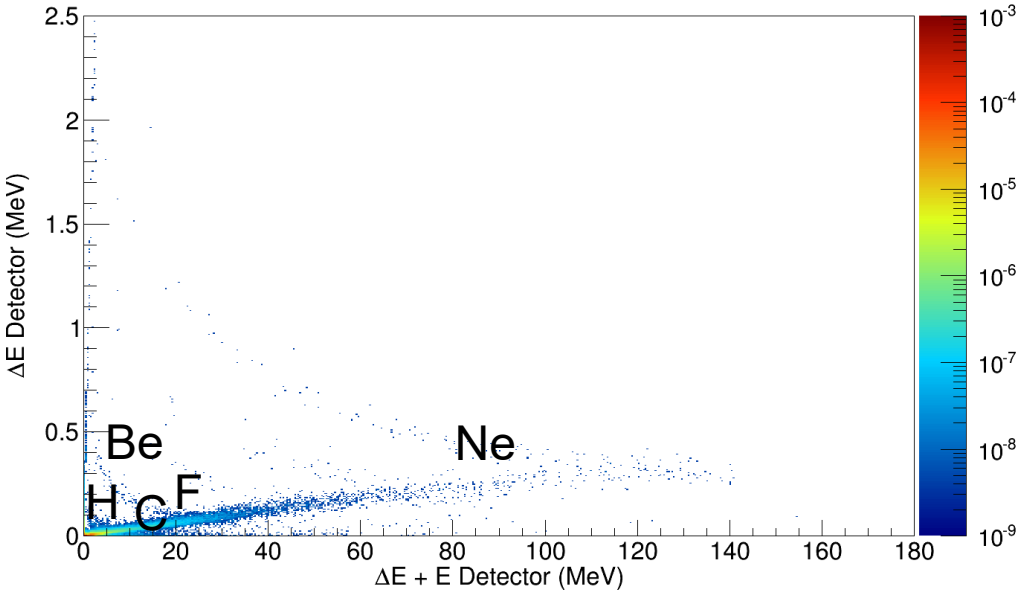

Figure 5.29. ΔE-E plot for telescope placed in-field at 225 mm in the phantom. Primary carbon ions still deposit energy in the detector but in far smaller quantity. Heavier fragments such as Ne, F and O are present.

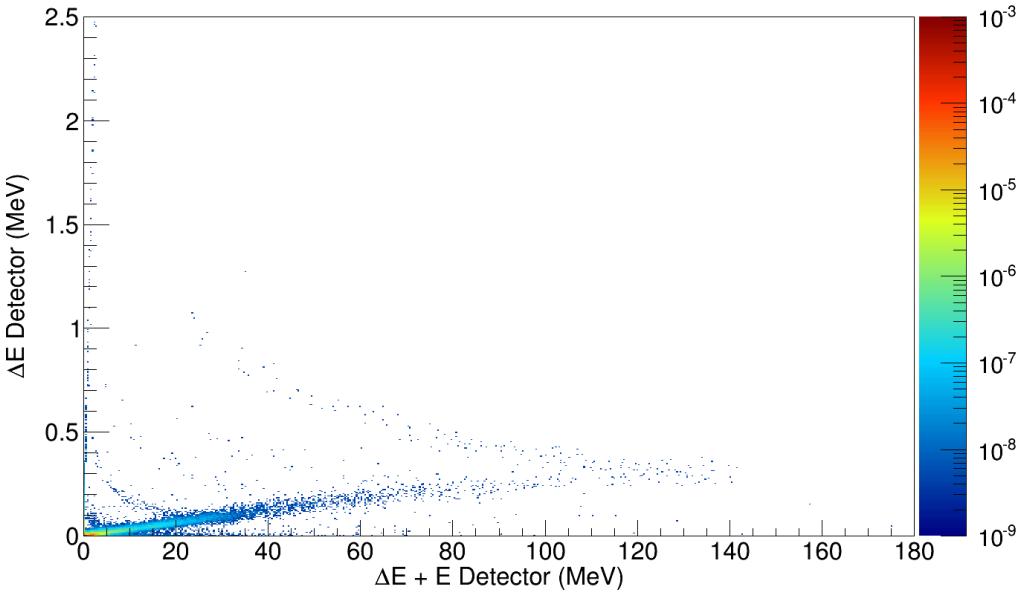

Figure 5.30. ΔE-E plot for telescope placed in-field at 230 mm in the phantom. Primary carbon ions deposit a limited amount of energy in the detector. Main contributors to the energy deposition are secondary fragments such as Ne, F and lighter fragments.

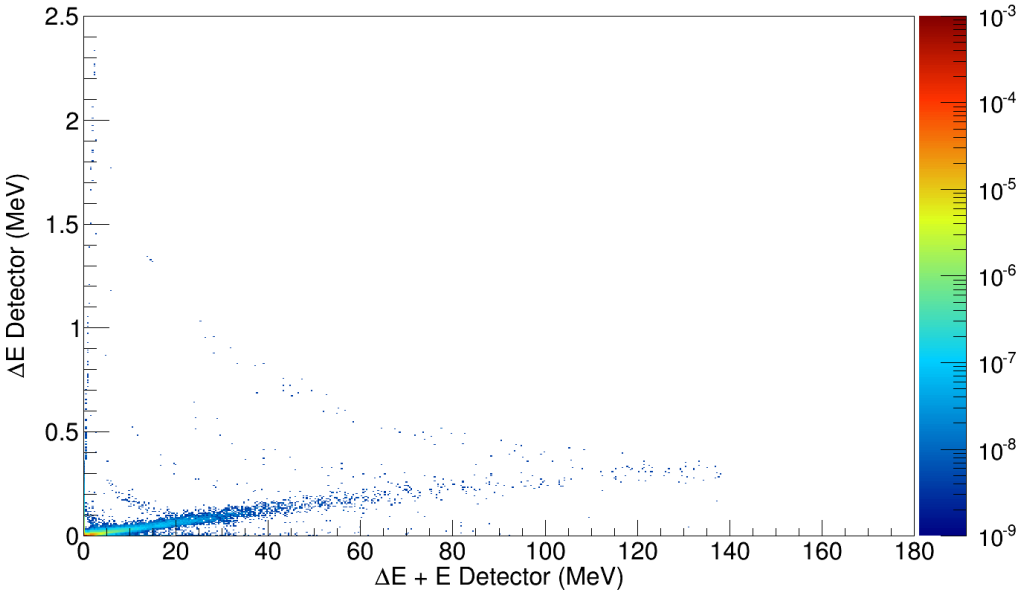

Figure 5.31. ΔE-E plot for telescope placed in-field at 250 mm in the phantom.

Microdosimetric spectra with area normalized to 1 were acquired for the same positions indicated in Table 5.5 using the ΔE stage of the telescope detector and are shown in Figure 5.32 and then in all figures to Figure 5.40. Separated dose weighted components have been shown in each microdosimetric spectrum.

It can be observed that in the plateau region, as for instance in Figure 5.32, the main contributions to the spectra derive from the primary carbons. Their lineal energies gradually increase towards the SOBP, as can be depicted by comparing Figure 5.32 to Figure 5.36. Figure 5.37 corresponds to a depth of 220 mm in the phantom and ^{12}C stoppers can be seen at this depth. In the microdosimetric spectrum a second minor peak other than the main peak due to carbon ions was observed which corresponds to those ^{12}C ions stopping in the detector (carbon edge). In the distal part of the SOBP and beyond, Figure 5.38 to Figure 5.40, even though a fair amount of primary carbon ions are still depositing energy in the detector, the fragments only contribute to the microdosimetric spectra as they are the dominant component of the radiation field.

The microdosimetric spectra have been converted from silicon to tissue using an appropriate factor [24] and the MKM model (described in Chapter 1), has been used to determine the RBE_{10} profile shown in Figure 5.41. It has been shown that the RBE_{10} profiles obtained with this method relate well with respect to RBE_{10} profiles obtained with microdosimetric spectra measured with a TEPC [37].

In Figure 5.41 it can be noted that the RBE_{10} is approximately flat in the plateau region, it increases towards the distal part of the SOBP reaching a maximum value of 2.2 and then fall off sharply to values around 1 in the tail. The obtained profile relate well with respect to RBE_{10} profiles obtained with microdosimetric spectra acquired with a TEPC at HIMAC with a 60 mm SOBP in water obtained using a ridge filter with a 290 MeV per nucleon ^{12}C beam line [11].

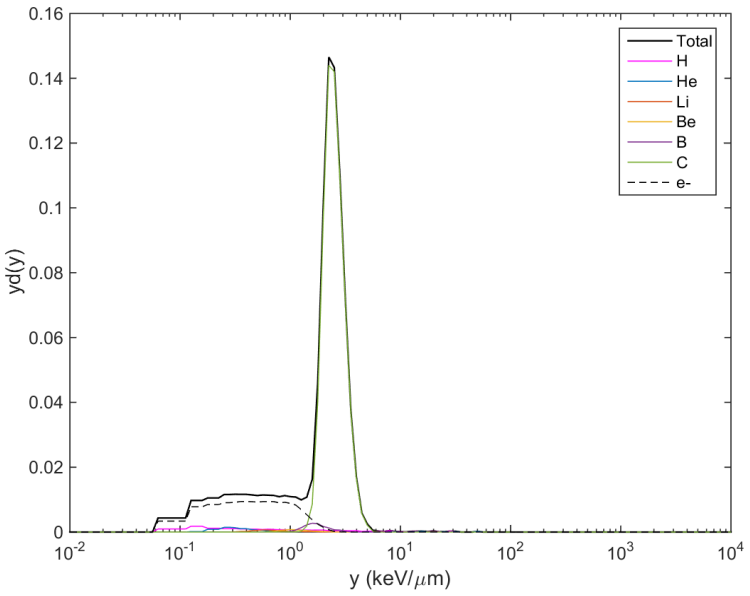

Figure 5.32. Microdosimetric spectrum obtained for the telescope placed in-field at 50 mm in the phantom. Spectra is dominated by primary carbon ions contribution.

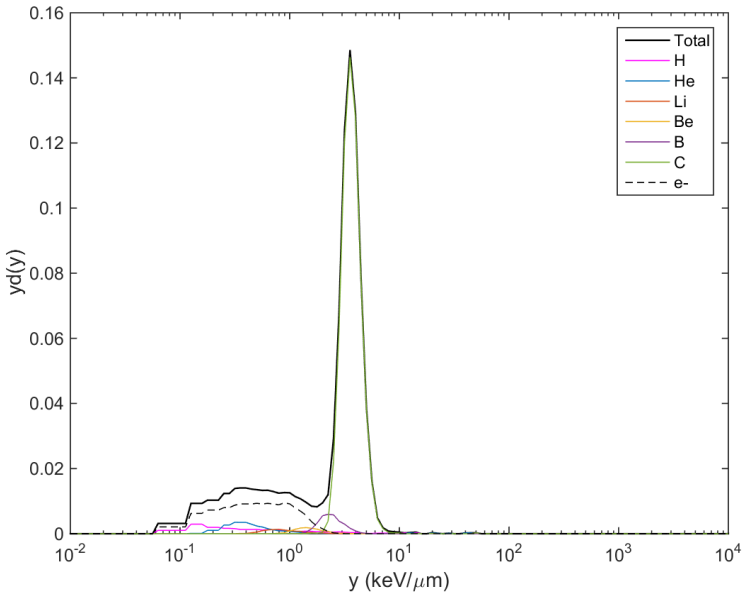

Figure 5.33. Microdosimetric spectrum obtained for the telescope placed in-field at 150 mm in the phantom. The spectrum is dominated by primary carbon ions contribution at higher lineal energy with respect to previous position.

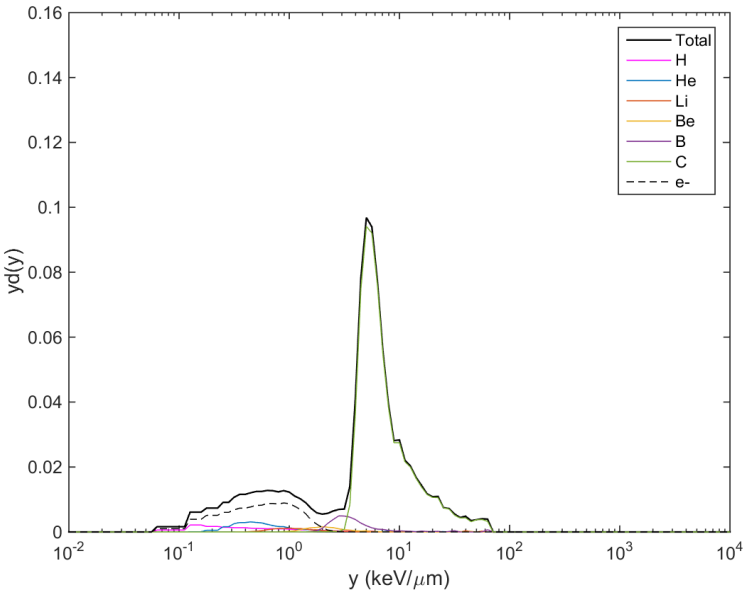

Figure 5.34. Microdosimetric spectrum obtained for the telescope placed in-field at 190 mm in the phantom. The spectrum is dominated by primary carbon ions contribution at higher lineal energy with respect to previous position.

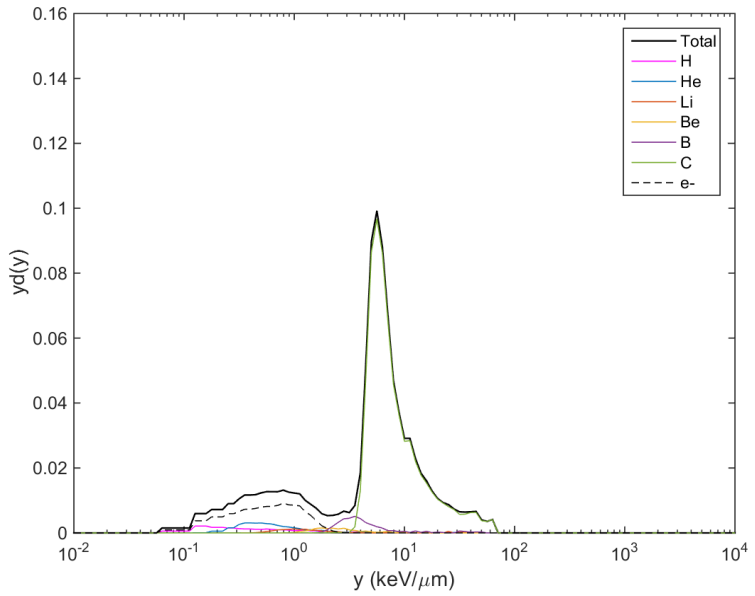

Figure 5.35. Microdosimetric spectrum obtained for the telescope placed in-field at 195 mm in the phantom.

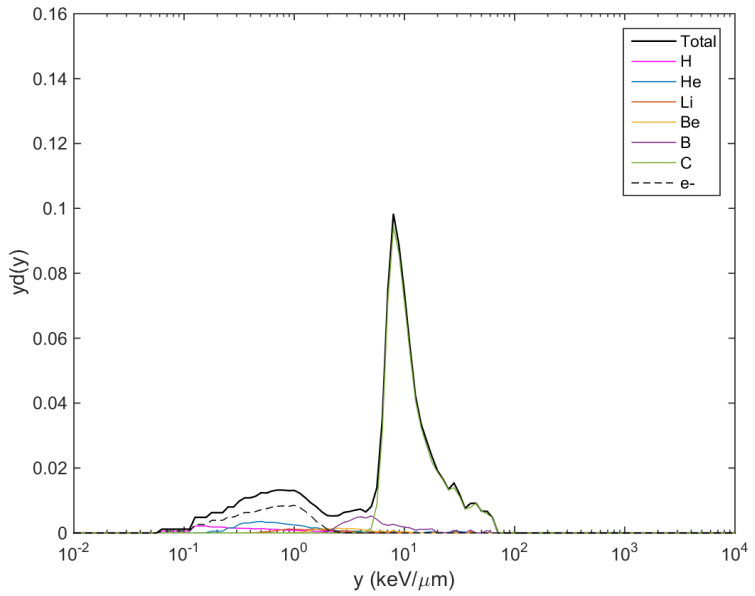

Figure 5.36. Microdosimetric spectrum obtained for the telescope placed in-field at 210 mm in the phantom.

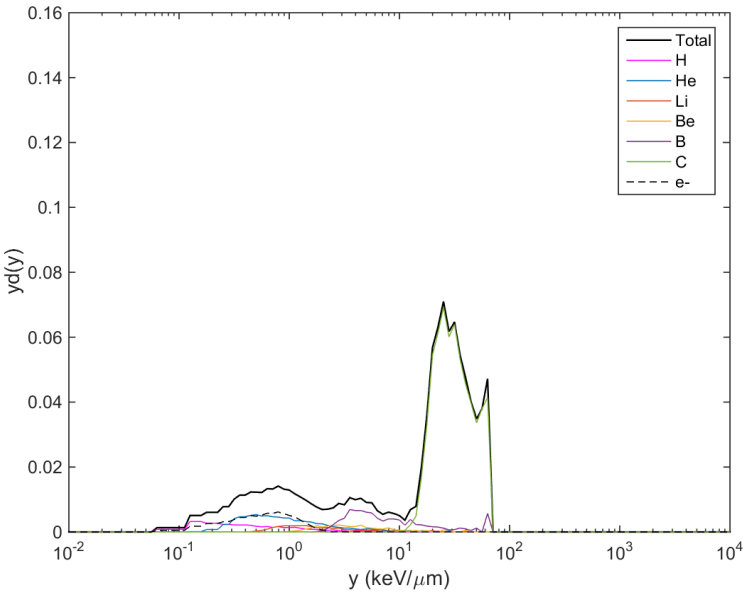

Figure 5.37. Microdosimetric spectrum obtained for the telescope placed in-field at 220 mm in the phantom. Spectra is dominated by primary carbon ions contribution. Carbon edge becomes visible.

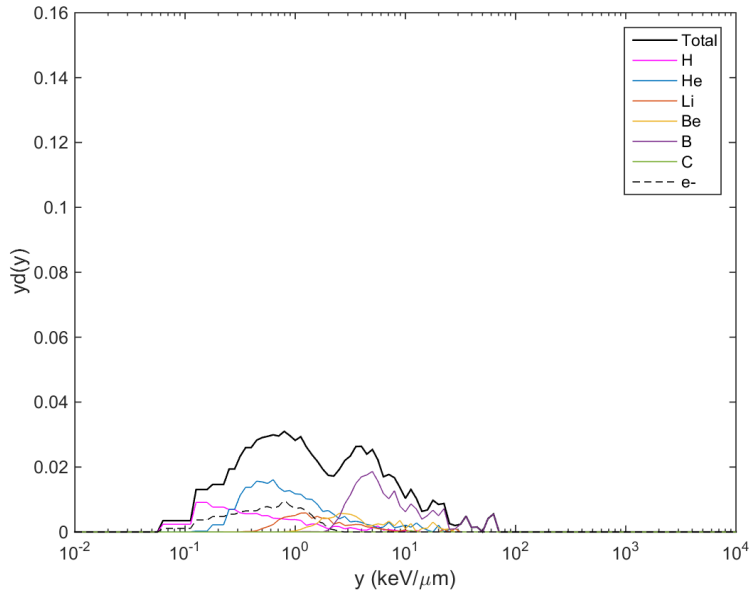

Figure 5.38. Microdosimetric spectrum obtained for the telescope placed in-field at 225 mm in the phantom. Spectra is dominated by secondary fragments.

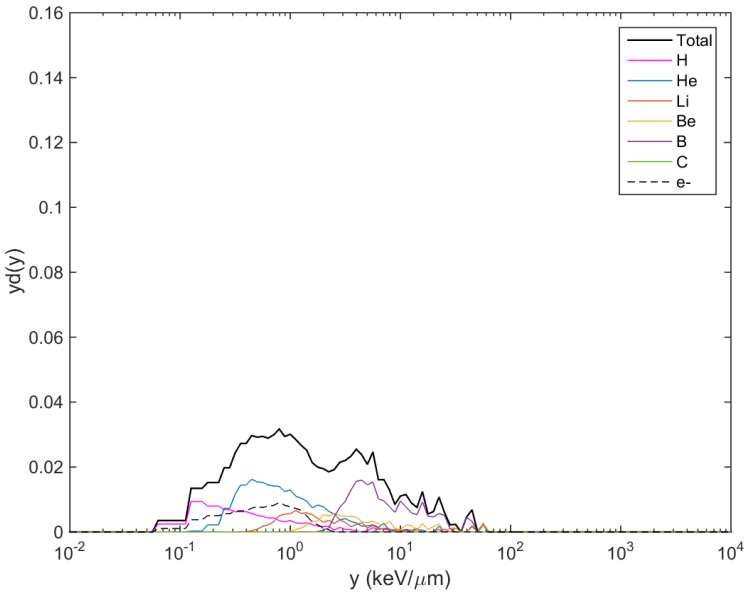

Figure 5.39. Microdosimetric spectrum obtained for the telescope placed in-field at 230 mm in the phantom. Spectra is dominated by secondary fragments.

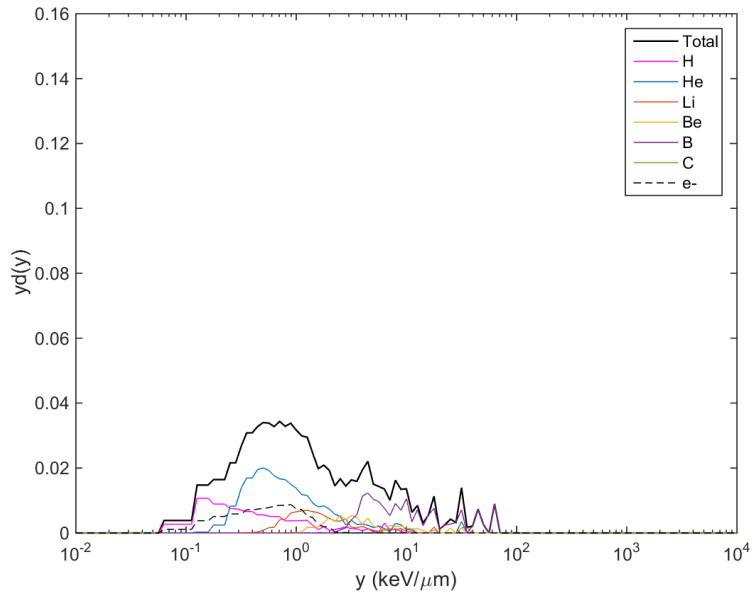

Figure 5.40. Microdosimetric spectrum obtained for the telescope placed in-field at 250 mm in the phantom. Spectra is dominated by secondary fragments.

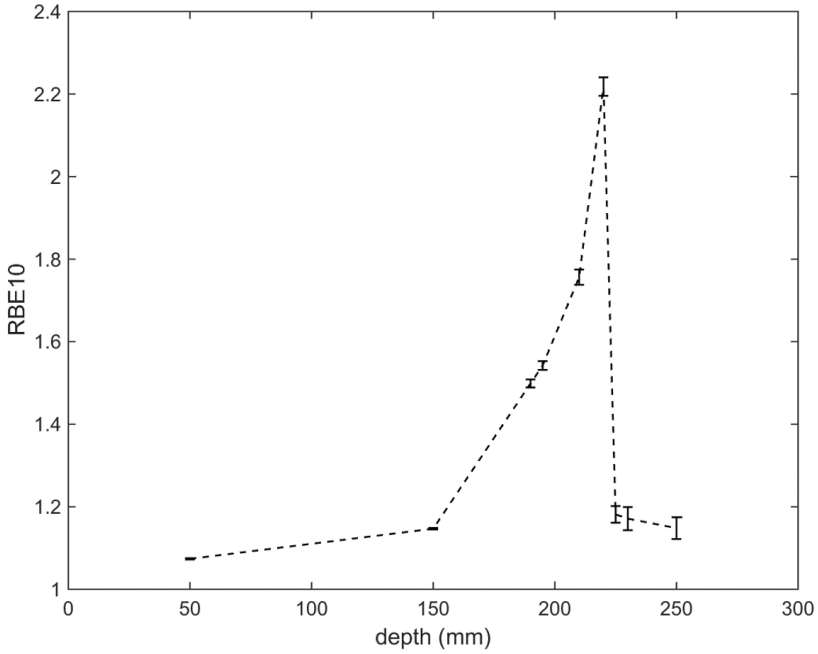

Figure 5.41. RBE_{10} profile obtained from microdosimetric spectra using the MKM model. Depth values refer to the depth in the phantom, an in-field configuration. As expected, the profile is almost flat in the plateau and in the tail of the SOBP, with the higher values recorded in the distal part of the SOBP. Lines are shown to help the eye and only the points where error bars are shown where simulated.

5.4.2. Out of field configuration

The detector response was further characterized by having it placed outside of the incoming primary beam. The detector was placed face-on with respect to the beam at the fixed distance of 35 mm from the axis but at three different depths along the SOBP, for which only the results considered more meaningful are shown. These positions were chosen as to compare the results with corresponding positions in-field where the SOBP is located. For these simulations the number of generated primary particles was 10^8 per position.

Figure 5.42 shows the response of the ΔE-E telescope set at 200 mm depth in the phantom and 35 mm from the axis. At this position only a small

amount of low energy secondary fragments are visible and no primary carbon ions, in contrast to the same depth in field where carbon ions are numerous. This result was expected since lighter ions are characterized by greater scattering when compared to heavier ions and therefore can more easily contribute to dose out of field.

Figure 5.43 shows the microdosimetric spectra obtained in the same position, which, as expected, is dominated by secondary fragments and mainly protons. Separated dose weighted components are shown. The MKM model was then applied to obtain the RBE_{10} profile shown in Figure 5.44. It can be noted that the range of the RBE_{10} values is consistent with those obtained at HIMAC [11].

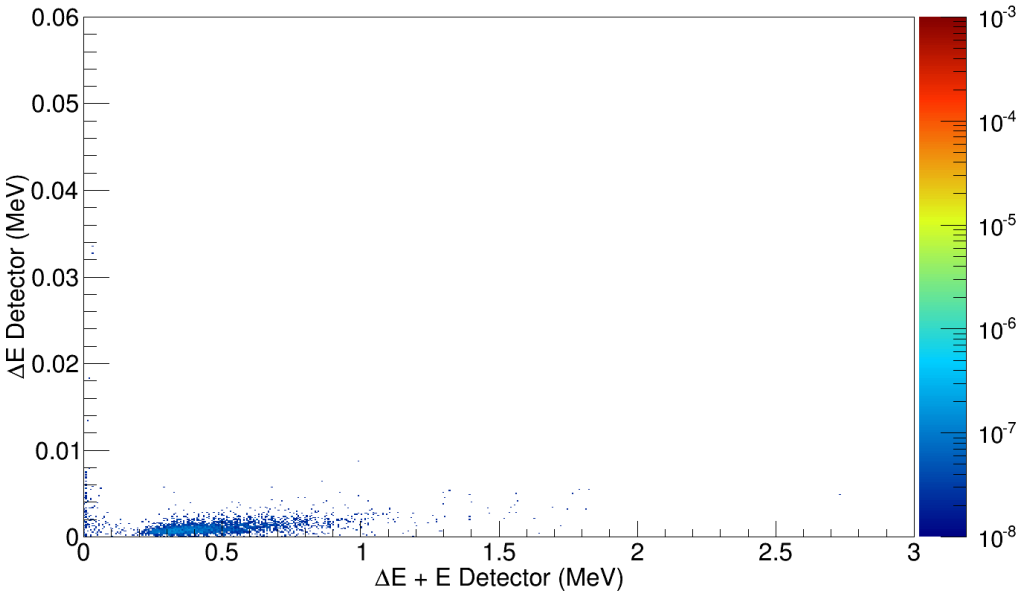

Figure 5.42. ΔE-E plot for telescope placed out of field at 200 mm depth in the phantom and 35 mm from the axis. Only a small amount of low energy secondary fragments are visible.

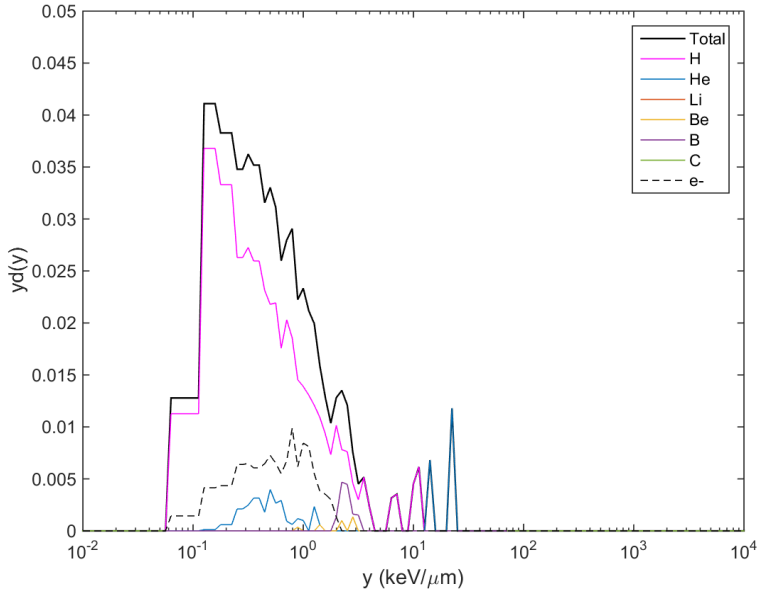

Figure 5.43. Microdosimetric spectrum obtained for the telescope placed out-of-field at 200 mm in the phantom and at 35 mm distance from the axis. The spectrum is dominated by secondary fragments.

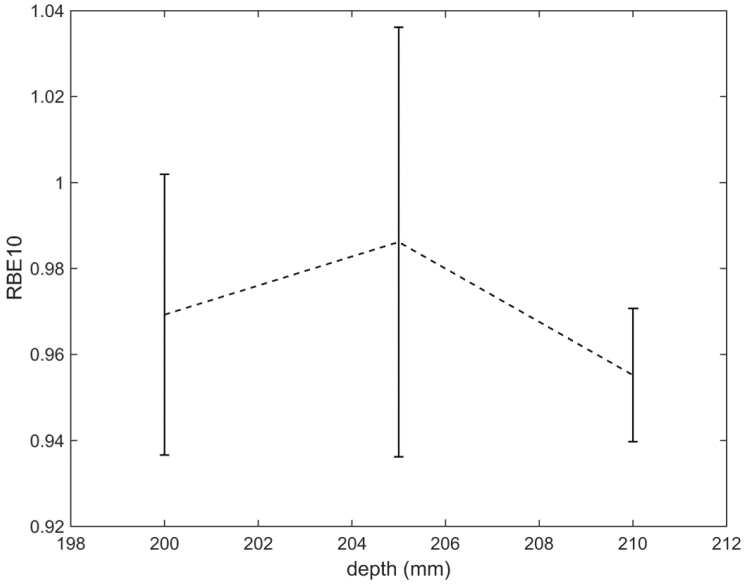

Figure 5.44. RBE_{10} profile obtained from microdosimetric spectra using the MKM model. Depth values refer to the depth in the phantom at a distance of 35 mm from the main axis, an out of field configuration. As expected, the profile is almost flat with values significantly lower than the corresponding values for the same depths in field. Lines are shown to help the eye and only the points where error bars are shown where simulated.

Finally the detector was placed face-on with respect to the primary incoming beam at different distances from the axis but at the fixed depth of 210 mm in the phantom, corresponding to a SOBP position in field. These positions were chosen as to describe the RBE_{10} profile and its fall off at the boundary between an in-field and an out of field configuration. For these simulations, the number of generated primary particles was $2x10^7$.

The obtained microdosimetric spectra are shown in Figure 5.46, Figure 5.47 and Figure 5.48. Separated dose weighted components have been shown in each microdosimetric spectrum. In-field spectra such as that in Figure 5.46 is dominated by the carbon ions contribution whereas out of field spectra such as that in Figure 5.48 is dominated by secondary fragments, mainly protons. It should be noted that the primary beam half-size is 15 mm so the off-set position in Figure 5.46 is technically at the boundary between an in-field position and an out of field one. In fact at this position the lineal energy contribution due to primary carbons is still big and then greatly decreases with the increase of the off-set.

The MKM model was then employed to obtain the RBE_{10} profile shown in Figure 5.49. As expected, values are flat in-field whereas decrease significantly at the boundary of the beam half-size, from 1.8 to approximately 1.2 and are then flat around 1 out of field. This means that the biological efficacy of the carbon ion beam is significantly greater in-field with respect to out of field, with a quite sharp fall off at the boundary between the two. Again, the range of the RBE_{10} values calculated in this work and reported in Figure 5.49 is consistent with those obtained at HIMAC [11].

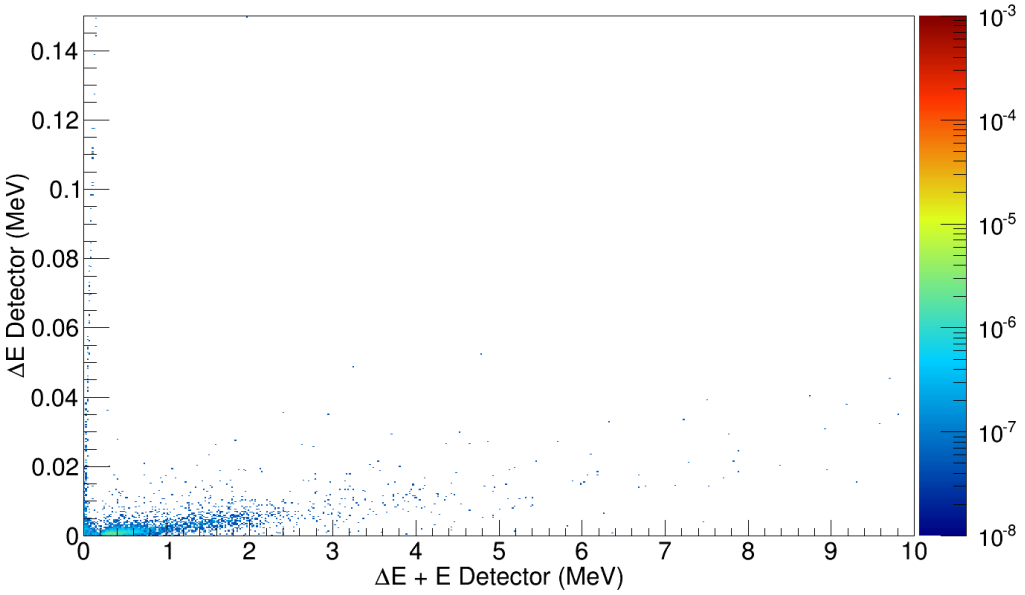

Figure 5.45. ΔE-E plot for telescope placed out of field at 210 mm depth in the phantom and 25 mm from the axis. Only a small amount of low energy secondary fragments are visible.

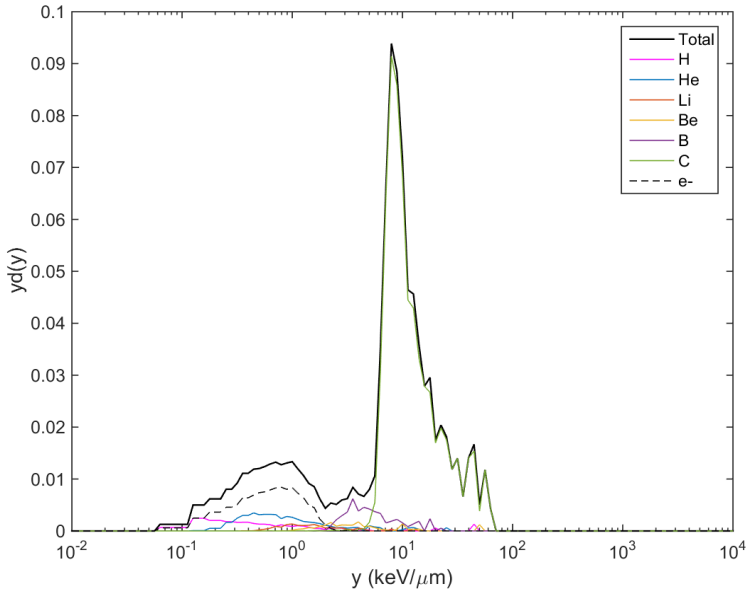

Figure 5.46. Microdosimetric spectrum obtained for the telescope placed out-of-field at 210 mm in the phantom and at 15 mm distance from the axis. The spectrum is dominated by primary carbon ions.

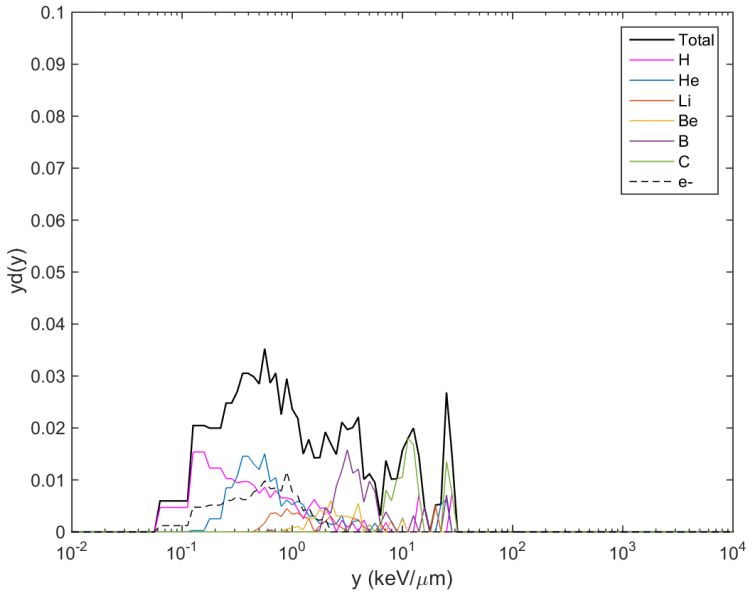

Figure 5.47. Microdosimetric spectrum obtained for the telescope placed out-of-field at 210 mm in the phantom and at 20 mm distance from the axis. The spectrum is dominated by secondary fragments.

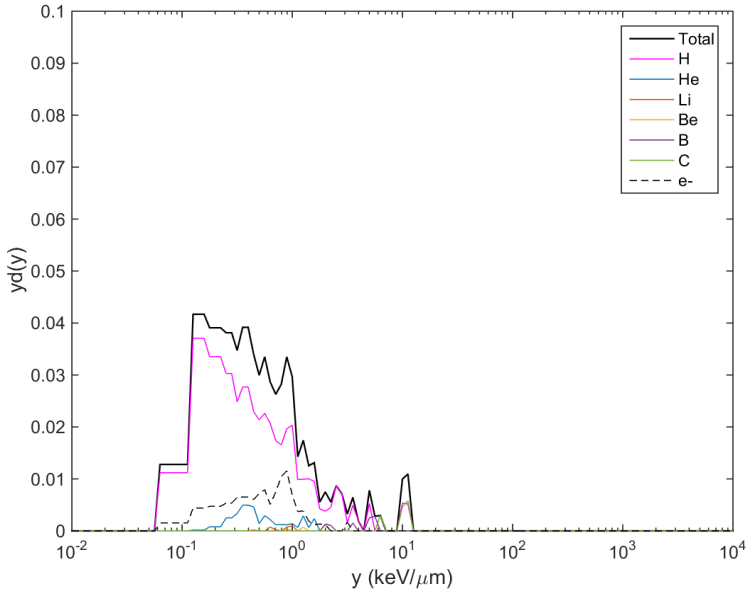

Figure 5.48. Microdosimetric spectrum obtained for the telescope placed out-of-field at 210 mm in the phantom and at 35 mm distance from the axis. The spectrum is dominated by secondary fragments.

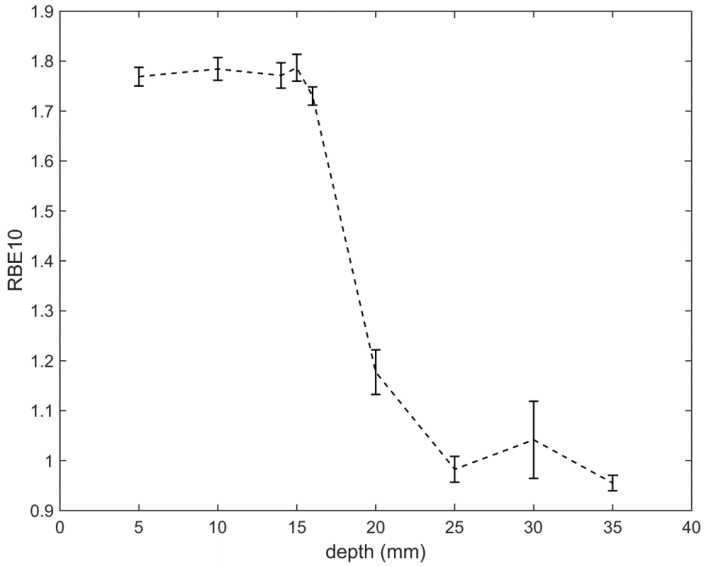

Figure 5.49. RBE_{10} profile obtained from microdosimetric spectra using the MKM model. Depth values refer to the distance from the main axis. Positions from 0 to 15 mm are in-field whereas positions from 15 to 35 mm are out of field. The RBE_{10} is flat in-field and fall sharply towards significantly lower values out of field, where the biological efficacy of the carbon ion beam is thus smaller. Lines are shown to help the eye and only the points where error bars are shown where simulated.

6. ΔE-E telescope characterization with a low energy carbon ion beam at ANU

This experiment was conducted at the Heavy Ion accelerator (14UD) facility at the Australian National University (ANU) and was significant mainly for the reliable information it could provide on the fragments present in a low-energy carbon ion beam field and on the energy deposition in the distal part of the Bragg Peak. As a part of this study, the ΔE-E telescope with the monolithic configuration was irradiated at the same beam line for the purpose of characterizing its expected behavior. At the moment of the writing of this thesis, the experimental measurements were not available making it therefore not possible to compare simulation results against experimental data.

6.1. Experimental set-up

A mono-energetic 5.95 MeV/nucleon carbon ion beam accelerated by the 14UD pelletron shown in Figure 6.1 was extracted and directed toward a vacuum chamber.

Figure 6.1: the 14UD pelletron accelerator at the Heavy Ion facility at the Australian National University (ANU).

A gold scatterer 0.52 μm thick and 12 mm radius was installed in the vacuum chamber, for which see Figure 6.2, on the path of the incoming beam to appropriately lower the beam current through Rutherford scattering and provide the desired beam intensity incident on the detector, which would not otherwise be able to operate in an effective and reliable way.

For the purpose of characterizing the detector behavior along the carbon ion beam Bragg Peak, low density polyethylene foils with different thicknesses were placed, one at a time, on the beam path just before the detector itself.

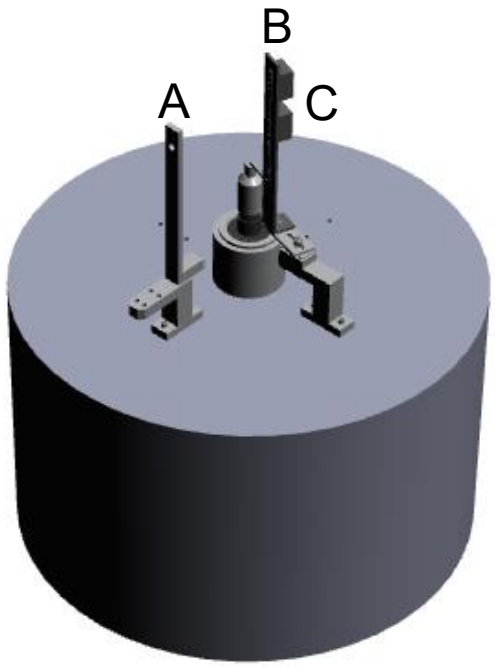

Figure 6.2: a virtual model of the vacuum chamber with the gold scatterer holder on the left [A] and the polyethylene foils holder [B] and detector holder [C] at the centre. The primary beam enters the chamber from the left, passes through the scatterer [A] and hits the foil with the select thickness before hitting the detector.

6.2. The GEANT4 application

A GEANT4 simulation was developed to accurately model the experimental configuration described in section 6.1. In the simulated geometrical set-up, the vacuum chamber with the gold scatterer was modelled. A polyethylene phantom box with 1 cm side was modelled inside the vacuum chamber on the path of the primary carbon ions. For the purpose of characterizing the ΔE-E telescope response, the monolithic detector was modelled and placed at different depths in the polyethylene phantom starting from the surface, as shown in Figure 6.3.

The different depths at which the detector is, one after the other, placed in the phantom reflect the varying thickness of the polyethylene foils placed in front of the telescope in the actual experiment.

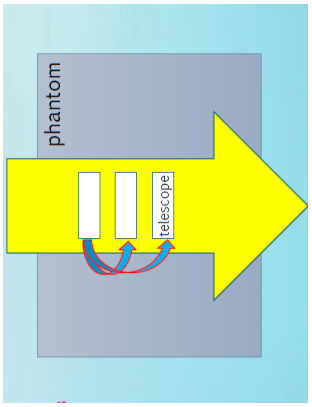

Figure 6.3. Simulated set-up with incoming primary beam (yellow arrow). The polyethylene phantom in figure (grey box) was placed in a simulated vacuum world (light blue box). To simulate the detector response at different depths along the primary carbon ions Bragg curve, the ΔE-E telescope (white box) was placed at different positions starting from the phantom surface. Positions were simulated one at a time in order to not alter the radiation field.

6.3. Characterization of the carbon ion radiation field

The radiation field was simulated using a 5.95 MeV/nucleon mono-chromatic carbon ion beam with 10^7 primary particles generated at 1 m from the polyethylene phantom surface inside the vacuum chamber, with direction normal to the phantom surface itself. In this simulation the physics list was the same as the one adopted in the GEANT4 simulation study of Chapter 5. A 0.001 mm cut was applied to the whole world as well as to the detector region. Figure 6.4 shows the resulting Bragg Peak in the polyethylene phantom. The different positions at which the detector was placed in the phantom for the subsequent study detailed in section 6.4 are also shown.

The distribution of the point of origin of secondary particles generated in the polyethylene phantom is projected in the 2D plots from Figure 6.5 to Figure 6.8 as a top-view of phantom. The spatial resolution is 1 mm^2 and the scale is normalized to the number of incident primary carbon ions. The region with the greater production of secondary particles is in the proximity of the primary beam path up to the Bragg Peak with almost no production beyond that point.

The 2D energy deposition distributions of some of the secondary particles is plotted in Figure 6.9 and Figure 6.10. The 2D energy deposition distribution of primary carbon ions is shown in Figure 6.11 whereas the 2D total energy deposition is shown in Figure 6.12. Plots are with a precision of 1 mm^2 and the scale is normalized to the number of incident particles.

Total energy deposition is almost uniform up to the primary carbon ions Bragg Peak with a limited energy deposition beyond that point mainly due to helium.

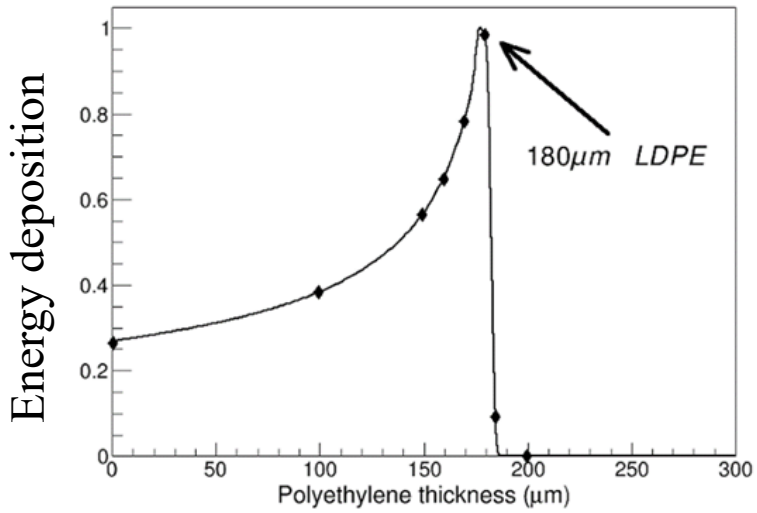

Figure 6.4. Bragg Peak of a 5.95 MeV/nucleon carbon ion beam incident on a polyethylene phantom. The black dots represent the different depths at which the detector was placed for the subsequent study detailed in section 6.4

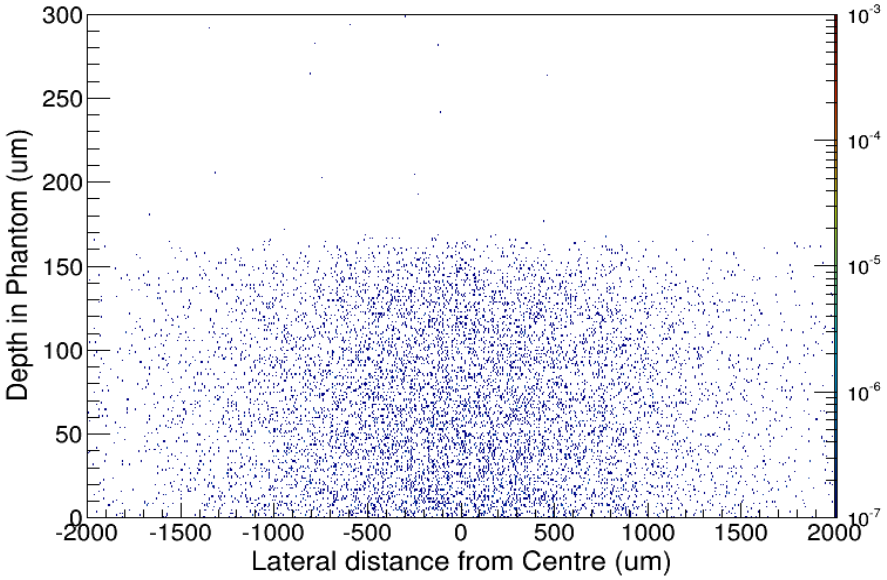

Figure 6.5. 2D distribution of the point of origin of secondary ^{1}H normalized to the number of incident primary carbon ions.

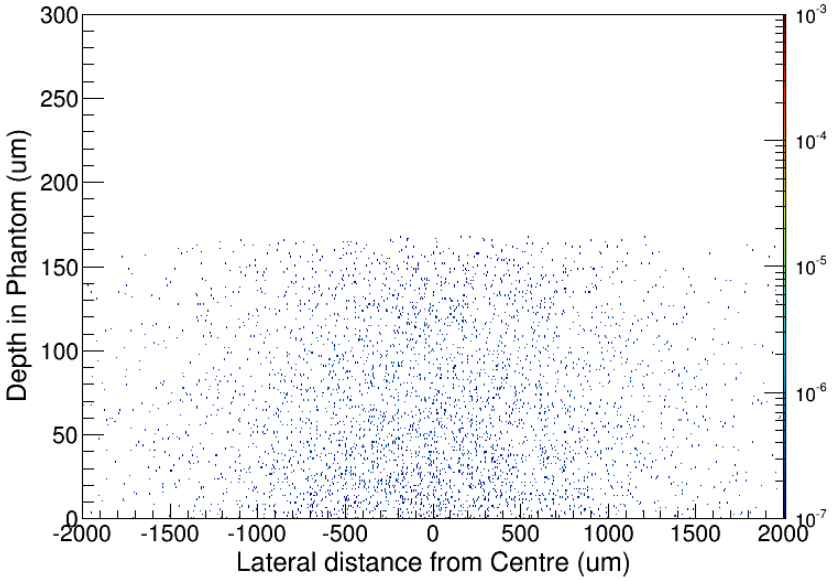

Figure 6.6. 2D distribution of the point of origin of secondary ^{4}He normalized to the number of incident primary carbon ions.

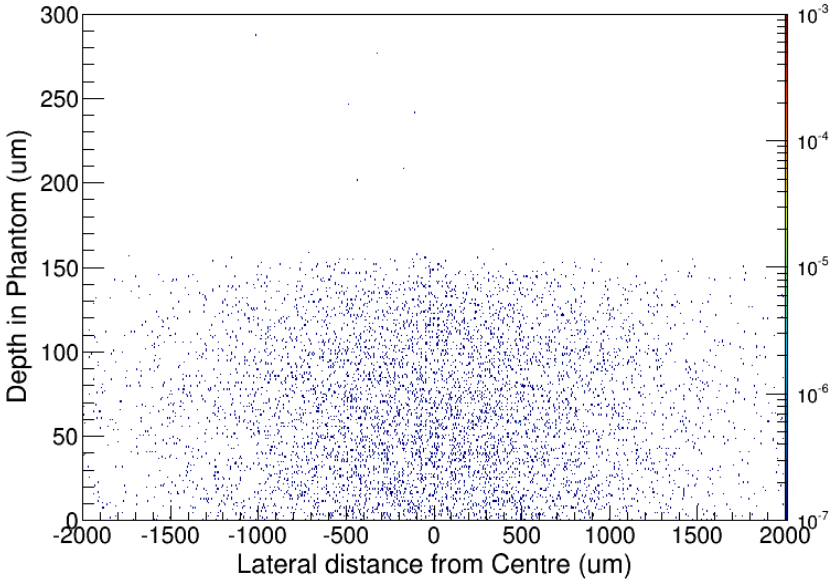

Figure 6.7. 2D distribution of the point of origin of secondary ^{12}C normalized to the number of incident primary carbon ions.

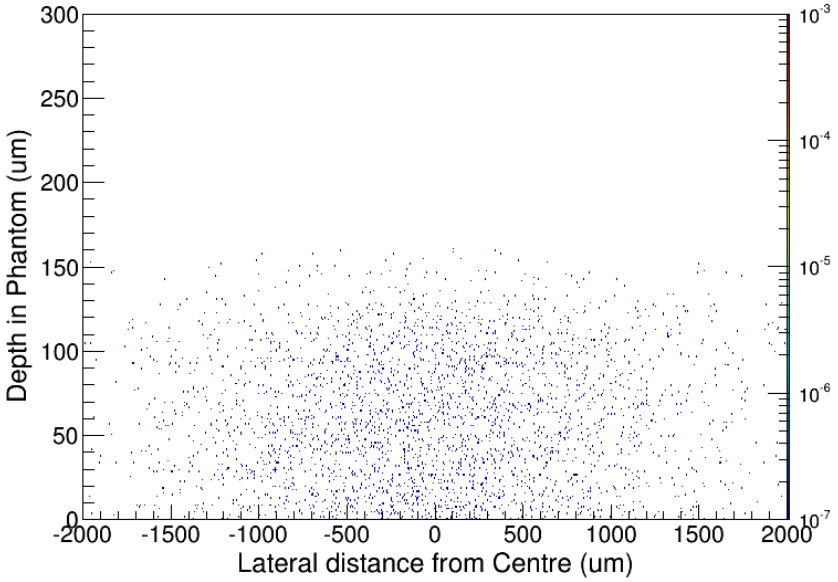

Figure 6.8. 2D distribution of the point of origin of secondary neutrons normalized to the number of incident primary carbon ions.

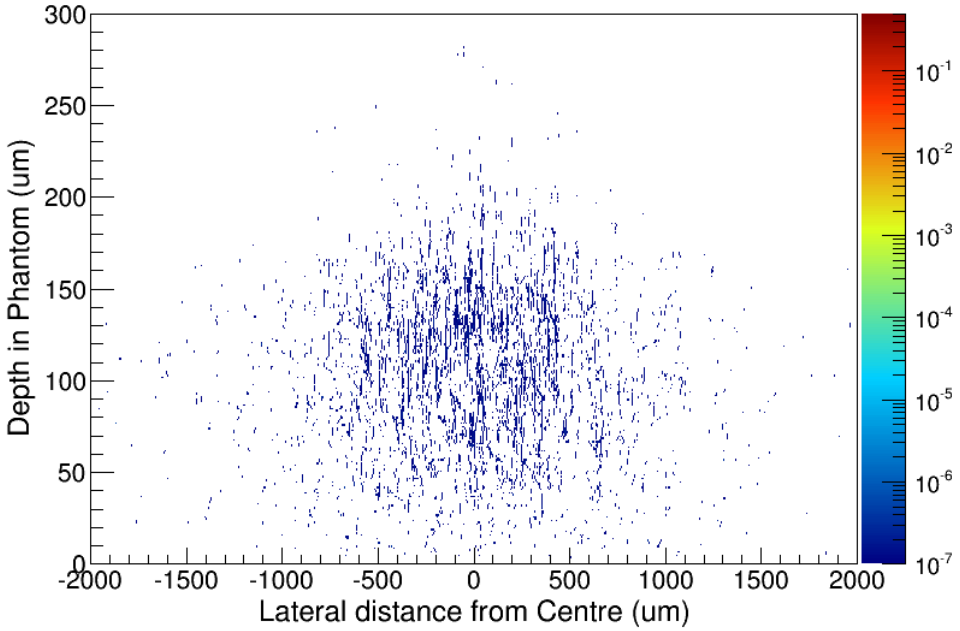

Figure 6.9. 2D energy deposition in the target due to He.

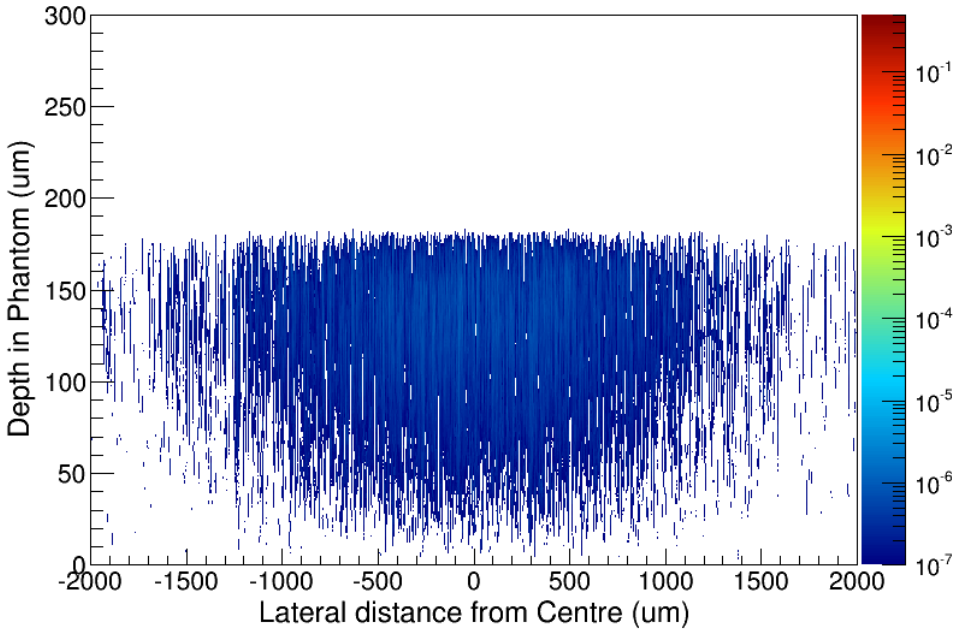

Figure 6.10. 2D energy deposition in the target due to secondary carbon ions.

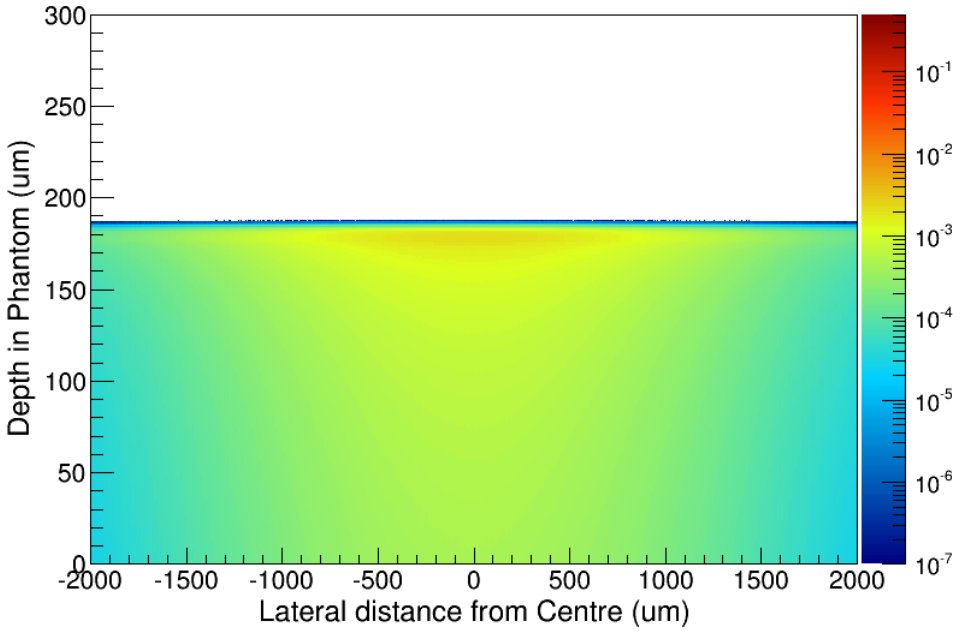

Figure 6.11. 2D energy deposition in the target due to primary carbon ions.

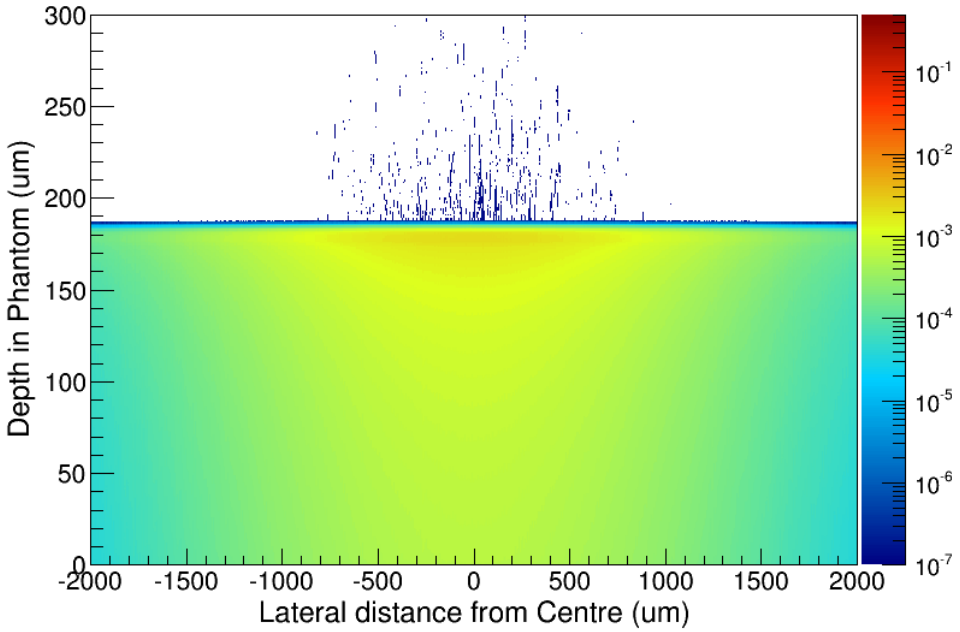

Figure 6.12. 2D total energy deposition in the target.

6.4. Characterization of the ΔE-E telescope response

A silicon ΔE-E telescope detector with a monolithic configuration[11] as described in Chapter 2 was modelled. Its dimensions were set to 25 mm^2 of superficial area with a 1.9 μm thick ΔE silicon stage and a 500 μm thick E stage. A 0.24 μm thick layer of oxygen oxidize was added on top of the ΔE stage.

The response of the detector is shown in 2D plots with the energy deposited in the ΔE stage on the vertical axis and the energy deposited in both the ΔE and E stages in the horizontal axis.

11 In contrast to the ΔE-E telescope detector used for the CNAO beam line which was with a pixelated ΔE stage configuration instead.

As already detailed in Chapter 5, also for this study the detector was simulated as operated in coincidence, hence only particles depositing their energy in both the ΔE and the E stages were counted, as for the real device.

The detector was placed in the center of the incoming beam at various depths in the phantom, listed in Table 6.1. The different depths were chosen to reflect the different thicknesses of the polyethylene foils placed before the detector in the actual experiment. 10^7 events were generated in each simulation to obtain statistically meaningful results.

Depth in phantom (μm)	Region
0	Plateau
50	Plateau
92	Plateau
143	Plateau
155	Plateau
165	Plateau
171	Plateau
183	Bragg Peak
185	Tail
200	Tail

Table 6.1. The detector was placed at various depths in the polyethylene phantom, starting from the phantom surface closest to the incoming primary beam. Positions are distributed along the Bragg curve in order to cover plateau, Bragg Peak proper and tail regions.

In Figure 6.13 and then in all figures to Figure 6.16 it is shown the response of the ΔE-E telescope detector when placed at the depths in Table 6.1. In all plots, the frequency of the events is normalized with respect to the number of the simulated events.

Figure 6.13 shows that there is a clustered maximum energy deposition in the detector at approximately 70 MeV due to primary carbon ions. The amount of hydrogen and helium nuclei is significant and occurs for lower energy depositions. These fragments are originated mainly in the scatterer. In Figure 6.14 and Figure 6.15 the primary particles are depositing less energy in the detector whereas the contribution of protons and helium isotopes remains unchanged. As expected, in Figure 6.16, a position just beyond the Bragg Peak, there are no more carbon ions depositing energy in the detector. Protons and helium isotopes are still the most abundant contributors to the energy deposition demonstrating the almost non-existence of heavier fragments throughout the Bragg curve due to a low-energy carbon ions beam. In the distal part of the Bragg Peak the energy deposition is, as expected, almost exclusively due to light fragments.

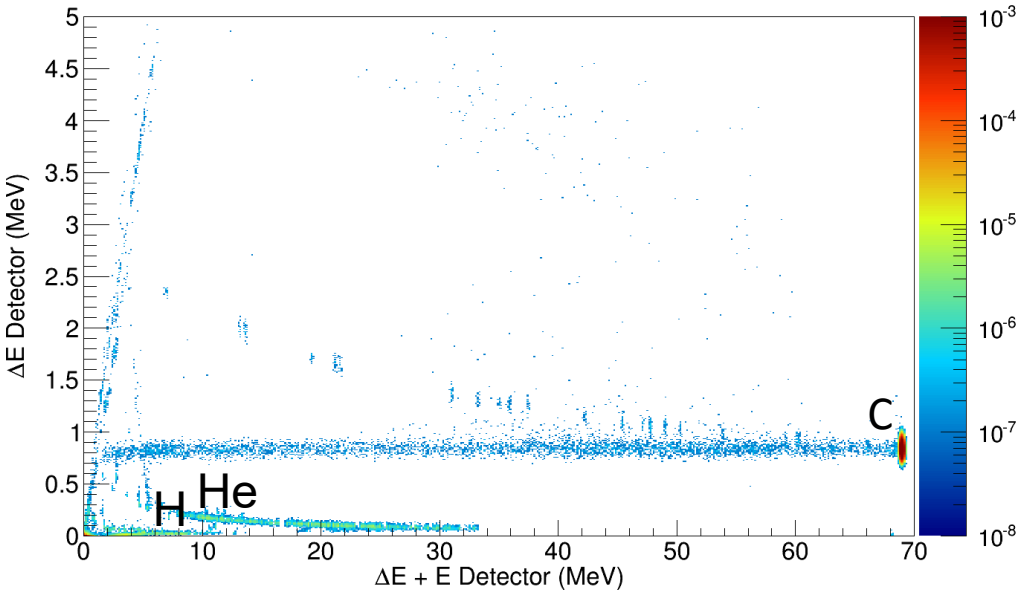

Figure 6.13. ΔE-E plot for telescope placed in-field at 0 µm depth from the phantom surface closest to the incoming primary beam.

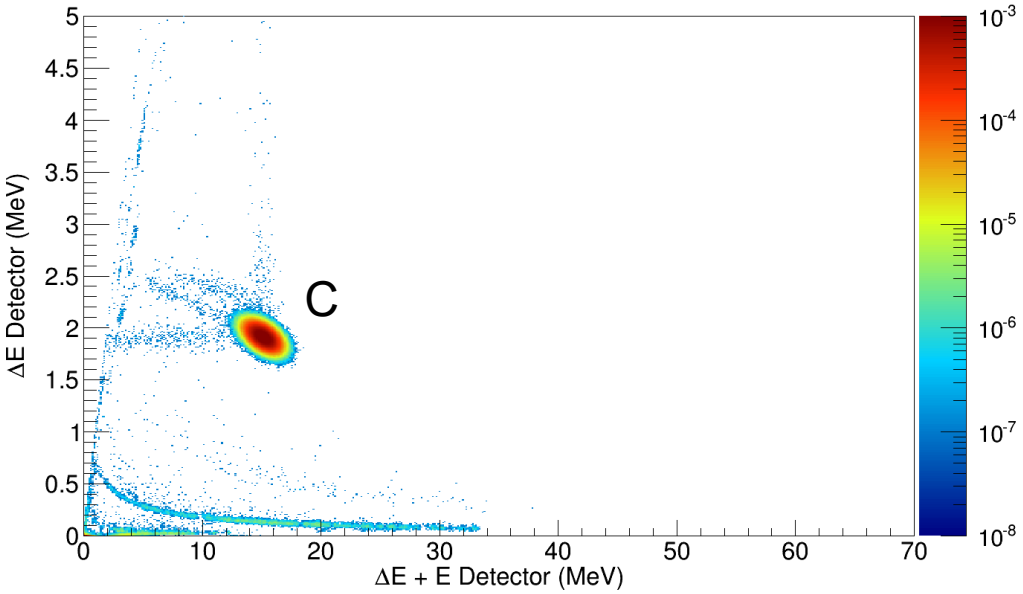

Figure 6.14. ΔE-E plot for telescope placed in-field at 157 µm depth from the phantom surface closest to the incoming primary beam.

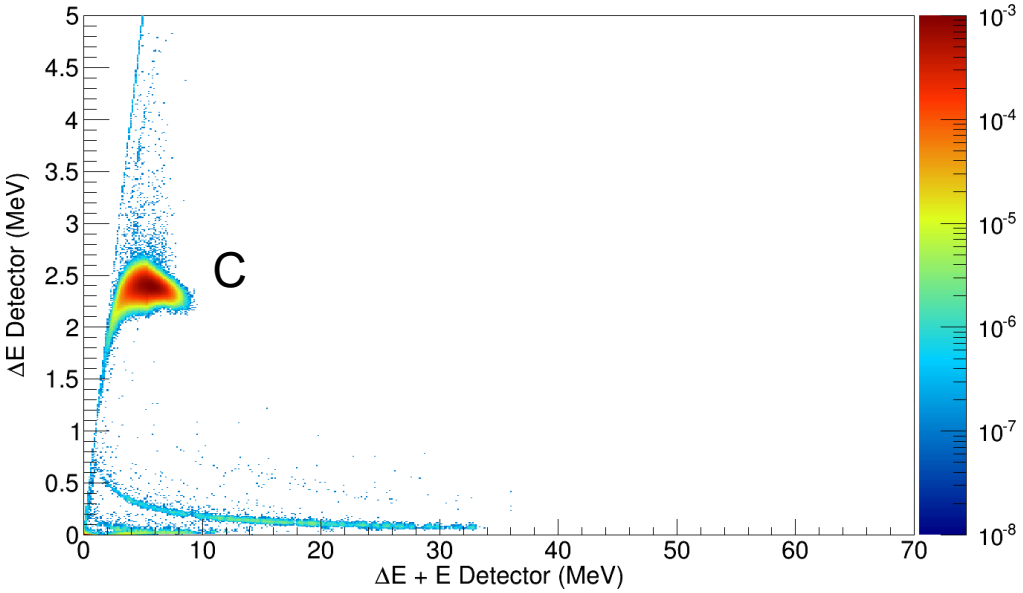

Figure 6.15. ΔE-E plot for telescope placed in-field at 171 µm depth from the phantom surface closest to the incoming primary beam.

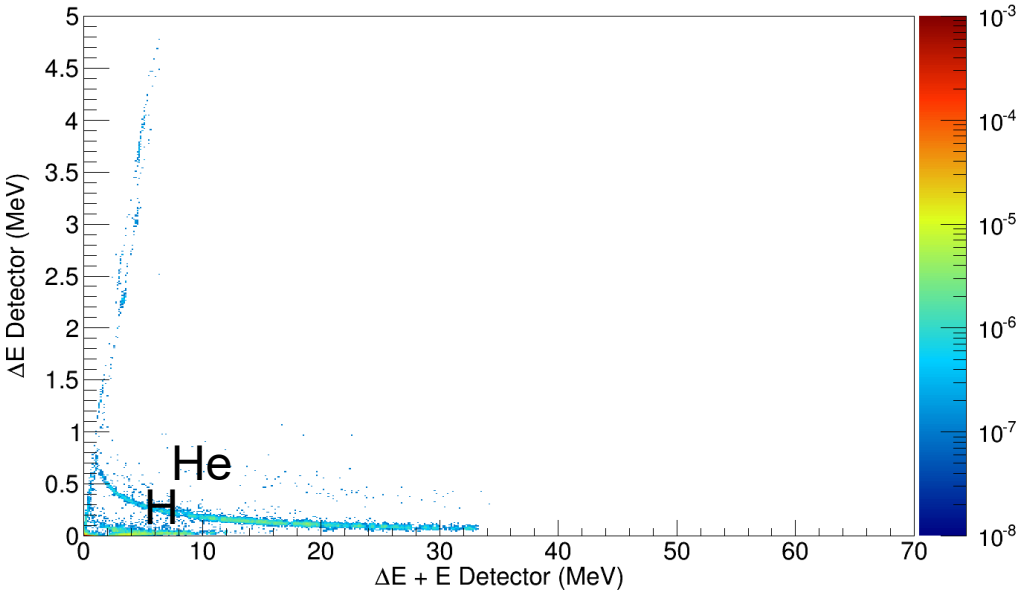

Figure 6.16. ΔE-E plot for telescope placed in-field at 183 μm depth from the phantom surface closest to the incoming primary beam.

Microdosimetric spectra were calculated for the same positions listed in Table 6.1, a selection of which is shown in Figure 6.17 and then in all figures to Figure 6.21 and separated dose weighted components microdosimetric spectra were studied but only the total spectra are shown.

For the spectra acquired in the plateau region, the main contributions to the lineal energy derive from the primary carbons, for which see the spike in Figure 6.17. On the other hand, in the proximity of the Bragg Peak, in Figure 6.18 the spectrum is dominated by secondary electrons originated outside the detector whereas moving closer to the Bragg Peak the spectrum starts to be dominated by the helium contribution, as in Figure 6.19. At the Bragg Peak, for which see Figure 6.20, the spectrum is dominated by the helium contribution. Beyond the Bragg Peak, for which see Figure 6.21, hydrogen but mainly helium isotopes play the most significant role, with no carbon contribution whatsoever.

The microdosimetric spectra have then been converted from silicon to tissue using an appropriate factor [24] and the MKM model as described in

Chapter 1 has been used to determine the RBE_{10} profile shown in shown Figure 6.22.

In Figure 6.22 it should be noted that the counter-intuitive downward trend of the RBE_{10} values towards the Bragg Peak is due to the overkilling effect. According to the theory, when the ionization density in the cell is much higher than that needed to kill the cell itself, there is a decreasing in the biological efficacy of the ionizing radiation. The reversed increasing trend near the Bragg Peak is explained by an intrinsic limitation of microdosimetry. In this region primary carbon ions detected in the telescope are actually stoppers and therefore do not cross the silicon ΔE layer as required by theory to apply a microdosimetry approach.

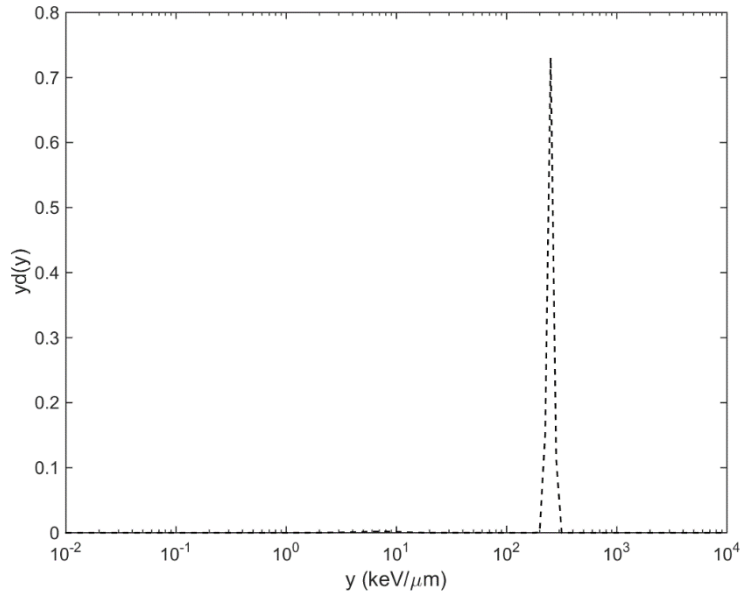

Figure 6.17. Microdosimetric spectrum obtained for the telescope placed in-field at 0 μm depth from phantom surface closest to the incoming primary beam.

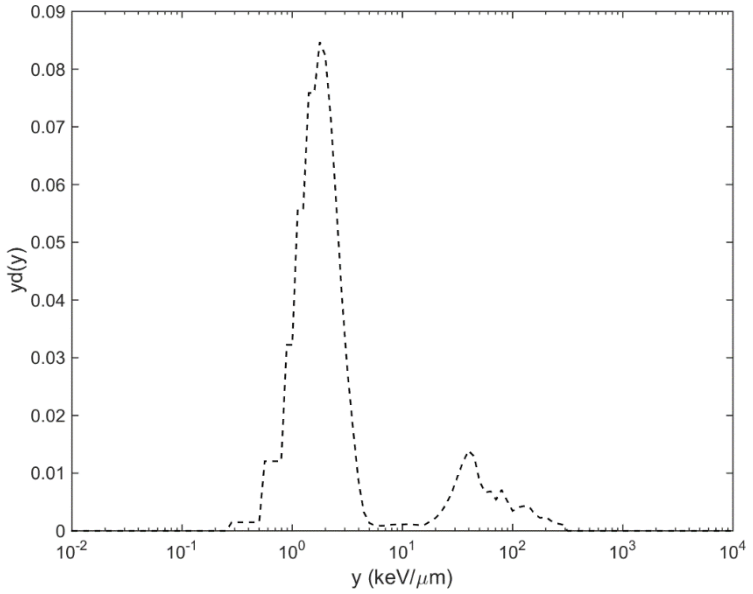

Figure 6.18. Microdosimetric spectrum obtained for the telescope placed in-field at 157 µm depth from phantom surface closest to the incoming primary beam.

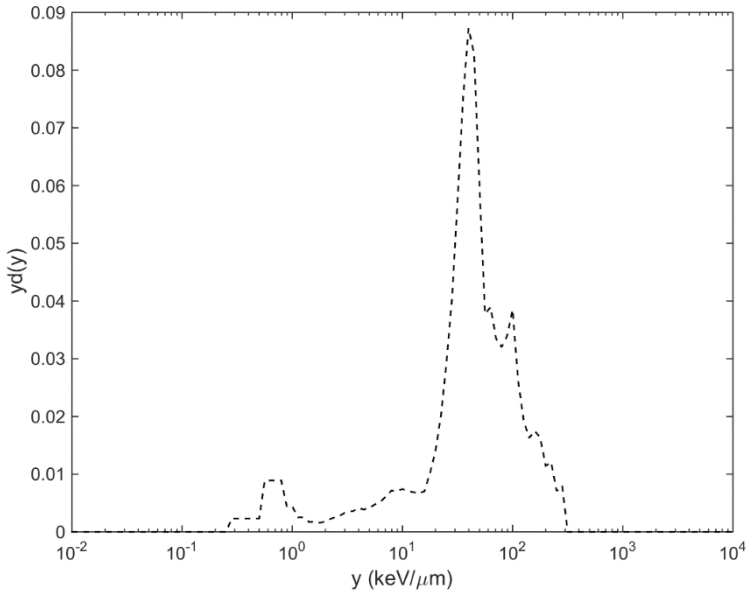

Figure 6.19. Microdosimetric spectrum obtained for the telescope placed in-field at 171 µm depth from phantom surface closest to the incoming primary beam.

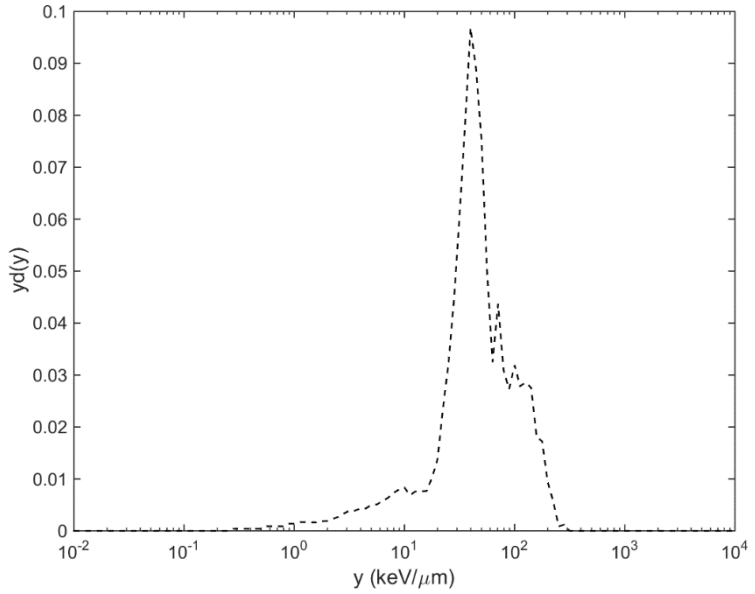

Figure 6.20. Microdosimetric spectrum obtained for the telescope placed in-field at 183 μm depth from phantom surface closest to the incoming primary beam.

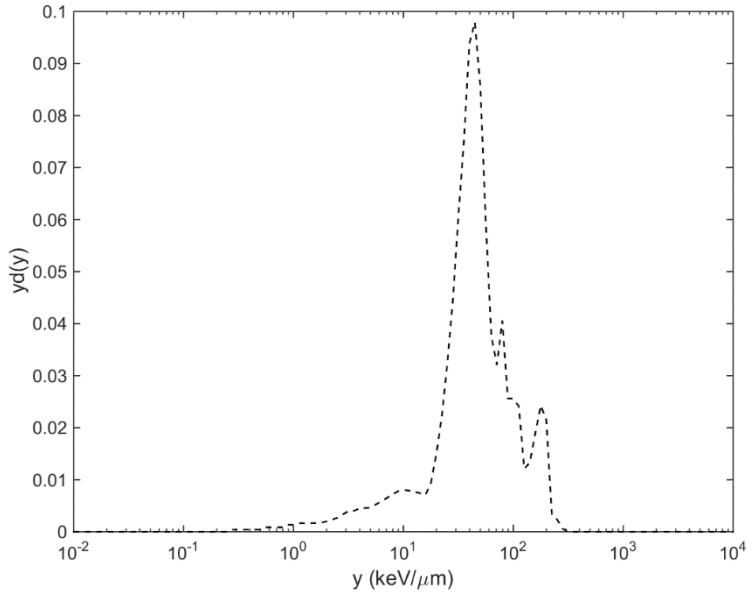

Figure 6.21. Microdosimetric spectrum obtained for the telescope placed in-field at 200 μm depth from phantom surface closest to the incoming primary beam.

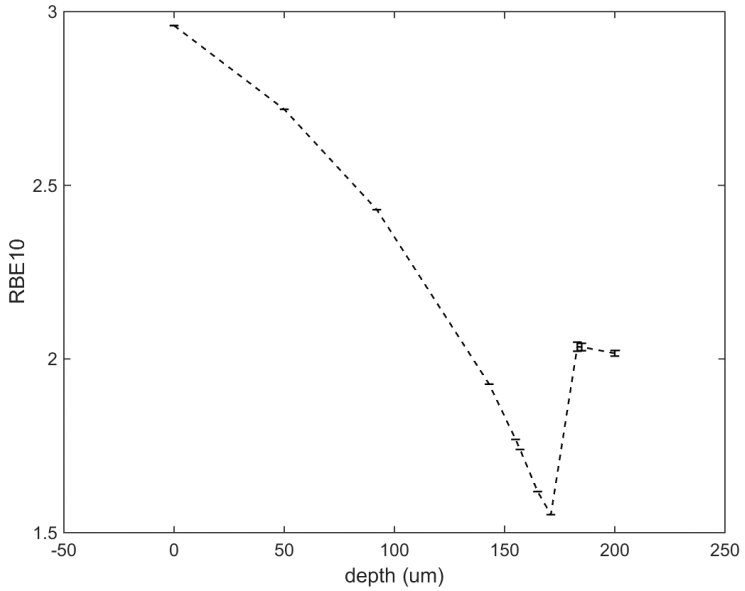

Figure 6.22. RBE_{10} profile obtained from microdosimetric spectra using the MKM model. Depth values refer to depths from phantom surface closest to the incoming primary beam, an in-field configuration. Counter-intuitively, the profile does not show a rising trend towards the Bragg Peak followed by a sharp fall-off. On the contrary, the RBE_{10} values decrease towards the Bragg Peak due to the overkilling effect. The sharp increase at the Bragg Peak is instead due to an intrinsic limitation of the microdosimetric model: carbon ions at these depths are coming to a complete stop in the ΔE layer of the detector whereas they should be crossing it for the microdosimetry theory to be coherently applied. Lines are shown to help the eye and only the points where error bars are shown where simulated.

7. Conclusions

In this thesis work the GEANT4 toolkit has been partially validated for Heavy Ion Therapy (HIT) applications by reproducing the Bragg Peak in water for carbon ion beams with clinical energies. Different physics models have been tested and compared and the *Electromagnetic standard package option 3* to model the electromagnetic physics and *QMD* to model ion hadron physics have been adopted based on the results of this thesis and on scientific literature. In the future a more comprehensive validation for the GEANT4 toolkit for HIT applications will be performed and fragments yield and energy/angular spectra will be simulated and discussed against experimental data for carbon ion beams with clinical energies.

Furthermore, in this thesis work the ΔE-E silicon telescope detector has been characterized as a possible Quality Assurance (QA) solution for HIT thanks to its theoretical capability to distinguish different fragments in a complex radiation field such as that due to carbon ions with clinical energies. Moreover, it has been shown that the ΔE stage of the telescope detector can in principle be used as a microdosimeter to obtain microdosimetric spectra with a sub-millimeter spatial resolution, proving to be a better alternative to TEPCs. The RBE_{10} profile has been estimated using the Microdosimetric Kinetic Model (MKM).

In the future, this work could be used to better understand the experimental measurements performed at the CNAO beam line with the ΔE-E silicon telescope, which would in turn be used to quantify the accuracy of the GEANT4 application hereby developed and discussed.

8. Bibliography

[1] K. Noda et al, «Recent progress of HIMAC for sophisticated heavy-ion cancer radiotherapy,» *Nuclear Instruments and Methods in Physics Research B,* 2014.

[2] WHO, «Fact sheet N° 310 - The top 10 causes of death,» 2014.

[3] B. Steward e C. Wild, World Cancer Report 2014, WHO Press, 2014.

[4] K. Noda et al, «New Heavy-Ion Cancer Treatment Facility at HIMAC,» *Proceedings of EPAC08,* pp. 1818 - 1820, 2008.

[5] V. Brower, «Carbon ion therapy to debut in Europe,» *Journal of the National Cacner Institute,* 2009.

[6] *Radiological Sciences,* vol. 50, n. 7, 2007.

[7] D. C. Schlaff et al, «Bringing the heavy: carbon ion therapy in the radiobiological and clinical context,» *Radiation Oncology,* 2014.

[8] U. Amaldi et al, «Radiotherapy with beams of carbon ions,» *Reports on progress in physics,* 2005.

[9] D. Schardt et al, «Heavy-ion tumor therapy: Physical and radiobiological benefits,» *Review of Modern Physics,* vol. 82, pp. 383-425, 2010.

[10] M. Krämer e M. Scholz, «Treatment planning for heavy ion therapy,» *Phys. Med. Biol.,* 2000.

[11] M. Tamura et al, «Microdosimetric calculation of penumbra for biological dose in wobbled carbon-ion beams with Monte Carlo Method,» *Radiol Phys Technol,* 2013.

[12] D. Schardt et al, «Nuclear fragmentation of high-energy heavy-ion beams in water,» *Advances in Space Research,* vol. 17, n. 2, pp. 87-94, 1996.

[13] I. Pshenichnov et al, «Neutrons from fragmentation of light nuclei in tissue-like media: a study with the GEANT4 toolkit,» *Phys. Med. Biol.,* n. 50, 2005.

[14] L. Sihver et al, «Depth-dose distributions of high-energy carbon, oxygen and neon beams in water,» *Jpn. J. Med. Phys.,* vol. 18, pp. 1-21, 1998.

[15] N. Matsufuji et al, «Influence of fragment reaction of relativistic heavy charger particles on heavy-ion readiotherapy,» *Phys. Med. Biol.,* vol. 48, n. 11, 2003.

[16] A. Ferrari et al, «Secondary particle yields from 400 MeV/u carbon ion and 250 MeV proton beams incident on thick targets,» *Nuclear Instruments and Methods in Physics Research Section B,* vol. 269, n. 13, p. 1474–1481, 2011.

[17] K. Gunzert-Marx, H. Iwase, D. Schardt e S. R. Simon, «Secondary beam fragments produced by 200MeV/u carbon ions in water and their dose contributions in carbon ion therapy,» *New Journal of Physics,* vol. 12, 2008.

[18] ICRU, «ICRU Report 36,» 1983.

[19] IAEA, «Relative Biological Effectiveness in Ion Beam Therapy,» IAEA, 2008.

[20] J. T. Bushberg, The Essential Physics of Medical Imaging, Lippincott Williams and Wilkins, 2002.

[21] F. M. Khan, The Physics of Radiation Therapy, Philadelphia: Lippincott Williams and Wilkins, 2003.

[22] H. H. Rossi e M. Zaider, Microdosimetry and its applications, Springer, 1996.

[23] P. D. Bradley, «The Development of a Novel Silicon Microdosimeter for High LET Radiation Therapy [PhD Thesis work. Unpublished],» 2000.

[24] P. D. Bradley et al, «Tissue equivalence correction for silicon microdosimetry detectors in boron neutron capture therapy,» *Medical Physics,* vol. 25, 1998.

[25] S. Chiriotti et al, «Equivalence of Pure Propane and Propane-TE Gases for Microdosimetric Measurements».

[26] D. Moro e e. al, «BNCT dosimetry performed with a mini twin tissue-equivalent proportional counters (TEPC),» *App. Rad. and Isot. ,* vol. 67, pp. S171-S174, 2009.

[27] A. Kellerer, «Event simultaneity in cavities. Theory of the distortions of energy deposition in proportional counters,» *Radiat. Res.,* vol. 48, p. 216, 1971.

[28] L. Lindborg e A. Brahme, «Influence of microdosimetric quantities on observed dose-response,» *Radiat. Res.,* vol. 124, pp. 23-28, 1990.

[29] P. Metcalfe, T. Kron e P. Hoban, The Physic of Radiotherapy x-rays and electrons, Medical Physics Publishing, 2007.

[30] S. Agosteo et al, «Feasibility study of radiation quality assessment with a monolothic silicon telescope: irradiations with 62 MeV/nucleon carbon ions at LNS-INFN,» *Radiation Measurements,* 2011.

[31] G. Knoll, Radiation Detection and Measurement, John Wiely and Sons, 2010.

[32] D. Bolst, Characterisation of a Silicon ΔE-E detector placed in a carbon ion beam using GEANT4 (Thesis work, unpublished), 2013.

[33] S. Agosteo et al, «Analytical model for a monolithic silicon telescope - Response function of the E stage,» *Radiation Measurements,* 2008.

[34] S. Agosteo et al, «A pixelated silicon telescope for solid state microdosimetry,» *Radiation Measurements,* 2008.

[35] A. Kordyasza et al, «Monolithic silicon delta-electron telescope produced by the quasi-selective epitaxy,» *Nuclear Instruments and Methods in Physics Research A,* 2004.

[36] A. Topkar et al, «Development of integrated ΔE-E silicon detector telescope using silicon planar technology,» *Nuclear Instruments and Methods in Physics Research A,* 2011.

[37] T. Linh et al, «High spatial resolution microdosimetry with ΔE-E detector on carbon ion beam: Monte Carlo simulations,» *Phys. Med. Bio. Journal* [submitted].

[38] S. Agosteo et al, «A feasibility study of a solid-state microdosimeter,» *Applied Radiation and Isotopes,* 2005.

[39] S. Agosteo et al, «Study of a silicon telescope for solid state microdosimetry: preliminary measurements at the therapeutic proton beam line of CATANA,» *Radiation Measurements,* 2010.

[40] M. V. Introini, Silicon Detectors for Hadrontherapy Applications, tesi di dottorato in Scienza e Tecnologia delle radiazioni, Politecnico di Milano, 2008.

[41] S. Agosteo et al, «A solid state microdosimeter based on a monolithic silicon telescope,» *Radiation protection dosimetry,* 2006.

[42] N. Matsufuji et al, «Specification of Carbon Ion Dose at the National Institute of Radiological Sciences,» *J. Radiat. Res.,* n. 48, pp. A81-A86, 2007.

[43] O. Jakel et al, «Heavy Ion Therapy: Status and Perspectives,» *Technology in Cancer Research & Treatment,* vol. 2, n. 5, 2003.

[44] J. Gueulette e A. Wambersie, «Comparisons of the methods of specifying carbon ion doses at NIRS and GSI,» *J. Radiat. ,* 2007.

[45] H. Tsujii et al, «Clinical results of carbon ion radiotherapy at NIRS,» *J. Radiat.,* 2007.

[46] Y. Kase et al, «Microdosimetric measurements and estimation of human cell survival for heavy-ion beams,» *Radiat. Res.,* 2006.

[47] H. Paganetti, Prtono therapy physics, 2012.

[48] A. Lechner et al, «Validation of recent GEANT4 physics models for application in carbon ion therapy,» *Nucelar Instruments and Methods in Physics Research B,* n. 268, 2010.

[49] Dudouet, «Benchmarking GEANT4 nuclear models for hadron therapy with 95 MeV/nucleon carbon ions,» *Physical Review C,* 2014.

[50] I. Pshenichnov et al, «Nuclear fragmentation reactions in extended media studied with GEANT4 toolkit,» *Nuclear Instruments and Methods in Physics Research B,* n. 268, 2010.

[51] De Napoli et al, «Nuclear reaction measurementes on tissue-equivalent materials and GEANT4 Monte Carlo simulations for hadrontherapy,» *Phys. Med. Biol.,* 2014.

[52] Braunn et al, «Comparisons of hadrontherapy-relevant data to nuclear interaction codes in the Geant4 toolkit,» *Journal of Physics: Conference Series,* 2013.

[53] T. T. Böhlen et al, «Benchmarking nuclear models of FLUKA and GEANT4 for carbon ion therapy,» *Phys. Med. Biol.,* n. 55, 2010.

[54] Mairani et al, «Clinical implementation of full Monte Carlo dose calculation in proton beam therapy,» in *Nucl Sci. Symp. Conf. Record*, 2008.

[55] Paganetti et al, «Clinical implementation of full Monte Carlo dose calculation in proton beam therapy,» *Phys. Med. Biol.,* 2008.

[56] Schardt et al, «Nuclear fragmentation of high-energy heavy-ion beams in water,» *Advances in Space Research,* vol. 17, n. 2, pp. 87-94, 1996.

[57] «ROOT - Data Analysis Framework,» [Online]. Available: https://root.cern.ch/drupal/. [Retrieved 02 June 2015].

[58] GEANT4 Physics Reference Manual (Version 9.6.0), 2012.

[59] The Geant4 Collaboration, Geant4 User's Manual for Application Developers-Version, 2012.

[60] N. Matsufuji et a, *Phys. Med. Biol.,* vol. 50, 2005.

[61] E. Haettner et al, «Experimental study of nuclear fragmentation of 200 and 400 MeV/nucleon carbon ions in water for applications in particle therapy,» *Phys. Med. Biol.,* 2013.

[62] D. Cussol, «Nuclear Physics and Hadrontherapy,» Université de Caen Basse-Normandie.

[63] G. Danielsen, *Simulating carbon beam fragmentation in water phantom with GEANT4 (Bachelor's thesis),* 2009.

[64] «Physics Lists EM constructors in Geant4,» [Online]. Available: http://geant4.web.cern.ch/geant4/collaboration/working_groups/electromagnetic/physlist9.4.shtml. [Retrieved 17 April 2015].

[65] T. Koi, «Joint International Conference on Supercomputing in Nuclear Applications and Monte Carlo 2010,» 2010.

[66] K. Niita et al, *Phys. Rev. C,* 1995.

[67] A. Boudard et al, «Intranuclear cascade model for a comprehensive description of spallation reaction data,» *Phys. Rev. ,* 2002.

[68] G. E. S. W. Group, 2009.

[69] NIST, «NIST database,» [Online]. Available: http://www.nist.gov/srd/. [Retrieved 24 April 2015].